Topology Optimization for Thermal and Flow Fields Related to Lattice Boltzmann Method

NGUYEN Truong

Topology Optimization for Thermal and Flow Fields Related to Lattice Boltzmann Method

by

NGUYEN Truong

Submitted in Partial Fulfillment of the Requirements
for the Degree of Doctor of Philosophy
in Mechanical Engineering

Graduate School of Engineering
Nagoya University

March 2021

Acknowledgments

This thesis is submitted to fulfill the requirements to obtain the degree of doctor philosophy at the department of mechanical systems engineering, graduated school of engineering, Nagoya university. This study was conducted at Matsumoto's laboratory, Nagoya university under the supervising of professor Toshiro Matsumoto.

It would have been impossible to complete this thesis without his generous help and thoughtful guidance of my advisor, professor Toshiro Matsumoto. I would like to express my special gratitude to him who always makes things are impossible to be possible. I am truly thankful for what he has done for me since the day I first met him in Taiwan until I complete this thesis.

I would like to extend my appreciation to professor Toru Takahashi and professor Hiroshi Isakari for their dedicated and continuous supports during my long study and research in the laboratory. Their unlimited knowledge and friendly made my study was so much comfortable.

I would like to express my sincere thanks to professor Masato Yoshino for his great knowledge on the field of the lattice Boltzmann method and this was my honor to cooperate with him in the study. Especially, I would like to sincerely thank professor Kentaro Yaji for his helpful lectures and his wide open-minded during my 3-days visiting his laboratory at Osaka university. He and his students made me feel at home during my short visiting their home-liked research center.

I would like to sincerely appreciate professor Tsuyoshi Inoue and professor Takayuki Yamada for their thoughtful examinations of my dissertation. This work would have not been comprehensive without their detailed comments and profound suggestions on the editing of the thesis.

I would also send my sincere gratitude to my friends, a special soulmate, my lovely lab mates and every individual I have met during my study at Nagoya university. Every

single one of you plays a role in my success. You are my true treasures.

Here, I would especially appreciate Dr. Masayuki Shimizu who helped me most during my financial crisis in the last year in my doctoral program at Nagoya university. Without his help, my career path would has been so much more difficult to achieve.

Last but not least, I specially offer my sincere gratitude to my family, my mother, my sisters, and my little Mi-family in Japan whom always silently and unconditionally support me with their true loves.

This is to my late father and brother!

Nagoya, March 25, 2021

Nguyen Truong

Contents

Nomenclature

$*$	The nondimensional quantity
$\bar{\rho}$	Prescribed fluid density
$\bar{J}^*$	Total objective functional
$\bar{p}$	Prescribed fluid pressure
$\bar{Q}$	Prescribed normal heat flux
$\bar{T}$	Prescribed temperature
$\bar{u}$	Prescribed fluid velocity
$\boldsymbol{c}$	Particle velocity
$\boldsymbol{E}$	Total energy
$\boldsymbol{n}$	Normal vector
$\boldsymbol{u}$	Fluid velocity
$\boldsymbol{x}$	Spacial position
χ_ϕ	Characteristic function
Δt	Discrete time step
Δx	Lattice space
$\dot{Q}$	Heat conduction rate
$\hat{T}$	Target temperature
λ	Lagrange's multiplier

$\mathbb{R}$	Real numbers
$\mathcal{W}$	Adjoint temperature
μ	Fluid dynamic viscosity
ν	Macroscopic viscosity
Ω	Computational domain
$\partial\Omega$	Interfaces/structural boundaries
ϕ	Level-set function
ρ	Fluid density
ALBM	Adjoint lattice Boltzmann method
BEM	Boundary element method
BGK	Bhatnagar-Gross-Krook
BVP	Boundary value problem
D2V9	Two-dimensional nine-velocity
FDM	Finite difference method
FEM	Finite element method
FVM	Finite volume method
KKT	Karush-Kuhn-Tucker
LBM	Lattice Boltzmann method
LHS	Left hand side
P1	Publication one
P2	Publication two
PDE	Partial differential equation
Re	Reynolds number

RHS	Right hand side
Sh	Strouhal number
N – S	Navier-Stokes
OBJ – 1	Object-1
OBJ – 2	Object-2
τ	Regularization parameter
$D\backslash\Omega$	Void domain
D	Fixed design domain
f	Velocity distribution function
G	Material volume constraint
g	Adjoint velocity distribution function
h	Heat transfer coefficient
J	Objective functional
K	Proportional constant
k	Thermal diffusivity coefficient
L	Characteristic length
m	The measured quantity
p	Fluid pressure
R	Ideal gas constant
S	Heat source
T	Temperature
t	Fictitious time in the time-evolution equation
U	Characteristic speed of flow

V	Fluid volume constraint
$\bar{J}'$	Design sensitivity
Γ_{in}	Inflow boundary
Γ_{out}	Outflow boundary
Γ_{ε}	Infinitesimal circular boundary
Γ_{D}	Dirichlet boundary
Γ_{h}	Robin boundary
Γ_{N}	Neumann boundary
Γ_{w}	Bounce-back boundary
$\mathcal{T}_{D}$	Topological derivative
Ω_{ε}	Infinitesimal circular domain
τ_{B}	Relaxation time
c_{s}	Speed of sound
FD_{J}	Finite differences of the objective functional
f^{eq}	Maxwell-equilibrium velocity distribution function
$G_{\max}$	Permissible material volume
h^{eq}	Maxwell-equilibrium thermal distribution function
Q	Normal heat flux
T_{∞}	Ambient temperature
$V_{\max}$	Permissible fluid volume
w_{i}	Weighting function

List of Figures

List of Tables

Chapter 1

Introduction

1.1 Motivation

In the conventional methods such as finite element method (FEM), finite volume method (FVM), finite difference method (FDM), or boundary element method (BEM), the iterative change in the optimized shape demands lots of computational resources for re-meshing and re-computation process during optimization. It is often a challenge in the optimization problem for large-scale complex boundary design [1, 2]. Therefore, it demands a substitute simulation method for those conventional methods in fluid flow and structural problems that are satisfied with the following conditions: (i) it is a method that contains a simplicity in implementation and high capability of parallel computation, (ii) it suits for the problem of large-scale with a complex boundary design, (iii) it can manipulate in various engineering design interests, and (iiii) it can be applied and contribute to the on-going development in topology optimization methodologies.

Alternatively, the lattice Boltzmann method (LBM) has been validated as a replaceable method to those conventional methods in solving the fluid flow and heat problems in fluid mechanics [3, 4, 5, 6, 7, 8, 9, 10, 11, 12, 13, 14, 15, 16, 17, 18]. In the LBM, instead of discretization the partial differential equation (PDE) in the Navier-Stokes (N-S) flow or the heat problem, the LBM uses the discretized scheme of the discrete Boltzmann equation to govern the behaviors of those governing equations. Thus the state filed can be managed by the explicit time-evolution equation [19]. The expensive resources to compute the matrices in the PDEs via the conventional methods can be avoided by the free of use of the matrix solver in the LBM.

Furthermore, the LBM is a good applicant for solving the thermal and flow fields in a topology optimization problem considering its simplicity in programming and the high capability to be parallelized in computation [20, 21]. Thus, the LBM is well applicable to the topology optimization problem with large-scale and complex boundaries. One of the important aspects to consider the LBM over the conventional methods in the topology optimization for thermal and flow fields is the similar algorithm in solving the adjoint system as compared to the primal system wherein the methodology possesses the simplicities in implementing and the capability of parallel computation [22, 23, 24]. Therefore, the LBM is an essential candidate to cooperate with the topology optimization in this thesis.

Nevertheless, in fluid flow topology optimization problem, its application in the fluidic design has achieved a majority successful results wherein the steady-state flow is considered, e.g., the fluidic switch design [25, 26, 27], the fluidic diode design [28, 29], and the others [30, 31]. However, its application in the fluidic design wherein the unsteady flow is considered will also be interested, e.g., the fluid pump design, the valve control design, or the vibration control design. In those designs, the use of cost function regarding the dissipated kinetic energy in a maximization problem is essential needed [28, 29]. Thus, the novel contribution of this study is considered in the mentioned problems for not only a single direction flow problem but also the multiple direction flow problems. It is noted that this part reorganizes the author's publication one (P1) [32] associated with this thesis for more comprehensive study. Fig. 1.1 shows the design concept of the time-dependent kinetic energy dissipation device where the symmetric and asymmetric boundary conditions are both considered. To be more specific, the vibration energy of the object-1 (OBJ-1) and object-2 (OBJ-2) is dissipated by using the concept design object I where the input/output conditions do not necessarily need to be symmetric with one another (left-end and right-end vertical boundaries). However, the design object II aims to absorb the vibration energy generated from the same-design OBJ-1 and OBJ-2. Thus, the input/output conditions to the design object II require the symmetric designs to periodically dissipate the kinetic energy of the two objects.

Besides, in topology optimization for the thermal problem, its applications in heat dissipation structure design are widely attractive, e.g., in structural design for heat sink [33] or heat pipe [34, 35]. As shown in the current review paper by Dbouk et al. [36] about the literature of topology optimization for thermal conduction, despite the advantages of LBM

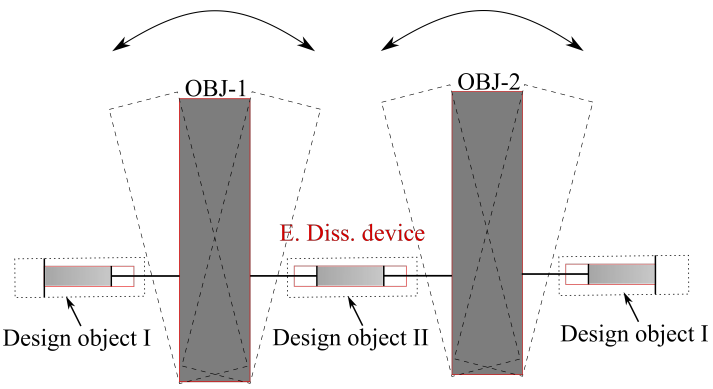

Figure 1.1: The design concept of kinetic energy dissipation device.

in topology optimization, the massive publications have done by using the conventional methods [37, 38, 39, 40, 41, 42, 43, 44, 45, 46, 47, 48, 49, 50, 51, 52, 53, 54]. The use of LBM has not been directly tested for its applicabilities and its high parallel efficiencies. It is, moreover, in a level-set based topology optimization problem, the potential cooperation of the topological derivative concept and the LBM has not been examined yet. Thus, the applicabilities of this collaboration in topology optimization for heat conduction problem is considered in this study as a novel contribution. It is noted that this part reorganizes the author's publication two (P2) [55] associated with this thesis for a more comprehensive study. Fig. 1.2 shows the design concept of the heat dissipation device where the dissipated heat structure generated with the help of topology optimization is an effective method.

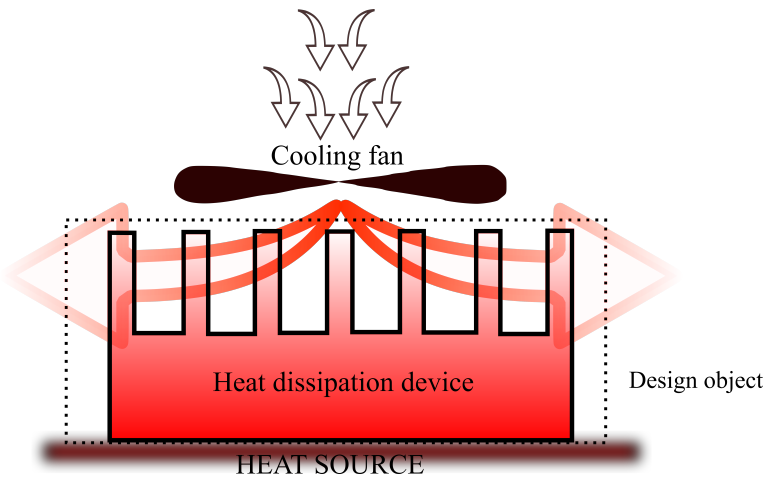

Figure 1.2: The design concept of heat dissipation device.

1.2 Goal

1) To develop a topology optimization for fluid flow that capable to handle various demands in engineering design using lattice Boltzmann method, for example, that is (i) applicability for topology optimization for various objective functions used in fluid mechanics, (ii) applicability for topology optimization for both the minimization and maximization problems, (iii) applicability for topology optimization for single-directional flow and multiple-directional flow, and (iiii) applicability for topology optimization for the transient problem and the steady problem.

2) To develop a more rigorous topology optimization that collaborating with the LBM and topological derivative concept and originally applied to the heat diffusion problem. The novel contribution of the development can become a potential paradigm for other studies of the evolution of the topology optimization for fluid flow, heat transfer, or other structural problems. Its computational efficiency is comparative over the conventional method.

1.3 Organization of thesis

This thesis is organized as follows, Chapter 1 shows a brief introduction of the motivations to conduct the study as well as its goals. Chapter 2-4 present some fundamental theories of continuum fluid dynamics, the lattice Boltzmann method, and the level-set based topology optimization, respectively. The information in these theoretical parts are referenced in the following Chapter 5-6 wherein the topology optimization for flow field and thermal field are respectively represented. The main novel contribution is contained in these two chapters which can be found in the two publications associated with this thesis submission. Finally, some new findings and recognized issues in the use of LBM in topology optimization are sufficiently presented in Chapter 7 for a better improvement in the future development of the current work.

Chapter 2

Continuum Fluid Dynamics Theory

2.1 Navier-Stokes problem

2.1.1 Physical theory of fluid flow

The Navier-Stokes equation is a mathematical model to govern the motion of fluid flow in a physical medium [56]. It is, in general, contained a number of partial differential equations (PDEs) used to describe the behavior of various physical phenomena in science and engineering. To be more specific, the motion of fluid flows is driven by the number of physical properties characterized in the PDEs, such as physical density, velocity, and pressure.

For instance, the dynamic of the flow field can be characterized by following the conservation of the physical laws, i.e., the conservation of mass, momentum, and energy. Essentially, the physical quantities of a flow such as a velocity field, pressure field, and temperature field are the solutions of equations in a mathematical model wherein the conservations of mass, momentum, and energy are applied to a particular fluid domain. Those equations are respectively entitled as the continuity equation, the momentum equation, and the energy equation.

In principle [57, 58], the motion of fluid flow is possibly examined by using the approach of kinetic energy that is to derive the mathematical model of fluid dynamics. In the approach, there are two well-known different approaches can be used to observe the particle transportations, i.e., the Lagrangian method and the Euler method. In the first method, the observation of fluid-particle movement related to the coordinates of fluid-particle at

initial time t_0 and the coordinates of that particle at different time t_n. In the second method, the observation is done by using the fixed coordinates. Thus, the movement of a particular particle passing the fixed coordinates is associated with time and position. For example, let us assume the initial coordinates in two-dimensional (2D) space of a particular particle are x_0 and y_0, and for those at time t_n are x_n and y_n. The motion in the Lagrangian method is described as follows:

$$x_n = x_n(x_0, y_0, t_n), \tag{2.1a}$$

$$y_n = y_n(x_0, y_0, t_n). \tag{2.1b}$$

The motion in the Euler method at a particular time t_n is described as follows:

$$u_x = u_x(x_n, y_n, t_n), \tag{2.2a}$$

$$u_y = u_y(x_n, y_n, t_n), \tag{2.2b}$$

where $\boldsymbol{u} = (u_x, u_y)$ denotes the velocity at position (x_n, y_n) and time t_n.

By observing the motion of all particles in time and space, the behavior of the flow field can be governed, especially, the flow field is expressed through equations of continuity, momentum, and energy by the conservation equations in the two mentioned approaches. The derivation of those equations for fluid dynamics is not given in this study. However, the results are solely given for future reference through the study.

2.1.2 Governing equations

In continuum fluid mechanics, the well-known Navier-Stokes equations are a set of PDEs to describe the state of the flow field, in which the physical properties, i.e., the fluid density, fluid pressure, fluid velocity, and temperature denoted by $\rho, p, \boldsymbol{u}$, and T, respectively, are obtained by solving those PDEs. They are accordingly presented as follows:

The continuity equation:

$$\frac{\partial \rho}{\partial t} + \nabla \cdot (\rho \boldsymbol{u}) = 0, \tag{2.3}$$

where the first term denotes the rate of density and the second term denotes the mass flux that normal to a control surface. The incompressible flow exists when the density

ρ unchanged during flow transports, i.e., the first term in Eq. (2.3) is vanished and the second term reduces to

$$\nabla \cdot \boldsymbol{u} = 0. \tag{2.4}$$

The momentum equation:

$$\rho \frac{\partial \boldsymbol{u}}{\partial t} + \rho \nabla \cdot \boldsymbol{u}\boldsymbol{u} = -\nabla p + \mu \nabla^2 \boldsymbol{u}, \tag{2.5}$$

where the first term in the LHS denotes the rate of momentum, the second term in the LHS denotes the rate of convection momentum, the first term in the RHS denotes the pressure gradient, and the second term in the RHS denotes the diffusion term. Here, μ is the dynamic viscosity of the fluid. This equation is also known as the Navier-Stokes equation. It is noted that if the continuity equation (2.3) is substituted into the momentum equation (2.5), it deduces to the incompressible Navier-Stokes equations as follows:

$$\begin{cases} \rho \left(\dfrac{\partial \boldsymbol{u}}{\partial t} + (\boldsymbol{u} \cdot \nabla)\, \boldsymbol{u} \right) = -\nabla p + \mu \nabla^2 \boldsymbol{u}, \\ \nabla \cdot \boldsymbol{u} = 0. \end{cases} \tag{2.6}$$

To solve the incompressible Navier-Stokes equations (2.6), along with giving the appropriate conditions of initial state and boundary, another requirement is needed to enclose the problem of the fluid dynamic system, it is shown as follows:

The state equation:

$$p = \rho R T, \tag{2.7}$$

where R denotes the ideal gas constant.

2.1.3 Dimensionless form of governing equations

The governing equations in fluid dynamics are often introduced in dimensionless form. Among those various approaches, by characterizing the Reynolds number, the characteristics of flow can be associated with the Reynolds number. The dimensionalizing procedure

is done by introducing some dimensionless variables as follows:

$$\boldsymbol{u}^* = \frac{\boldsymbol{u}}{u_m}, \tag{2.8a}$$

$$p^* = \frac{p}{\rho u^2{}_m}, \tag{2.8b}$$

$$t^* = \frac{t u_m}{L}, \tag{2.8c}$$

$$\nabla^* = \nabla L, \tag{2.8d}$$

$$\mathrm{Re} = \frac{\rho u_m L}{\mu}, \tag{2.8e}$$

where the underscript m denotes the measured quantity, the asterisk $*$ denotes the non-dimensional quantity, L denotes the characteristic length used for the Reynolds number Re.

Taken the above dimensionalization into account, the non-dimensional form of the incompressible Navier-Stokes equations is, finally, constructed as follows:

$$\begin{cases} \dfrac{\partial \boldsymbol{u}^*}{\partial t^*} = \dfrac{1}{\mathrm{Re}} \nabla^{*2} \boldsymbol{u}^* - \left(\boldsymbol{u}^* \cdot \nabla^*\right) \boldsymbol{u}^* - \nabla^* p^*, \\ \nabla^* \cdot \boldsymbol{u}^* = 0. \end{cases} \tag{2.9}$$

It is note that all the non-dimensional forms are used throughout the entire thesis. Therefore, for the notational convenience, the asterisk notation $*$ will be implicitly dropped.

2.2 Heat conduction problem

2.2.1 Physical theory of heat conduction

Heat conduction is a process of energy transport from one to another region in contact, where there are different temperatures between the two regions [59]. In the microscopic point of view, the heat conduction mechanism process is visualized by the rate of exchange the molecular kinetic energy results in the thermal energy transfer from the higher temperature medium to the lower temperature medium in direct contact. In the heat conduction problem, the material flow is not considered in contribution to the transportation of thermal energy from a solid domain to the adjacent solid domain.

In a material medium, the existence of two types of conducting heat is remained, i.e., the vibration of molecular and the diffusion of the free-electron. In the former, if a solid object receives heat from the heat supplier, its molecules are started to vibrate

actively. They are, then, randomly collided with the surrounding molecules and transfer the kinetic energy to them. The neighbors gain some amount of energy and also started vibrating and transferring their kinetic energy to their neighbors through the collisions. This process is continued until they reach an equilibrium state. In the latter, the free-electron conductions happened when the electrons in a solid medium are released from molecules during heat energy is supplied. The free electrons are oriented to transport toward the lower temperature area and bump into the molecules in that area. By this means, they transfer some amount of energy to the molecules in the colder area. As a consequence, the heat is spread out to the lower temperature by the electron diffusion process.

By understanding the fundamentals of physical laws, the science of engineering can be built up in a strong foundation. Starting from the heat conduction law, which is also entitled Fourier's law, the rate of change of heat transfer passing a unit material area can be constructed by the relation with temperature gradient as follows:

$$\dot{Q} = -k\frac{dT}{d\boldsymbol{x}}, \tag{2.10}$$

where $\dot{Q}$ denotes the heat conduction rate, k denotes the thermal conductivity of the solid material, and $dT/d\boldsymbol{x}$ denotes the temperature gradient in the $\boldsymbol{x}$ direction. The negative sign of the equation indicates that the heat conduction rate is a positive variable since the temperature is a negative quantity on decreasing temperature direction.

The development of the heat conduction law to the heat conduction problem by means of energy balance will be summarized in the next section. Note that the fundamental theory for the heat conduction problem is merely studied in this thesis and that is not sufficient from the comprehensive theoretical analysis. Thus, for more detail on the development of the heat conduction law, it can be found in the literature [56].

2.2.2 Governing equations

In the Cartesian coordinates, the equation that governs the heat flow in an isotropic medium is designated as the heat conduction equation. Let us assume that $T(\boldsymbol{x}, t)$ denotes the scalar temperature field that respects to spacial position $\boldsymbol{x}$ and time t, the notation ∇^2 denotes the Laplacian, k denotes the thermal diffusivity coefficient, and S denotes the heat source in an inhomogeneous medium. The temperature T is, then, a solution of the

following heat equation:

$$\frac{\partial T}{\partial t} = k\nabla^2 T + S, \tag{2.11}$$

where $\partial T/\partial t$ denotes the time derivative of temperature T. In the case that the temperature is not varied by time, i.e., the time derivative $\partial T/\partial t = 0$, the Eq. (2.11) becomes the steady inhomogeneous heat conduction or entitled as Poisson's equation. It reads,

$$-k\nabla^2 T = S. \tag{2.12}$$

If the heat generation S is negligible in the Eq. (2.12), it becomes the homogeneous steady heat conduction or entitled as Laplace's equation as follows:

$$-k\nabla^2 T = 0. \tag{2.13}$$

It is noted that the time-variant heat conduction is not considered in the study, it is only interested in solving the two-dimensional steady heat conduction with various boundary conditions.

2.2.3 Boundary conditions

From the mathematical point of view, the solution for the steady heat conductions shown in the previous section may, however, depends on the boundary conditions specified at the surfaces [23]. The common types of those thermal conditions for the boundaries can be considered such as the prescribed temperature, prescribed heat flux, and the heat transfer boundary conditions. They are usually named as the Dirichlet, Neumann, and Robin boundary conditions, respectively.

I. *Dirichlet boundary condition*

This is the simplest boundary condition since the temperature of surfaces in a medium is easy to be measured in engineering. Also, this boundary condition is often used in an analytical solution. If the Dirichlet boundary condition is used, the temperature needs to be specified on the nodes placed on the surfaces. It is expressed as follows:

$$T(\boldsymbol{x}) = \bar{T} \quad \text{(on Dirichlet boundary)}, \tag{2.14}$$

where $\boldsymbol{x}$ denotes the position on the surface and $\bar{T}$ denotes the prescribed temperature, which is a constant in the steady case.

II. *The Neumann boundary condition*

The information related to the temperature gradient that normal to boundary surfaces will be specified in case of using the Neumann boundary condition. In this case, the prescribed normal heat flux needs to be given on the nodes that are located on the boundary surfaces as follows:

$$Q(\boldsymbol{x}) = -k\nabla T \cdot \boldsymbol{n} = \bar{Q} \quad \text{(on Neumann boundary)}, \tag{2.15}$$

where Q denotes the normal heat flux, $\bar{Q}$ denotes the specified normal heat flux, which is a constant in the steady case, ∇T denotes the temperature of the gradient, and $\boldsymbol{n}$ denotes the normal vector. In case the specified heat flux $\bar{Q} = 0$, the Neumann boundary condition becomes a specific case and entitled as the isolated boundary condition.

III. *Robin boundary condition*

This is a general boundary condition used in practice wherein the thermal energy balances at the surfaces, i.e., the thermal conduction at a surface equals the thermal convection considering the same direction. It is formulated as follows:

$$Q(\boldsymbol{x}) = -k\nabla T \cdot \boldsymbol{n} = h(T - T_\infty) \quad \text{(on Robin boundary)}, \tag{2.16}$$

where h denotes the heat transfer coefficient and T_∞ denotes the ambient temperature or the surrounding temperature of the surface.

It is note that this section mainly stated the fundamental theory for steady heat conduction problem needs for further development in our optimization problem. Therefore, one needs a more extensive analysis for the heat problem may refer to the comprehensive studies in literature [59, 56].

Chapter 3

The Lattice Boltzmann Method

In this section, the analysis of the lattice Boltzmann method for the incompressible Navier-Stokes flow and the thermal conduction will be discussed. Even though the analysis of the LBMs in this study is not extensive as compared to the comprehensive theory found in the literature of the continuum mechanics, its applications in topology optimization for flow field and thermal field are fairly covered. The readers should prefer to the existing researches [3, 4, 60, 5, 6] for more extensive analysis of the LBM for simulating various physical phenomena.

The start point from the kinetic theory, in which the state variable can be governed by the distribution of particle at position $\boldsymbol{x}$ and time t with particle velocity $\boldsymbol{c}$. As a result, the macroscopic variables such as the mass density $\rho(\boldsymbol{x}, t)$, the macroscopic velocity $\boldsymbol{u}(\boldsymbol{x}, t)$, and the total energy $E(\boldsymbol{x}, t)$ can be achieved from the first, second, and third order momentum, respectively, as follows:

$$\rho(\boldsymbol{x}, t) = \int f(\boldsymbol{x}, t, \boldsymbol{c})\ d\boldsymbol{c}, \tag{3.1}$$

$$\boldsymbol{u}(\boldsymbol{x}, t) = \frac{1}{\rho(\boldsymbol{x}, t)} \int \boldsymbol{c} f(\boldsymbol{x}, t, \boldsymbol{c})\ d\boldsymbol{c}, \tag{3.2}$$

$$E(\boldsymbol{x}, t) = \frac{1}{2}\rho(\boldsymbol{x}, t) \int \boldsymbol{c}^2 f(\boldsymbol{x}, t, \boldsymbol{c})\ d\boldsymbol{c}. \tag{3.3}$$

In kinetic theory, the well-known governing equation for describing the dynamical phenomena of those particle distribution functions $f(\boldsymbol{x}, t, \boldsymbol{c})$ is called the Boltzmann equation and described as follows:

$$\frac{\partial f}{\partial t} + \boldsymbol{c} \cdot \nabla f = \Omega\ , \tag{3.4}$$

where Ω denotes the collision operator. In this study, it employs the approximation Bhatnagar-Gross-Krook (BGK) model for the collision operator as follows:

$$\Omega = -\frac{1}{\tau_B}\left(f - f^{\mathrm{eq}}\right), \tag{3.5}$$

where τ_B denotes the relaxation time and f^{eq} denotes the Maxwell-equilibrium distribution function, it is defined as follows:

$$f^{\mathrm{eq}} = \rho\left(\frac{1}{2\pi RT}\right)^{d/2} \exp\left(-\frac{|\boldsymbol{c} - \boldsymbol{u}|^2}{2RT}\right), \tag{3.6}$$

where d denotes the dimensional space, R and T denote the gas constant and the temperature, respectively.

The Boltzmann equation (3.4) can be numerically solved by simply discretizing in time and space the continuous element of the equation (3.4), i.e., discretizing the continuous particle speed $\boldsymbol{c}$ to the set of directional vectors restricted in v directions, $\boldsymbol{c}_1, \boldsymbol{c}_2, \boldsymbol{c}_3, ..., \boldsymbol{c}_v$. As a consequence, the discrete Boltzmann equation can be written based on the discretization of the Boltzmann equation (3.4), as follows:

$$\mathrm{Sh}\frac{\partial f_i}{\partial t} + \boldsymbol{c}_i \cdot \nabla f_i = -\frac{1}{\tau_B}\left(f_i - f^{\mathrm{eq}}\right), \tag{3.7}$$

where f_i and f^{eq} denote the particle distribution and equilibrium distribution functions, respectively. $\mathrm{Sh} = U/c_s$ denotes the Strouhal number, where U denotes the speed of flow and c_s denotes the speed of sound. The left hand side of the Eq. (3.7) is called the propagation process (shown in Fig. 3.1) and the right hand side of the Eq. (3.7) is called the collision process (shown in Fig. 3.2). It is noted that the particle velocity $\boldsymbol{c}_i$ and the weighting function w_i must satisfy the following equations for the conservation of mass and momentum [61] such as follows:

$$\sum_{i=1}^{v} w_i = 1, \tag{3.8a}$$

$$\sum_{i=1}^{v} w_i c_{i\alpha} = 0, \tag{3.8b}$$

$$\sum_{i=1}^{v} w_i c_{i\alpha} c_{i\beta} = {c_s}^2 \delta_{\alpha\beta}, \tag{3.8c}$$

$$\sum_{i=1}^{v} w_i c_{i\alpha} c_{i\beta} c_{i\gamma} = 0, \tag{3.8d}$$

$$\sum_{i=1}^{v} w_i c_{i\alpha} c_{i\beta} c_{i\gamma} c_{\delta} = {c_s}^4 \left(\delta_{\alpha\beta}\delta_{\gamma\delta} + \delta_{\alpha\gamma}\delta_{\beta\delta} + \delta_{\alpha\delta}\delta_{\beta\gamma}\right). \tag{3.8e}$$

where $\delta_{\alpha\beta}$, $\delta_{\alpha\gamma}$, $\delta_{\alpha\delta}$, $\delta_{\beta\gamma}$, $\delta_{\beta\delta}$, and $\delta_{\gamma\delta}$ denote the Kronecker deltas by different Greek letters and must be followed by Einstein's summation rule. The weighting functions will be defined based on the lattice model of particle velocity.

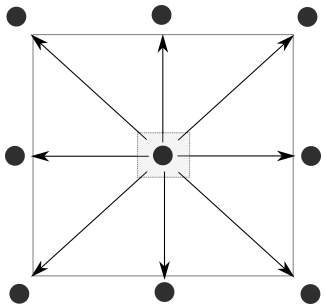

Figure 3.1: Propagation step.

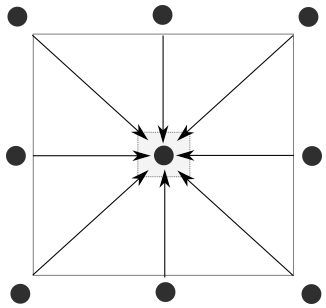

Figure 3.2: Collision step.

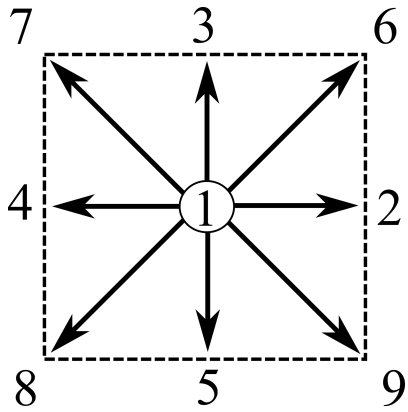

Figure 3.3: The demonstration of D2V9 lattice model.

Throughout the rest of this study, the two-dimensional nine-velocity (D2V9) lattice model is used for the LBMs corresponding to the solvers of the flow and thermal fields. Thus, $\boldsymbol{c}_i$ (the particle velocity) and w_i (the weighting function) in the D2V9 lattice model read the following equations:

$$\Big[\boldsymbol{c}_1, \boldsymbol{c}_2, \boldsymbol{c}_3, \boldsymbol{c}_4, \boldsymbol{c}_5, \boldsymbol{c}_6, \boldsymbol{c}_7, \boldsymbol{c}_8, \boldsymbol{c}_9\Big] = \begin{bmatrix} 0 & 1 & 0 & -1 & 0 & 1 & -1 & -1 & 1 \\ 0 & 0 & 1 & 0 & -1 & 1 & 1 & -1 & -1 \end{bmatrix}. \tag{3.9}$$

$$\begin{cases} w_1 = 4/9, \\ w_{2\text{-}5} = 1/9, \\ w_{6\text{-}9} = 1/36. \end{cases} \tag{3.10}$$

The D2V9 lattice model can be described in Fig. 3.3 by a finite set of 9 fixed velocity vectors including a stationary vector at its center.

3.1 Lattice Boltzmann method for Navier-Stokes flow

3.1.1 Method of computation

Regarding the discretization procedures by Inamuro et al. [62], by giving the lattice space Δx and the discrete time step Δt, the lattice Boltzmann equation for flow field can be derived from the discrete Boltzmann equation (3.7) with respect to the spacial position $\boldsymbol{x}$ at time t, it reads the following equation:

$$f_i\left(\boldsymbol{x}+\boldsymbol{c}_i\Delta x, t+\Delta t\right)-f_i\left(\boldsymbol{x}, t\right)=-\frac{1}{\tau_f}\left[f_i\left(\boldsymbol{x}, t\right)-f_i^{\mathrm{eq}}\left(\boldsymbol{x}, t\right)\right], \tag{3.11}$$

where τ_f denotes the single relaxation time of the lattice Boltzmann method, $f_i{}^{\mathrm{eq}}$ denotes the discrete equilibrium distribution function and it is given as follows:

$$f_i^{\mathrm{eq}}=w_i\rho\left[1+\frac{(\boldsymbol{c}_i\cdot\boldsymbol{u})}{c_s^2}+\frac{(\boldsymbol{c}_i\cdot\boldsymbol{u})^2}{2c_s^2}-\frac{|\boldsymbol{u}|^2}{2c_s^2}\right], \tag{3.12}$$

where the particle velocity $\boldsymbol{c}_i$ and the weighting function w_i are defined in Eqs. (3.9)-(3.10) for the D2V9 lattice scheme. The macroscopic density, velocity, pressure, and total energy are given as follows:

$$\rho(\boldsymbol{x}, t)=\sum_{i=1}^{9} f_i, \tag{3.13}$$

$$\boldsymbol{u}(\boldsymbol{x}, t)=\frac{1}{\rho}\sum_{i=1}^{9}\boldsymbol{c}_i f_i, \tag{3.14}$$

$$p(\boldsymbol{x}, t)=\frac{1}{3}\rho, \tag{3.15}$$

$$E(\boldsymbol{x}, t)=\frac{1}{2}\rho\sum_{i=1}^{9}\boldsymbol{c}_i\boldsymbol{c}_i f_i, \tag{3.16}$$

and the macroscopic viscosity ν is as follows:

$$\nu=\frac{1}{6}\tau_f\left(2-\frac{1}{\tau_f}\right)\Delta x. \tag{3.17}$$

By solving the time-evolution (3.11), the state variable can be determined accordingly. The presented LBM can be recovered exactly same the incompressible N-S equation (2.9) by using the asymptotic analysis [63] up to the second order of $O[\Delta x]^2$. The readers can refer to Inamuro et al. [61] for the extensive recovery procedures.

3.1.2 Initial and boundary conditions

Despite there are varieties of boundary conditions used in LBM for simulating the flow field, such applications are presented by Zhou and He et al. [64], and references therein. This part mainly concentrates on the boundary conditions used in this study. In LBM, the conditions for the initial state and boundaries need to be specified, especially, those macroscopic variables such as fluid velocity $\boldsymbol{u}$ and fluid pressure p are given to the conditions in order to implement the time-evolution LBM (3.11).

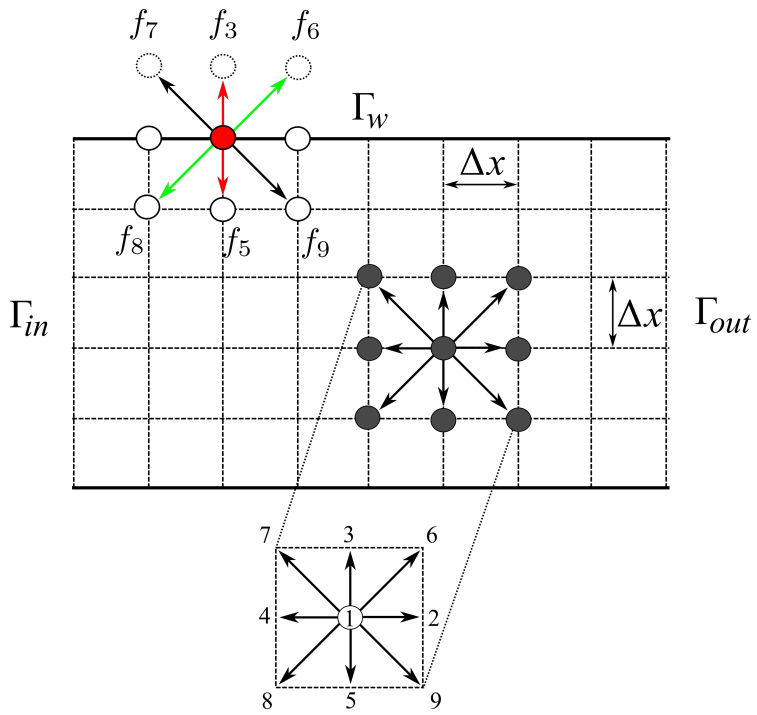

Figure 3.4: The demonstration of boundary conditions in D2V9 lattice model.

First, for initializing the initial state of all distribution functions, the initial values for fluid density and fluid velocity at time $t = 0$ are given. The initial state of all distribution functions is assumed to be at rest. Thus, all the distribution functions at position $\boldsymbol{x}$ and the initial time $t = 0$ are equivalent to the equilibrium state, it is defined as follows:

$$f_i(\boldsymbol{x}, 0) = f_i^{\mathrm{eq}}\left(\rho(\boldsymbol{x}, 0), \boldsymbol{u}(\boldsymbol{x}, 0)\right). \tag{3.18}$$

Next, this part highlights the boundary conditions used for simulating the flow field in this study. Fig. 3.4 shows the demonstration of boundary conditions in the D2V9 lattice model used for the analysis. The no-slip boundary value ($\boldsymbol{u} = 0$) is imposed on all

solid walls Γ_w, and the pairs prescribed velocity and prescribed pressure is imposed on the inflow-outflow ($\Gamma_{\text{in}}/\Gamma_{\text{out}}$), which placed at the vertical left and right ends, for example. They are respectively presented as follows:

$$\begin{cases} f_3(\boldsymbol{x},t) = f_5 \\ f_6(\boldsymbol{x},t) = f_8 \\ f_7(\boldsymbol{x},t) = f_9 \end{cases} \quad \text{on } \Gamma_w. \tag{3.19}$$

This no-slip boundary condition is also named as the bounce-back boundary condition [5]. It is, moreover, suited for implementing the boundary condition at conners by its simplicities.

The prescribed velocity boundary condition on Γ_{in} and prescribed pressure boundary condition on Γ_{out} written as follows:

$$\begin{cases} \rho(\boldsymbol{x},t) = \dfrac{f_1 + f_2 + f_4 + 2\left(f_5 + f_8 + f_9\right)}{1 - u_x} \\ f_4(\boldsymbol{x},t) = \underline{f_2} + \dfrac{2}{3}\rho\bar{u_x} \\ f_7(\boldsymbol{x},t) = \underline{f_9} + \dfrac{1}{6}\rho\bar{u_x} - \dfrac{1}{2}\left(f_3 - f_5\right) \\ f_8(\boldsymbol{x},t) = \underline{f_6} + \dfrac{1}{6}\rho\bar{u_x} + \dfrac{1}{2}\left(f_3 - f_5\right) \end{cases} \quad \text{on } \Gamma_{\text{in}}, \tag{3.20}$$

$$\begin{cases} u_x(\boldsymbol{x},t) = 1 - \dfrac{f_1 + f_2 + f_4 + 2\left(f_5 + f_8 + f_9\right)}{\bar{\rho}} \\ f_4(\boldsymbol{x},t) = \underline{f_2} + \dfrac{2}{3}\bar{\rho}u_x \\ f_7(\boldsymbol{x},t) = \underline{f_9} + \dfrac{1}{6}\bar{\rho}u_x - \dfrac{1}{2}\left(f_3 - f_5\right) \\ f_8(\boldsymbol{x},t) = \underline{f_6} + \dfrac{1}{6}\bar{\rho}u_x + \dfrac{1}{2}\left(f_3 - f_5\right) \end{cases} \quad \text{on } \Gamma_{\text{out}}, \tag{3.21}$$

where $\bar{u} = (\bar{u}_x, \bar{u}_y)$ denote the prescribed fluid velocity with x and y directions, $\bar{\rho}$ denotes the prescribed fluid density that imposed on boundaries at these vertical ends (Fig. 3.4). It is also noted that the symbol underlines denote the unknown distribution functions on boundaries.

3.1.3 Numerical verification

First, in the evaluation of the LBM solver for fluid flow, a direct comparison is performed with the analytical solution [65], though a numerical example to analyze the accuracy of the LBM used in this study. Considering the Navier-Stokes flow (2.9) that is driven by

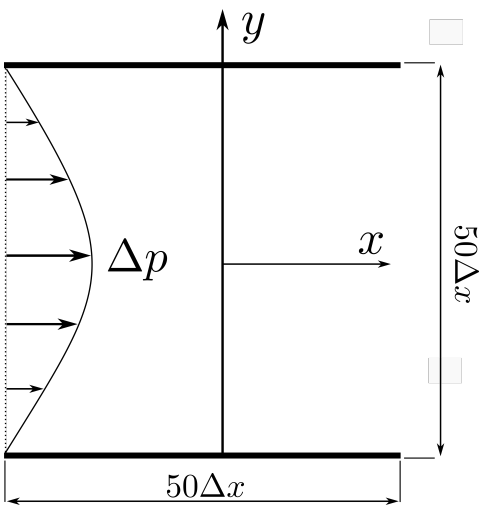

Figure 3.5: Design setting of the Poiseuille flow.

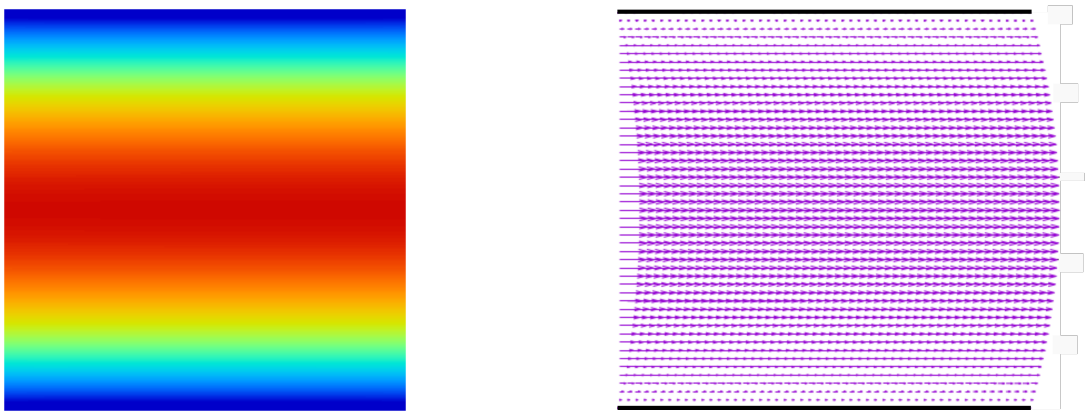

(a) The velocity contour

(b) The velocity vector

Figure 3.6: The results of Poiseuille flow obtained by LBM.

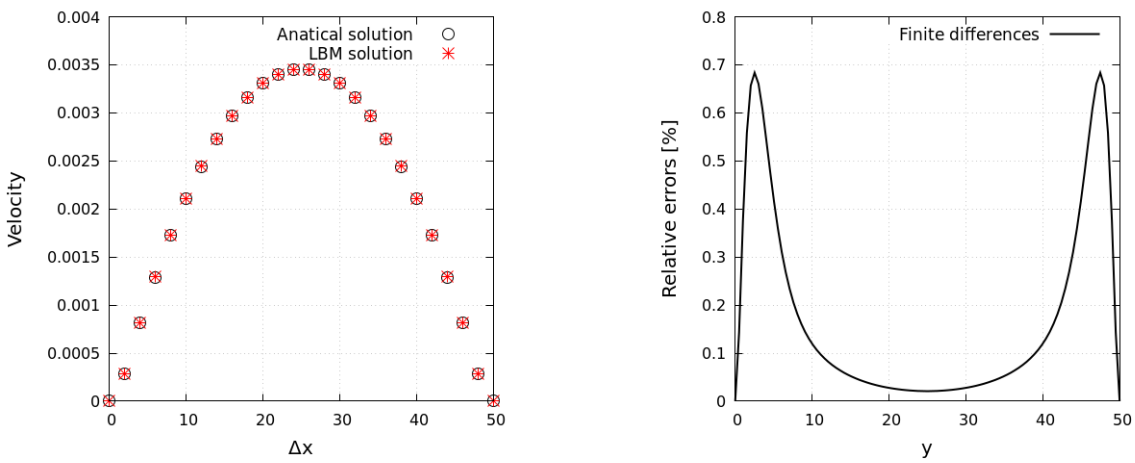

(a) Numerical solutions

(b) Finite differences

Figure 3.7: The comparison of analytical solution and the solution obtained by LBM.

the pressure gradient $\Delta p = [-\bar{p}, 0]$. The no-slip boundary condition ($\boldsymbol{u} = 0$) is used for the top and bottom horizontal boundaries (at $y = \pm a$). As a result, the analytical solution can be obtained by the following equation:

$$u_y = \frac{\bar{p}}{2\mathrm{Re}}\left(a^2 - y^2\right) \quad \text{here, } u_x = 0. \tag{3.22}$$

For the LBM solver, the governing equation (3.11) is used with the prescribed pressure boundary condition (3.21) is used at inlet and outlet. The design setting for the Poiseuille flow is shown in Fig. 3.5. Some of the specified conditions are given to solve this problem such as the $\tau_f = 1$, $\bar{p} = 1 \times 10^{-4}$, and the initial density is given at the equilibrium $\rho = 1$. The summary of these specified parameters used in this verification is shown in Tab. 3.1.

Table 3.1: The specified parameters used in the verification of LBM for flow field problem

Mesh size $[\Delta x]$	Re	Inlet width $[\Delta x]$	Pressure $\bar{p}$	Density ρ	Relaxation time τ_f
50×50	1/6	50	1×10^{-4}	1.0	1.0

With the above settings, the observations of the results obtained by the theoretical solution, and the results obtained by the lattice Boltzmann method are in good agreement, shown in Fig. 3.7. Also, the absolute error by mean of finite differences between the results obtained by the LBM and the theoretical solution is less than 1% at each point. The finite differences are computed by $\left(\frac{|u_{yL} - u_{yF}|}{u_{yL}} \times 100\right)$, where u_{yL} denotes the solution achieved by the LBM and u_{yF} denotes the solution achieved by the analytical solution at the selected lattice points (at x_{max}). It can be seen that the analysis is successful with the comparison of the two solvers. Fig. 3.6 shows the velocity field of the Poiseuille flow obtained by LBM. The parabolic profile at both inlet and outlet confirms the flow is fully developed. Therefore, the obtained results are considered as solutions.

3.2 Lattice Boltzmann method for heat conduction

3.2.1 Method of computation

This section will introduce the D2V9 lattice Boltzmann model for the thermal field corresponding to the heat conduction problem (2.13) shown in section 2.2 [11, 12, 13, 14]. The

following time-evolution lattice Boltzmann equation is used to govern the scalar temperature field T with the thermal diffusivity D. It is expressed as follows:

$$h_i\left(\boldsymbol{x}+\boldsymbol{c}_i\Delta x, t+\Delta t\right)-h_i\left(\boldsymbol{x}, t\right)=-\frac{1}{\tau_h}\left[h_i\left(\boldsymbol{x}, t\right)-h_i^{\mathrm{eq}}\left(\boldsymbol{x}, t\right)\right]+\Omega_i'\left(\boldsymbol{x}, t\right). \tag{3.23}$$

Here, $h_i(\boldsymbol{x}, t)$ denotes the thermal distribution function, τ_h denotes the single relaxation time, the particle velocity $\boldsymbol{c}_i$ and the weights w_i are shown in Eqs. (3.9-3.10). The force term $\Omega_i{}' = w_i S D \Delta x$ does not exist in the homogeneous heat conduction problem (equals the Laplace's equation (2.13), $\Omega_i{}' = 0$) while S equals the inhomogeneous term (heat source) in the inhomogeneous heat conduction problem (equals the Poisson's equation (2.12), $\Omega_i{}' \neq 0$). The thermal equilibrium distribution function denoted by $h_i{}^{\mathrm{eq}}$ as follows:

$$h_i^{\mathrm{eq}}=w_i T \quad \text{for} \quad i=1,2,3,\ldots 9. \tag{3.24}$$

The state variable such that temperature T is represented in term of concentration of the thermal distribution function $h_i{}^{\mathrm{eq}}(\boldsymbol{x}, t)$ as follows:

$$T=\sum_{i=1}^{9} h_i=\sum_{i=1}^{9} h_i^{\mathrm{eq}}. \tag{3.25}$$

The thermal diffusivity D and thermal conductivity k are defined as follows:

$$D=\frac{1}{6}\tau_h\left(2-\frac{1}{\tau_h}\right)\Delta x, \tag{3.26}$$

$$k=\frac{1}{3}\tau_h\Delta x. \tag{3.27}$$

The readers can refer to Inamuro et al. [61] for the recovery of the time-evolution LBM (3.23) from the heat equation (2.13) by using the asymptotic theory.

3.2.2 Initial and boundary conditions

Typically in LBM, in order to solve the time-evolution equation, the specified equation is required for the initial and boundary conditions. Those conditions are generally given in terms of macroscopic variables, as such in the flow problem and also in the thermal problem. As similar in the previous Subsection 3.1.2, the macroscopic T at a position $\boldsymbol{x}$ and the initial time $t = 0$ is given to compute the rest-state of all particle distribution functions. The initial condition is as follows:

$$h_i(\boldsymbol{x}, 0)=h_i{}^{\mathrm{eq}}\left(T(\boldsymbol{x}, 0)\right). \tag{3.28}$$

As described in the previous studies [12, 55] for typical boundaries condition used in the heat conduction problem, this part will present three general types of Dirichlet, Neumann, and Robin boundary condition used for the presented LBM. It is noted that the typical feature of propagating of the particle distribution functions placed on the solid boundary nodes requires some assumtions for deriving the boundary conditions. In such assumptions, the distributions that meet the condition $\boldsymbol{c}_i \cdot \boldsymbol{n} > 0$ are unknown (shown in Fig. 3.8), where $\boldsymbol{n}$ denotes the normal vector [66]. They need to be specified from boundary conditions to compute the macroscopic variables. On the solid bounday node ($\boldsymbol{x} \in \Gamma_{\text{wall}}$), the unknown distribution functions h_i^{unknown} are defined as follows:

$$h_i^{\text{unknown}} = w_i \bar{T}' \quad \text{for} \quad \boldsymbol{c}_i \cdot \boldsymbol{n} > 0, \tag{3.29}$$

where $\bar{T}'$ denotes the unknown temperature.

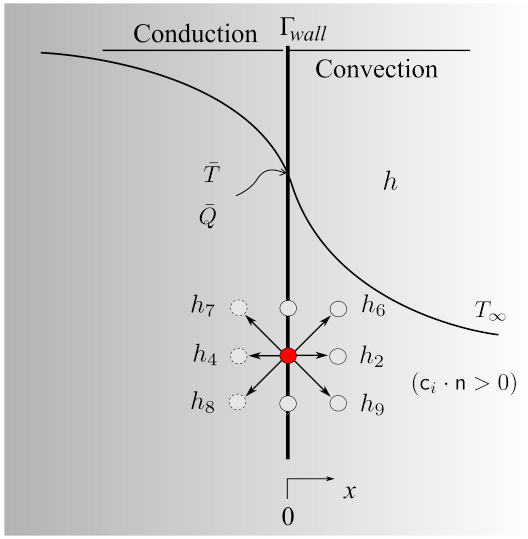

Figure 3.8: The demonstration of boundary conditions in D2V9 lattice model for the heat conduction problem.

The prescribed temperature $\bar{T}$, the prescribed heat flux $\bar{Q}$ or the heat transfer constant h and the ambient temperature T_∞ are specified on the boundary nodes or given on the cases that the Dirichlet (Γ_D), the Neumann (Γ_N), or the Robin (Γ_h) boundary conditions are used, respectively. They are presented as follows:

$$h_i^{\text{unknown}} = w_i \frac{\bar{T} - \sum_{i(\boldsymbol{c}_i \cdot \boldsymbol{n} \leq 0)} h_i}{\sum_{i(\boldsymbol{c}_i \cdot \boldsymbol{n} > 0)} w_i} \qquad \text{on } \Gamma_D. \tag{3.30}$$

$$h_i^{\text{unknown}} = w_i \frac{\bar{Q} - \sum_{i(\boldsymbol{c}_i \cdot \boldsymbol{n} \leq 0)} h_i \boldsymbol{c}_i \cdot \boldsymbol{n}}{\sum_{i(\boldsymbol{c}_i \cdot \boldsymbol{n} > 0)} w_i \boldsymbol{c}_i \cdot \boldsymbol{n}} \quad \text{on } \Gamma_N. \tag{3.31}$$

$$h_i^{\text{unknown}} = \tilde{h}_i \left(\frac{1 + 3h\Delta x}{1 - 3h\Delta x} \right) \qquad \text{on } \Gamma_h. \tag{3.32}$$

where the unknown thermal distribution functions $h_i^{\text{unknown}} = h_2, h_6,$ and h_9 and the known distribution functions are $h_1, h_3, h_4, h_5, h_7,$ and h_8 according to the demonstration on Fig. 3.8. The notation tilde (in the Eq. (3.32)) denotes the opposite distribution functions of the unknown components, e.g., $h_2 \leftrightarrow h_4$, $h_6 \leftrightarrow h_8$, and $h_9 \leftrightarrow h_7$.

It is noted that the ambient temperature $T_\infty = 0$ is implicitly used in the Eq. (3.32). For the detailed analysis on the derivations of these boundary conditions, it can be easily found in literature [66, 12, 55].

3.2.3 Numerical verification

To evaluate the LBM solver used in this study, this numerical example conducts a direct comparison to the well-known FEM solver in a heat diffusion problem, i.e., the FreeFEM++ solver. The PDE which often called the heat equation used in this numerical simulation is written as follows:

$$\begin{cases} -\nabla^2 T = 0 & \text{in } \Omega, \\ \bar{T} = 100 & \text{on } \Gamma_u, \\ \bar{T} = 0 & \text{on } \Gamma_q. \end{cases} \tag{3.33}$$

This numerical simulation is defined in a square domain of $100\Delta x \times 100\Delta x$ lattice grid. In order to ensure the identical conditions used in the two approaches, the framed triangulate unit mesh of a $100\Delta x \times 100\Delta x$ lattice size is also used in the FreeFEM++ simulation tool. The Galerkin finite element scheme (P1) is employed to solve the heat equation (3.33) in the FEM approach in comparison to the constructed LBM. For the manual of implementation of the FreFEM++ application, the readers are suggested to Hecht et al. [67]. Moreover, some conditions used in the constructed LBM are specified in this numerical example, such as the relaxation time $\tau_h = 1$, the initial condition $h_i(x, 0) = 0$, and the accuracy is up to 10^{-6} in the LBM.

The summary of these specified parameters used in this verification is shown in Tab. 3.2. Figure 3.9 shows the design settings of the boundary value problem (BVP) (3.33). It is initially fulfilled by the material in a square area Ω. The prescribed temperature condition is specified on all the vertical and horizontal edges of the design domain. The

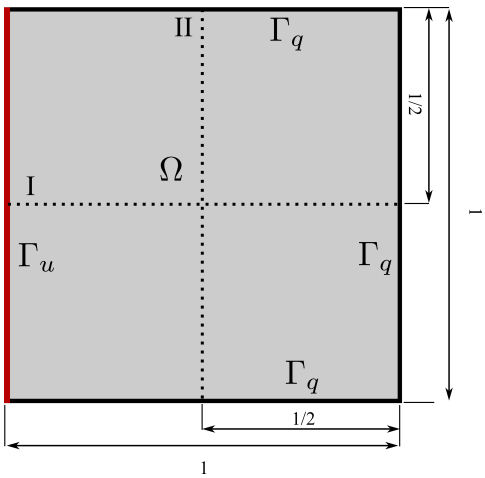

Figure 3.9: Design setting of the Laplace problem.

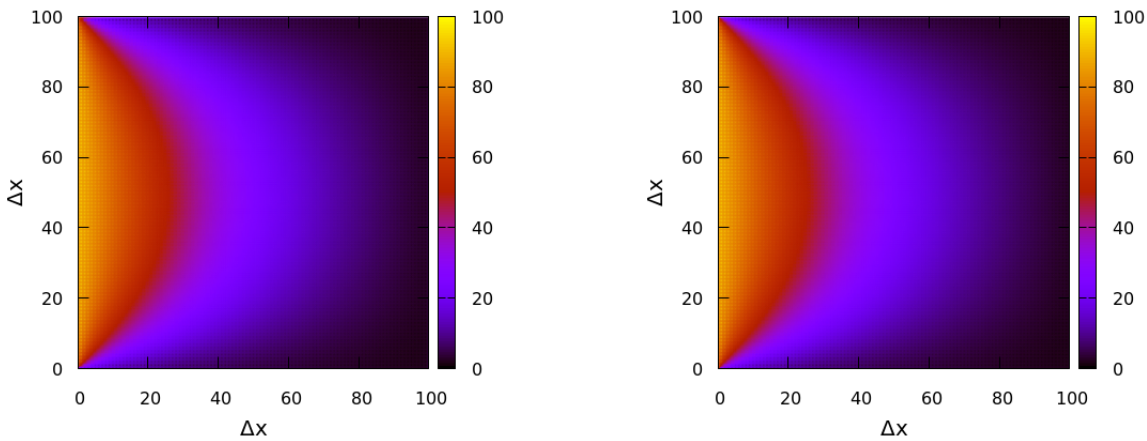

(a) FEM approach

(b) LBM approach

Figure 3.10: The results of the Laplace problem obtained by the two different methods.

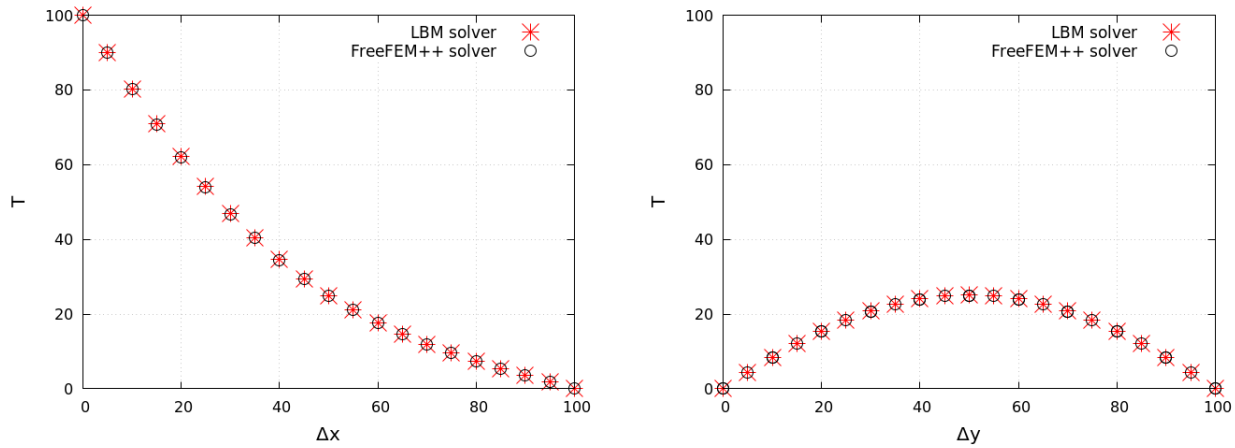

(a) Line I

(b) Line II

Figure 3.11: The result of Laplace problem plotted on the center lines I and II.

Table 3.2: The specified parameters used in the verification of LBM for the heat diffusion

Mesh size $[\Delta x]$	FreeFEM++ solver	Boundary condition $\bar{T}$ (Γ_u)	Boundary condition $\bar{T}$ (Γ_q)	Initial condition $h_i(x,0)$	Relaxation time τ_h
100×100	P1	100	0	0	1.0

prescribed temperature $\bar{T} = 100$ is imposed on the vertical left end (Γ_u) while the prescribed temperature $\bar{T} = 0$ is imposed on all the other edges (Γ_q) of the design domain Ω.

As a result, the solutions of the BVP obtained by the two methods are identical. Fig. 3.10 shows a good agreement of the temperature distribution obtained by the LBM solver and the FEM solver. The finite differences of the results obtained by the two approaches are also examined to robust the comparison. In this examination, the observation points are selected on the horizontal centerline I and the vertical centerline II of the design domain Ω. The results recorded at the observation points by the LBM are denoted by T_{obsL} and for those of the FEM are denoted by T_{obsF}. The finite differences of the results obtained by by the two solvers at the observation points are calculated by $\left(\frac{|T_{obsL}-T_{obsF}|}{T_{obsL}} \times 100\right)$. Consequently, it is shown in Fig. 3.11, the results recorded at the observation points on the centerlines II and II are observed with a good agreement over this comparison. To be more specific, it is observed that the finite differences are less than 0.25% noticed on all observation nodes on line I and the finite differences are less than 0.3% noticed on all observation nodes on line II. This simulation indicates that the reasonable accuracy of the LBM in this study for solving the heat equation.

Chapter 4

Level-set Based Topology Optimization

A general statement of a topology optimization for a fixed design domain $D \subset \mathbb{R}^d$ (where $d = 2$ denotes two-dimentional space in the study) which includes a computational domain $\Omega \subset D$, can be given as follows:

$$\begin{aligned} &\text{Minimize} \quad J, \\ &\text{subject to} \quad F(f) = 0 \quad \text{on } \Omega, \end{aligned} \tag{4.1}$$

where J denotes an objective functional and F is a numerous equations with respect to the state variable f that to govern the current state.

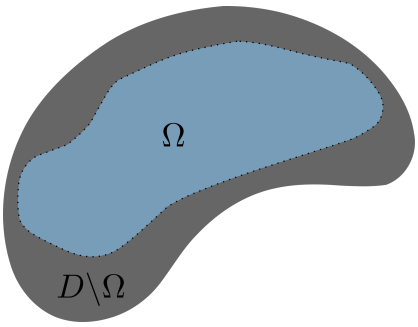

Figure 4.1: Demonstration of the fixed design domain D and computational domain Ω.

In this study, the method of optimization based on the level-set method [68] in which the adjoint method is used to find the continuous sensitivity and/or the topological derivative to help finding the optimal geometries [69, 70].

4.1 Level-set based topology optimization

The level-set method [71, 72, 73, 74] is formulated as such a numerical method for expressing interfaces/structural boundaries in a fixed design domain. In structural optimization problem, the level-set function $\phi(\boldsymbol{x})$ is used to express the interfaces/structural boundaries $\partial\Omega$ between the material region Ω and the void region $D\backslash\Omega$ in a fixed design domain D, it is formulated as follows:

$$\begin{cases} \phi(\boldsymbol{x}) = 0 & \text{if} \quad \boldsymbol{x} \in \partial\Omega, \\ \phi(\boldsymbol{x}) > 0 & \text{if} \quad \boldsymbol{x} \in \Omega\backslash\partial\Omega, \\ \phi(\boldsymbol{x}) < 0 & \text{if} \quad \boldsymbol{x} \in D\backslash\Omega, \end{cases} \tag{4.2}$$

where $\boldsymbol{x}$ denotes a particular position in the domain D.

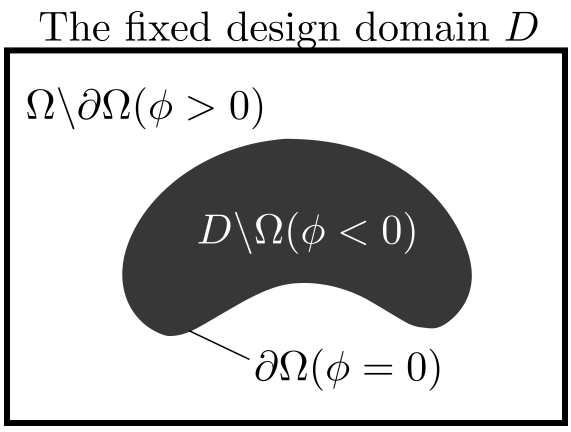

Figure 4.2: Demonstration of the level-set function.

By introducing a fictitious time t, the general approach for modeling the time-evolution level-set function that to solve the Hamilton-Jacobi equation [75, 76] is as follows:

$$\frac{\partial\phi(\boldsymbol{x},t)}{\partial t} = -\upsilon(\boldsymbol{x},t)\,|\nabla\phi(\boldsymbol{x},t)| \quad \text{in } D, \tag{4.3}$$

where $\upsilon(\boldsymbol{x},t)$ denotes the velocity of moving boundary that is normal to the structural boundaries. By solving the time-evolution equation (4.3), the structural optimization is replaced with the material distribution problem and without the existing of intermediate values/gray scales. It is, however, still remained a problem such that the new holes are not allowed during the optimization process, even though it is allowed to reduce the number of existing holes during topological changes [77]. The problem is, therefore, considered as

shape optimization problem [78, 79, 80, 81] wherein the normal speed of moving boundary $\upsilon(\boldsymbol{x}, t)$ is, essentially shape derivative.

Next, to overcome these problems discussed in literature for topology optimization problem, Yamada et al. [68] proposed a new level-set method that lies on the phase field method [82, 83, 84]. In his research, the scalar function $\phi(\boldsymbol{x})$ is defined using the sets of positive and negative values to introduce the existence of the material domain Ω, the void domain $D\backslash\Omega$, and the interfaces $\partial\Omega$ of them in the fixed design domain D. By adding the upper and lower bounds to the level-set function $\phi(\boldsymbol{x})$ in (4.2), the new level-set function is now become as follows:

$$\begin{cases} 1 \geq \phi(\boldsymbol{x}) > 0 & \text{if} \quad \boldsymbol{x} \in \Omega\backslash\partial\Omega, \\ \phi(\boldsymbol{x}) = 0 & \text{if} \quad \boldsymbol{x} \in \partial\Omega, \\ 0 > \phi(\boldsymbol{x}) \geq -1 & \text{if} \quad \boldsymbol{x} \in D\backslash\Omega, \end{cases} \tag{4.4}$$

where $\boldsymbol{x}$ is a position in a fixed domain D. It is, moreover, the method of updating the topological change by solving the Eq. (4.3) replaced by the new reaction-diffusion equation in his research. It is defined as follows:

$$\frac{\partial\phi}{\partial t} = -K\left(\mathcal{T}_D J - \tau\nabla^2\phi\right) \quad \text{in } D, \tag{4.5}$$

where $K > 0$ denotes the proportionality, $\mathcal{T}_D J$ denotes the topological sensitivity of the objective function J, t denotes the fictitious time, and τ denotes the regularization parameter which is designedly used to control the complexities of the obtained topological shapes. Unlikely, the time-evolution equation (4.3) that only suits for the shape optimization while the time-evolution equation (4.5) allows the creation of new holes or allows merging different holes during optimization process. Thus, this method is suited for the topology optimization with the advantage of controlling the complications of the optimal results.

The application and discussion of the reaction-diffusion equation (4.5) in topology optimization for flow field and thermal field will be discussed in the next sections. Also, the analysis of the sensitivity of the objective function that denotes by the reaction term in Eq. (4.5) will be given later, as well as the initial and boundary conditions to solve this time-evolution equation.

4.2 The adjoint method and sensitivity analysis

Reconsidering the optimization problem in (4.1) in which the objective is to minimize or maximize the cost function $J(\alpha, u(\alpha))$, where $F(\alpha, u(\alpha)) = 0$ is a set of governing equations to govern the behavior of fluid/structure states. Also, α denotes the control variable and $u(\alpha)$ denotes the state variable that regards to the change in control variable. The most popular algorithm to find the optimal solution is based on the gradient information of the cost function $J(\alpha, u(\alpha))$ with respect to the control variable α. The derivative of $J(\alpha, u(\alpha))$ can be computed by using the following chain rule:

$$\frac{dJ(\alpha, u(\alpha))}{d\alpha} = \frac{\partial J(\alpha, u(\alpha))}{\partial \alpha} + \frac{\partial J(\alpha, u(\alpha))}{\partial u(\alpha)} \frac{\partial u(\alpha)}{\partial \alpha} \tag{4.6}$$

To analytically compute the gradient of $J(\alpha, u(\alpha))$ in the above equation, the so-called direct method [85, 86] or adjoint method [87, 88] can be efficiently applied. The general analyses of the two methods will be produced in the following sections.

4.2.1 The direct and adjoint methods

I. *The direct method*

Let us define the state system with respect to the control variable α denoted by $F(\alpha, u(\alpha))$. The gradient of F with respect to α is introduced as follows:

$$\frac{dF(\alpha, u(\alpha))}{d\alpha} = \frac{\partial F(\alpha, u(\alpha))}{\partial \alpha} + \frac{\partial F(\alpha, u(\alpha))}{\partial u(\alpha)} \frac{\partial u(\alpha)}{\partial \alpha} = 0 \tag{4.7}$$

Assuming the above equation is solvable. Thus, the expression of the gradient of the state variable $u(\alpha)$ with respect to the control variable α can be written as follows:

$$\frac{\partial u(\alpha)}{\partial \alpha} = -\left(\frac{\partial F(\alpha, u(\alpha))}{\partial u(\alpha)}\right)^{-1} \frac{\partial F(\alpha, u(\alpha))}{\partial \alpha} \tag{4.8}$$

Next, inserting the differential equation above to the Eq. (4.6), it deduces to the so-called direct derivative. It yields

$$\frac{dJ(\alpha, u(\alpha))}{d\alpha} = \frac{\partial J(\alpha, u(\alpha))}{\partial \alpha} - \frac{\partial J(\alpha, u(\alpha))}{\partial u(\alpha)} \left(\left(\frac{\partial F(\alpha, u(\alpha))}{\partial u(\alpha)}\right)^{-1} \frac{\partial F(\alpha, u(\alpha))}{\partial \alpha}\right). \tag{4.9}$$

Here, $\partial J(\alpha, u(\alpha))/\partial \alpha$ and $\partial J(\alpha, u(\alpha))/\partial u(\alpha)$ can be analytically computed using the expression of the given objective function J. Therefore, computing the derivative $dJ(\alpha, u(\alpha))/d\alpha$ will not be so computationally expensive if the number of design variable is small, since

its cost is proportional to the number of design variable α and the dimension of the state variable u. In other cases, if the number of design variable is large, e.g., in fluid/structure optimization problems, the use of the so-called adjoint method is significantly efficient more than the proposed direct method [70, 89].

II. *The adjoint method*

From the Eq. (4.9), a new expression for the derivative of the objective function J with respect to the design variable α can be defined as follows:

$$\frac{dJ(\alpha, u(\alpha))}{d\alpha} = \frac{\partial J(\alpha, u(\alpha))}{\partial \alpha} - \left(\left(\frac{\partial F(\alpha, u(\alpha))}{\partial u(\alpha)} \right)^{-T} \frac{\partial J(\alpha, u(\alpha))}{\partial u(\alpha)} \right) \frac{\partial F(\alpha, u(\alpha))}{\partial \alpha} \tag{4.10}$$

By introducing the Lagrangian multiplier $\boldsymbol{p}$ named as the so-called adjoint variable. It is regarded to the state variable $u(\alpha)$ as follows:

$$\left(\frac{\partial F(\alpha, u(\alpha))}{\partial u(\alpha)} \right)^{T} \boldsymbol{p} = \frac{\partial J(\alpha, u(\alpha))}{\partial u(\alpha)}, \tag{4.11}$$

where the term $\partial J(\alpha, u(\alpha))/\partial u(\alpha)$ denotes the source term of the so-called adjoint system Eq. (4.11) regarding the given cost function J. The advantage of using the above adjoint equation (4.11) is the efficient computation of the derivative of the cost function $J(\alpha, u(\alpha))$ with whatever size of the design variable α. To be more specific, to solve the Eq. (4.10), especially, in a topology optimization problem where there is a large number of design variable α, the computational cost is used to compute the variation of the state system with respect to the control variable α ($\partial F(\alpha, u(\alpha))/\partial \alpha$ in Eq. (4.10)) is extremely huge. However, by using the adjoint system Eq. (4.11), the variation of the state system with respect to the control variable α ($\partial F(\alpha, u(\alpha))/\partial \alpha$) is correspondingly eliminated. Thus, the variation of the state system with respect to the control variable α is free of computation with whatever size of α. Additionally, it is only needed to solve the new defined adjoint equation (4.11). The derivative of $J(\alpha, u(\alpha))$ becomes

$$\frac{dJ(\alpha, u(\alpha))}{d\alpha} = \frac{\partial J(\alpha, u(\alpha))}{\partial \alpha} - \boldsymbol{p}^{T} \frac{\partial F(\alpha, u(\alpha))}{\partial \alpha}. \tag{4.12}$$

The adjoint method is extremely helpful in topology optimization problem wherein the number of design variable α is large. However, the requirement of developing a new adjoint solver may be difficult in some cases such that solving the highly non-linear PDEs [90]. To this end, the automatic differentiation [91] can be considered as an possibility to achieve those adjoint solutions for the optimization problems.

4.2.2 Methods of sensitivity computation

I. *Continous derivative*

The continuous design sensitivity [92, 93, 94] is commonly obtained along with the differentiation of a set of state equations that governs the behavior of fluid/structure. Usually, it can be a set of PDEs. For instance, let us assume the variation of a given objective function J that responded by the small changes in the design variable s at a particular point, named as $\delta_s J$. It denotes $(s + \varepsilon\eta)$ as the perturbation field, where ε denotes the perturbation variable and η denotes the arbitrary function. Thus, the variation of the objective function J caused by the perturbation of a design variable can be defined as follows:

$$\delta_s J = \lim_{\varepsilon \to 0} \frac{J[s + \varepsilon\eta] - J[s]}{\varepsilon}. \tag{4.13}$$

It can be computed numerically and reflect the change in the original design domain. The application and discussion on how to use the Eq. (4.13) in the field of fluid/structure topology optimization will be given in Section 5.1.2. It is noted that $\delta_s J$ is a linear function that respects the coefficient of the design change η. The readers may refer to [69] for more detailed analysis.

II. *Topological derivative*

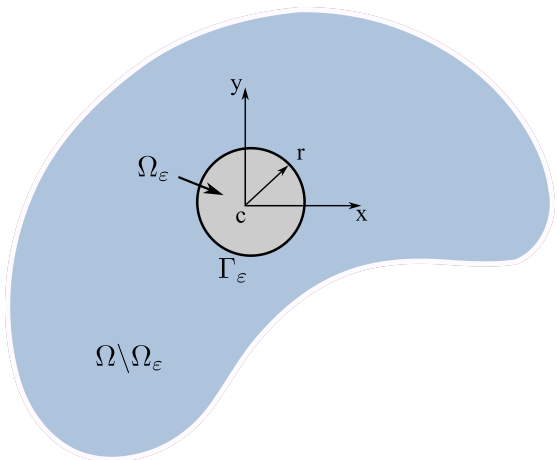

Figure 4.3: Demonstration of the topological derivative concept.

The topological derivative [95, 96, 97] is an analytical method to predict the possibility

of the topological change that affects the variation of the objective function J. In the method, the topological change can be considered as the nucleation or the inclusion of an infinitesimal material/solid circular in the original domain. For instance, let us assume the variation of a given objective function J in a computational domain Ω by the small perturbation corresponds to the inserting/removing of a small circular material/solid ball Ω_ε with radius $|r|$ and boundary Γ_ε (at the particular point with center c) named as $\mathcal{T}_D$. Thus, the variation of the objective function caused by the topological change at a particular point in the interior domain can be defined as follows:

$$\mathcal{T}_D J = \lim_{\varepsilon \to 0} \frac{J\left(\Omega \backslash \Omega_\varepsilon(c)\right) - J(\Omega)}{|\Omega_\varepsilon(c)|}. \tag{4.14}$$

It is noted that the topological derivative $\mathcal{T}_D J$ can appear with a positive or negative sign that predicts the increase or decrease of the objective function J by the topological change at the optimal point. The application and discussion on how to use the Eq. (4.14) in the field of structure/fluid topology optimization will be given in Subsection 6.1.2.

Chapter 5

Topology Optimization for Flow Field Problem using LBM

5.1 Formulation for a topology optimization

5.1.1 Level-set based topology optimization for flow field problem

In this study, the scalar level-set function $\phi(\boldsymbol{x})$ is used to express the solid distribution $D\backslash\Omega$, the fluid distribution Ω, and the structural boundaries $\partial\Omega$ in a fixed design domain D. It is defined as follows:

$$\begin{cases} 1 \geq \phi(\boldsymbol{x}) > 0 & \boldsymbol{x} \in \Omega\backslash\partial\Omega, \\ \phi(\boldsymbol{x}) = 0 & \boldsymbol{x} \in \partial\Omega, \\ 0 > \phi(\boldsymbol{x}) \geq -1 & \boldsymbol{x} \in D\backslash\Omega, \end{cases} \tag{5.1}$$

where $\boldsymbol{x}$ denotes a particular point in a fixed design domain D. Moreover, the characteristic function $\chi_\phi(\boldsymbol{x})$ is used to define the existence of fluid in the entire design domain. It is associated with the level-set function (5.1) and expressed as follows:

$$\chi_\phi(\boldsymbol{x}) = \begin{cases} 1 & \text{if} \quad \phi(\boldsymbol{x}) \geq 0, \\ 0 & \text{if} \quad \phi(\boldsymbol{x}) < 0. \end{cases} \tag{5.2}$$

Next, considering the method of updating the new design variables in an optimization problem. The time-evolution equation [68, 32, 98, 99] is selected in this study to solve the problem of finding optimal shapes with the help of the gradient of a given objective

function J. The expression is shown as follows:

$$\begin{aligned}
&\frac{\partial \phi}{\partial t} = -K\left(\bar{J}' - \tau\nabla^2\phi\right) && \text{in } D,\\
&\phi|_{t=0} = \phi_0 && \text{in } D,\\
&\frac{\partial \phi}{\partial \boldsymbol{n}} = 0 && \text{on } \partial D\backslash\Gamma_w,\\
&\phi = -1 && \text{on } \Gamma_w,
\end{aligned} \tag{5.3}$$

where $K > 0$ denotes a proportional constant, $\bar{J}'$ denotes the design sensitivity of an objective function J which has a great contribution in predicting the feasible shapes, τ is a regularization parameter, ϕ_0 is an initial value of level-set function ϕ at an initial fictitious time $t = 0$, and Γ_w is the non-design boundary.

In order to determine the optimal topologies of flow field that minimize/maximize an objective function J, the optimization problem can be constructed as follows:

$$\min_{\phi} J|_{t=t_1} = \int_I \int_\Omega A\left(\rho, \nabla\boldsymbol{u}\right)\, d\Omega dt + \int_I \int_\Gamma B\left(\rho, \boldsymbol{u}\right)\, d\Gamma dt,$$

subject to:

$$\begin{aligned}
&\text{G.E.} && \frac{\partial f}{\partial t} + \boldsymbol{c}.\nabla f + \frac{1}{\tau_B}\left(f - \hat{f}^{\text{eq}}\right) && \text{in } I\times D\times\mathbb{R}^2,\\
&\text{I.C.} && f|_{t=0} - f_0 = 0 && \text{in } D\times\mathbb{R}^2,\\
&\text{B.C.} && \begin{cases} f\left(\boldsymbol{c}\right) - f\left(-\boldsymbol{c}\right) = 0 & \text{on } I\times\Gamma_w\times\mathbb{R}^2{}_{\boldsymbol{n}.\boldsymbol{c}<0},\\ f\left(\boldsymbol{c}\right) - f^{\text{eq}}\left(\rho, \overline{\boldsymbol{u}}, \chi_\phi\right) = 0 & \text{on } I\times\Gamma_{\text{in}}\times\mathbb{R}^2,\\ f\left(\boldsymbol{c}\right) - f^{\text{eq}}\left(\overline{\rho}, \boldsymbol{u}, \chi_\phi\right) = 0 & \text{on } I\times\Gamma_{\text{out}}\times\mathbb{R}^2, \end{cases}
\end{aligned} \tag{5.4}$$

and

$$V = \int_D \chi_\phi d\Omega - V_{\max} \leq 0 \qquad \text{volume constraint.}$$

Here, $J|_{t=t_1}$ denotes the objective functional that can be specified in the internal domain or on the boundary domain. It is noted that the objective functional is judged after an arbitrary time (t_1), until it meets the termination conditions. In this study, the structural boundary is a set of $\Gamma = \Gamma_{\text{in}} \cup \Gamma_{\text{out}} \cup \Gamma_w$ boundaries, where Γ_{in}, Γ_{out} and Γ_w denote the prescribed velocity inlet boundary, the prescribed pressure outlet boundary, and the boundary between solid and fluid regions defined as the bounce-back boundary, respectively. The real objective functionals A and B are specified in fluid region Ω or on structural boundary Γ, $\boldsymbol{u}$ denotes the fluid velocity, $\nabla\boldsymbol{u}$ denotes the gradient of velocity, $\bar{u}$ is the prescribed

fluid velocity at the inlet, $\bar{\rho}$ is the prescribed density at the outlet, V denotes the volume constraint, and $V_{\max}$ denotes the permissible fluid volume.

Next, in order to evolve the time-evolution (5.3) implicitly, the adjoint method [100] is used and the design sensitivity is, then, obtained by using the solutions of the primal equation (5.4) and the following adjoint equation (5.5):

$$-\frac{\partial g}{\partial t} - \boldsymbol{c} \cdot \nabla g = -\frac{1}{\tau_B}(g - g^{\mathrm{eq}}) \qquad \text{in } I \times D \times \mathbb{R}^2, \tag{5.5}$$

$$\left.\begin{aligned} g|_{t=t_1} &= \mp A^{'} && \text{in } D \times \mathbb{R}^2, \\ g|_{t=t_1} &= g^{\mathrm{eq}}_{\mathrm{in}} \pm B^{'} && \text{in } \Gamma_{\mathrm{in}} \times \mathbb{R}^2, \\ g|_{t=t_1} &= g^{\mathrm{eq}}_{\mathrm{out}} \pm B^{'} && \text{in } \Gamma_{\mathrm{out}} \times \mathbb{R}^2, \end{aligned}\right\} \text{Initial conditions} \tag{5.6}$$

$$\left.\begin{aligned} g\left(\boldsymbol{c}\right) &= g\left(-\boldsymbol{c}\right) && \text{in } I \times \Gamma_w \times \mathbb{R}^2{}_{\boldsymbol{n}.\boldsymbol{c}>0}, \\ g\left(\boldsymbol{c}\right) &= g^{\mathrm{eq}}_{\mathrm{in}} && \text{in } I \times \Gamma_{\mathrm{in}} \times \mathbb{R}^2, \\ g\left(\boldsymbol{c}\right) &= g^{\mathrm{eq}}_{\mathrm{out}} && \text{in } I \times \Gamma_{\mathrm{out}} \times \mathbb{R}^2, \end{aligned}\right\} \text{Boundary conditions} \tag{5.7}$$

where

$$\begin{cases} g^{\mathrm{eq}} = \displaystyle\int_{\mathbb{R}^2} g(\hat{\boldsymbol{c}}) \hat{f}^{\mathrm{eq}}(\hat{\boldsymbol{c}}) \frac{T + \left(\chi_\phi \boldsymbol{u} - \boldsymbol{c}\right) \cdot \left(\chi_\phi \boldsymbol{u} - \hat{\boldsymbol{c}}\right)}{\rho T} \, d\hat{\boldsymbol{c}}, \\ g^{\mathrm{eq}}_{\mathrm{in}} = \displaystyle\int_{\mathbb{R}^2} g(\hat{\boldsymbol{c}}) \frac{1}{\rho} f^{\mathrm{eq}}(\hat{\boldsymbol{c}}) \, d\hat{\boldsymbol{c}}, \\ g^{\mathrm{eq}}_{\mathrm{out}} = \displaystyle\int_{\mathbb{R}^2} g(\hat{\boldsymbol{c}}) f^{\mathrm{eq}}(\hat{\boldsymbol{c}}) \frac{\left(\chi_\phi \boldsymbol{u} - \boldsymbol{c}\right) \cdot \left(\chi_\phi \boldsymbol{u} - \hat{\boldsymbol{c}}\right)}{\rho_{out} T} \, d\hat{\boldsymbol{c}}, \end{cases} \tag{5.8}$$

$$A^{'} = \frac{1}{\rho}\left\{\frac{\partial A}{\partial \rho} \cdot \rho - \frac{\partial A}{\partial \left(\nabla \boldsymbol{u}\right)} \cdot \nabla \boldsymbol{u}\right\}, \tag{5.9}$$

$$B^{'} = \frac{1}{\rho}\left\{\frac{\partial B}{\partial \rho} \cdot \rho + \frac{\partial B}{\partial \boldsymbol{u}} \cdot (\boldsymbol{c} - \boldsymbol{u})\right\}. \tag{5.10}$$

Here, $g(\boldsymbol{x}, t, \boldsymbol{c})$ denotes the Lagrange's multiplier that is also called as the adjoint variable [101, 102]. $A^{'}$ and $B^{'}$ denote the integrands of real objective functionals A and B, respectively. It is noted that the adjoint equation above (5.5) is computed in the same manner as the primal equation (5.4) but in the backwards time. Especially, to solve this equation in the unsteady problem, the solutions of the primal problem in an entire computation history are needed [103, 99, 98, 32]. The hat notation denotes the extension of the Maxwell-equilibrium distribution [104] in fluid region $\boldsymbol{\Omega}$ to the fixed design domain

D entirely. The Maxwell-equilibrium distribution function (3.6) becomes the extended Maxwell-equilibrium distribution function as follows:

$$\hat{f}^{\mathrm{eq}} = \rho\left(\frac{1}{2\pi RT}\right)^{d/2} \exp\left(-\frac{|\boldsymbol{c} - \chi_\phi \boldsymbol{u}|^2}{2RT}\right). \tag{5.11}$$

As a result, the design sensitivity can be computed by using the solutions of the primal and the adjoint systems. The detail derivation of the design sensitivity is shown in the next section, the results is as follows:

$$\begin{aligned}
\delta_\phi \bar{J} &= \int_I \int_D \int_{\mathbb{R}^2} \frac{1}{\tau_B} \frac{\partial \hat{f}^{\mathrm{eq}}}{\partial \phi} g \delta\phi \; d\boldsymbol{c} d\Omega dt \\
&+ \int_I \int_{\Gamma_{\mathrm{in}} \cup \Gamma_{\mathrm{out}}} \int_{\mathbb{R}^2} \frac{\partial \hat{f}^{\mathrm{eq}}}{\partial \phi} g \delta\phi \; d\boldsymbol{c} d\Gamma dt + \lambda \int_D \delta\phi \; d\Omega \\
&= \int_{D \backslash (\Gamma_{\mathrm{in}} \cup \Gamma_{\mathrm{out}})} \left\{ \int_I \int_{\mathbb{R}^2} \frac{\left(\boldsymbol{c} - \chi_\phi \boldsymbol{u}\right) \cdot \boldsymbol{u}}{\tau_B RT} \hat{f}^{\mathrm{eq}} g \; d\boldsymbol{c} dt + \lambda \right\} \delta\phi \; d\Omega \\
&+ \int_{\Gamma_{\mathrm{in}} \cup \Gamma_{\mathrm{out}}} \left\{ \int_I \int_{\mathbb{R}^2} \frac{\left(\boldsymbol{c} - \chi_\phi \boldsymbol{u}\right) \cdot \boldsymbol{u}}{RT} \hat{f}^{\mathrm{eq}} g \; d\boldsymbol{c} dt + \lambda \right\} \delta\phi \; d\Gamma.
\end{aligned} \tag{5.12}$$

Next, by applying the same discretization system as Inamuro et al. [62] to a D2V9 lattice model, the primal equation (5.4), the adjoint equation (5.5), and the design sensitivity (5.12) can be expressed in the discretized forms with respect to the spacial position $\boldsymbol{x}$ and and time t. The corresponding discretized lattice Boltzmann equation, discretized adjoint lattice Boltzmann equation, and discretized design sensitivity can be derived as follows:

The discretized lattice Boltzmann equation:

$$f_i\left(\boldsymbol{x} + \boldsymbol{c}_i \Delta x, t + \Delta t\right) - f_i\left(\boldsymbol{x}, t\right) = -\frac{1}{\tau_B}\left[f_i\left(\boldsymbol{x}, t\right) - f_i^{\mathrm{eq}}\left(\boldsymbol{x}, t\right)\right], \tag{5.13}$$

The discretized adjoint lattice Boltzmann equation:

$$g_i\left(\boldsymbol{x} - \boldsymbol{c}_i \Delta x, t - \Delta t\right) - g_i\left(\boldsymbol{x}, t\right) = -\frac{1}{\tau_B}\left[g_i\left(\boldsymbol{x}, t\right) - g_i^{\mathrm{eq}}\left(\boldsymbol{x}, t\right)\right], \tag{5.14}$$

The discretized design sensitivity:

$$\begin{aligned}
\delta_\phi \bar{J} \;\; &= \;\; \left[\frac{1}{\tau_B} \sum_{i=1}^{9} 3 g_i \hat{f}_i^{eq} (\boldsymbol{c}_i - \chi_\phi \boldsymbol{u}) \cdot \boldsymbol{u} + \lambda\right] \quad \text{in } D \backslash (\Gamma_{\mathrm{in}} \cup \Gamma_{\mathrm{out}}) \\
&+ \;\; \left[\sum_{i=1}^{9} 3 g_i \hat{f}_i^{eq} (\boldsymbol{c}_i - \chi_\phi \boldsymbol{u}) \cdot \boldsymbol{u} + \lambda\right] \quad \text{on } \; \Gamma_{\mathrm{in}} \cup \Gamma_{\mathrm{out}}.
\end{aligned} \tag{5.15}$$

5.1.2 The adjoint problem and design sensitivity

By using the Lagrange's method, the topology optimization described in the above section (5.4) is replaced with a corresponding unconstrained problem as follows:

$$\min_{\phi} \bar{J} = J + G + I + B_{\mathrm{w}} + B_{\mathrm{in}} + B_{\mathrm{out}} + \lambda V \tag{5.16}$$

where $\bar{J}$ denotes the Lagrangian objective function, $\lambda \ni R$ denotes the Lagrange's multiplier, the functions G, I, B_{w}, B_{in}, and B_{out} are determined as follows:

$$G = \int_I \int_D \int_{\mathbb{R}^2} g \left\{ \frac{\partial f}{\partial t} + \boldsymbol{c} \cdot \nabla f + \frac{1}{\tau_B}(f - \hat{f}^{\mathrm{eq}}) \right\} d\boldsymbol{c} dD dt = 0 \tag{5.17}$$

$$I = \int_D \int_{\mathbb{R}^2} g(f|_{t=t_0} - f_0)\, d\boldsymbol{c} dD = 0 \tag{5.18}$$

$$B_{\mathrm{w}} = \int_I \int_{\Gamma_w} \int_{\mathbb{R}^2} g \left\{ f(\boldsymbol{c}) - f(-\boldsymbol{c}) \right\} d\boldsymbol{c} d\Gamma dt = 0 \tag{5.19}$$

$$B_{\mathrm{in}} = \int_I \int_{\Gamma_{\mathrm{in}}} \int_{\mathbb{R}^2} g \left\{ f - \hat{f}^{\mathrm{eq}}(\rho[f], \bar{\boldsymbol{u}}, \chi_\phi) \right\} d\boldsymbol{c} d\Gamma dt = 0 \tag{5.20}$$

$$B_{\mathrm{out}} = \int_I \int_{\Gamma_{\mathrm{out}}} \int_{\mathbb{R}^2} g \left\{ f - \hat{f}^{\mathrm{eq}}(\bar{\rho}, \boldsymbol{u}[f], \chi_\phi) \right\} d\boldsymbol{c} d\Gamma dt = 0 \tag{5.21}$$

First, employing the Karush-Kuhn-Tucker (KKT) conditions [105] to the optimization formula (5.16), it yields,

$$\begin{aligned} &\delta_\phi \bar{J} = 0\,,\ G = 0\,,\ I = 0\,,\ B_{\mathrm{w}} = 0\,,\ B_{\mathrm{in}} = 0\,,\ B_{\mathrm{out}} = 0\,, \\ &\lambda V = 0\,,\ \lambda \geq 0\,,\ V \leq 0, \end{aligned} \tag{5.22}$$

where $\delta_\phi \bar{J}$ denotes the variation of $\bar{J}$ with respect to the variation of ϕ.

Next, it is described how to solve the time-evolution equation (5.3) by introducing the gradient of $\bar{J}$ with respect to functions f, g, and ϕ. It is formulated as follows:

$$\delta \bar{J} = \delta_f J[f] + \delta_f F[f, g, \phi] + \delta_g F[f, g, \phi] + \delta_\phi F[f, g, \phi] + \lambda \delta_\phi V[\phi]. \tag{5.23}$$

Since the adjoint variable g is used, the variation of $\delta_g F[f, g, \phi]$ is eliminated. Here $F = G + I + B_{\mathrm{w}} + B_{\mathrm{in}} + B_{\mathrm{out}}$ denotes the equilibrium equation. From the Eq. (5.23), the so-called design sensitivity is, therefore, expressed as follows:

$$\delta \bar{J} = \delta_\phi F[f, g, \phi] + \lambda \delta_\phi V[\phi]. \tag{5.24}$$

Here the adjoint equation must be satisfied the following condition:

$$\delta_f J[f] + \delta_f F[f, g, \phi] = 0. \tag{5.25}$$

Next, the derivation of the adjoint equation for g from the Eq. (5.25) will be described. First, since $\delta_f J[f]$ is a variation of the objective functional J with respect to f, it is assumed that f is perturbed by an amount $\varepsilon\eta$ (where ε is a constant that represents a variation size and η is an arbitrary function). The perturbation of the objective functional with respect to the distribution function f is as follows:

$$\delta_f J = \lim_{\varepsilon \to 0} \frac{J[f + \varepsilon\eta] - J[f]}{\varepsilon}. \tag{5.26}$$

Since the objective functionals in this study are separately considered in the fluid region and on the structural boundary, the derivations are performed separately in the fluid region Ω and on the boundary Γ as follows:

$$\begin{cases} J_\Omega = -\int_I \int_\Omega A\left(\rho, \frac{\partial u_i}{\partial x_j}\right) \, d\Omega dt, \\ J_\Gamma = -\int_I \int_\Gamma B\left(\rho, \boldsymbol{u}\right) \, d\Gamma dt, \end{cases} \tag{5.27}$$

where J_Ω and J_Γ denote the objective functional considered in the internal domain Ω and on the structural boundary Γ, respectively.

Applying Taylor expression to expand the functionals A and B, and using the following equations:

$$\boldsymbol{u} = \frac{\boldsymbol{v}}{\rho}, \tag{5.28}$$

$$\boldsymbol{v}[f] = \int_{\mathbb{R}^2} \boldsymbol{c} f \, d\boldsymbol{c}, \tag{5.29}$$

$$\rho[\eta] = \int_{\mathbb{R}^2} \eta \, d\boldsymbol{c}, \tag{5.30}$$

$$\boldsymbol{v}[\eta] = \int_{\mathbb{R}^2} \boldsymbol{c}\eta \, d\boldsymbol{c}, \tag{5.31}$$

$$\begin{aligned} \frac{\partial u_i}{\partial x_j}\left(\rho[f] + \varepsilon\rho[\eta], \boldsymbol{v}[f] + \varepsilon\boldsymbol{v}[\eta]\right) &= \frac{\partial u_i}{\partial x_j}\left(\rho[f], \boldsymbol{v}[f]\right) \\ &+ \varepsilon\left\{\frac{\partial}{\partial \rho}\left(\frac{\partial u_i}{\partial x_j}\right)\rho[\eta] + \frac{\partial}{\partial \boldsymbol{v}}\left(\frac{\partial u_i}{\partial x_j}\right)\boldsymbol{v}[\eta]\right\} + O(\varepsilon), \end{aligned} \tag{5.32}$$

$$\begin{aligned} \boldsymbol{u}\left(\rho[f] + \varepsilon\rho[\eta], \boldsymbol{v}[f] + \varepsilon\boldsymbol{v}[\eta]\right) &= \boldsymbol{u}\left(\rho[f], \boldsymbol{v}[f]\right) \\ &+ \varepsilon\left\{\frac{\partial \boldsymbol{u}}{\partial \rho}\rho[\eta] + \frac{\partial \boldsymbol{u}}{\partial \boldsymbol{v}}\boldsymbol{v}[\eta]\right\} + O(\varepsilon), \end{aligned} \tag{5.33}$$

$$A\left(\rho[f + \varepsilon\eta], \frac{\partial u_i}{\partial x_j}[f + \varepsilon\eta]\right) = A\left(\rho[f] + \varepsilon\rho[\eta], \frac{\partial u_i}{\partial x_j}\left(\rho[f] + \varepsilon\rho[\eta], \boldsymbol{v}[f] + \varepsilon\boldsymbol{v}[\eta]\right)\right), \tag{5.34}$$

$$B\left(\rho[f + \varepsilon\eta], \boldsymbol{u}[f + \varepsilon\eta]\right) = B\left(\rho[f] + \varepsilon\rho[\eta], \boldsymbol{u}\left(\rho[f] + \varepsilon\rho[\eta], \boldsymbol{v}[f] + \varepsilon\boldsymbol{v}[\eta]\right)\right). \tag{5.35}$$

Thus, the following expressions can be obtained:

$$
\begin{aligned}
A = {} & A\left\{\rho\left[f\right], \frac{\partial u_i}{\partial x_j}\left(\rho\left[f\right], \boldsymbol{v}\left[f\right]\right)\right\} \\
& + \varepsilon\left\{\frac{\partial A}{\partial \rho}\rho\left[\eta\right] + \frac{\partial A}{\partial\left(\frac{\partial u_i}{\partial x_j}\right)} \cdot \left\{\frac{\partial}{\partial \rho}\left(\frac{\partial u_i}{\partial x_j}\right)\rho\left[\eta\right] + \frac{\partial}{\partial \boldsymbol{v}}\left(\frac{\partial u_i}{\partial x_j}\right)\boldsymbol{v}\left[\eta\right]\right\}\right\}.
\end{aligned}
\tag{5.36}
$$

$$
B = B\left\{\rho\left[f\right], \boldsymbol{u}\left(\rho\left[f\right], \boldsymbol{v}\left[f\right]\right)\right\} + \varepsilon\left\{\frac{\partial B}{\partial \rho}\rho\left[\eta\right] + \frac{\partial B}{\partial \boldsymbol{u}} \cdot \left\{\frac{\partial \boldsymbol{u}}{\partial \rho}\rho\left[\eta\right] + \frac{\partial \boldsymbol{u}}{\partial \boldsymbol{v}}\boldsymbol{v}\left[\eta\right]\right\}\right\}. \tag{5.37}
$$

Therefore, the integrands $A^{'}$ and $B^{'}$ can be obtained by the following derivations:

$$
\begin{aligned}
\delta_f J_\Omega &= \lim_{\varepsilon\to 0}\frac{J_\Omega\left[f+\varepsilon\eta\right] - J_\Omega\left[f\right]}{\varepsilon} \\
&= -\int_I\int_\Omega\left[\frac{\partial A}{\partial \rho}\rho\left[\eta\right] + \frac{\partial A}{\partial\left(\frac{\partial u_i}{\partial x_j}\right)} \cdot \left\{\frac{\partial}{\partial \rho}\left(\frac{\partial u_i}{\partial x_j}\right)\rho\left[\eta\right] + \frac{\partial}{\partial \boldsymbol{v}}\left(\frac{\partial u_i}{\partial x_j}\right)\boldsymbol{v}\left[\eta\right]\right\}\right] dtd\Omega \\
&= -\int_I\int_\Omega\left[\frac{\partial A}{\partial \rho}\rho\left[\eta\right] + \frac{\partial A}{\partial\left(\frac{\partial u_i}{\partial x_j}\right)} \cdot \left\{-\frac{1}{\rho_{[f]}^2}\left(\frac{\partial \boldsymbol{v}_i\left[f\right]}{\partial x_j}\right)\rho\left[\eta\right] + \frac{\partial}{\partial x_j}\left(\frac{1}{\rho_{[f]}}\right)\boldsymbol{v}\left[\eta\right]\right\}\right] dtd\Omega \\
&= -\int_I\int_\Omega\frac{1}{\rho_{[f]}}\left\{\frac{\partial A}{\partial \rho}\rho\left[f\right] + \frac{\partial A}{\partial\left(\frac{\partial u_i}{\partial x_j}\right)}\left(-\left(\frac{\partial u_i}{\partial x_j}\right) + 0\right)\right\}\rho\left[\eta\right]\ dtd\Omega \\
&= -\int_{\mathbb{R}^2}\int_I\int_\Omega\frac{1}{\rho_{[f]}}\left\{\frac{\partial A}{\partial \rho}\rho\left[f\right] - \frac{\partial A}{\partial\left(\frac{\partial u_i}{\partial x_j}\right)}\left(\frac{\partial u_i}{\partial x_j}\right)\right\}\eta\ d\boldsymbol{c}dtd\Omega.
\end{aligned}
\tag{5.38}
$$

$$
\begin{aligned}
\delta_f J_\Gamma &= \lim_{\varepsilon\to 0}\frac{J_\Gamma\left[f+\varepsilon\eta\right] - J_\Gamma\left[f\right]}{\varepsilon} \\
&= -\int_I\int_\Gamma\left[\frac{\partial B}{\partial \rho}\rho\left[\eta\right] + \frac{\partial B}{\partial \boldsymbol{u}} \cdot \left\{\frac{\partial \boldsymbol{u}}{\partial \rho}\rho\left[\eta\right] + \frac{\partial \boldsymbol{u}}{\partial \boldsymbol{v}}\boldsymbol{v}\left[\eta\right]\right\}\right] dtd\Gamma \\
&= -\int_I\int_\Gamma\left[\frac{\partial B}{\partial \rho}\rho\left[\eta\right] + \frac{1}{\rho_{[f]}}\frac{\partial B}{\partial \boldsymbol{u}} \cdot \left\{-\frac{\boldsymbol{v}\left[f\right]}{\rho\left[f\right]}\rho\left[\eta\right] + \boldsymbol{v}\left[\eta\right]\right\}\right] dtd\Gamma \\
&= -\int_I\int_\Gamma\left[\frac{\partial B}{\partial \rho}\rho\left[\eta\right] + \frac{1}{\rho_{[f]}}\frac{\partial B}{\partial \boldsymbol{u}} \cdot \left\{-\boldsymbol{u}\left[f\right]\rho\left[\eta\right] + \boldsymbol{v}\left[\eta\right]\right\}\right] dtd\Gamma \\
&= -\int_{\mathbb{R}^2}\int_I\int_\Gamma\frac{1}{\rho_{[f]}}\left\{\frac{\partial B}{\partial \rho}\rho\left[f\right] + \frac{\partial B}{\partial \boldsymbol{u}} \cdot \left\{\frac{\boldsymbol{v}\left[\eta\right]}{\rho\left[\eta\right]} - \boldsymbol{u}\left[f\right]\right\}\right\}\rho\left[\eta\right]\ dtd\Gamma \\
&= -\int_{\mathbb{R}^2}\int_I\int_\Gamma\frac{1}{\rho_{[f]}}\left\{\frac{\partial B}{\partial \rho}\rho\left[f\right] + \frac{\partial B}{\partial \boldsymbol{u}} \cdot \left\{\boldsymbol{c} - \boldsymbol{u}\left[f\right]\right\}\right\}\eta\ d\boldsymbol{c}dtd\Gamma.
\end{aligned}
\tag{5.39}
$$

Finally, the integrands $A^{'}$ and $B^{'}$ are expressed as follows:

$$
A^{'} = -\frac{1}{\rho}\left\{\frac{\partial A}{\partial \rho}\rho - \frac{\partial A}{\partial\left(\frac{\partial u_i}{\partial x_j}\right)}\left(\frac{\partial u_i}{\partial x_j}\right)\right\}, \tag{5.40}
$$

$$B' = -\frac{1}{\rho}\left\{\frac{\partial B}{\partial \rho}\rho + \frac{\partial B}{\partial \boldsymbol{u}}(\boldsymbol{c}-\boldsymbol{u})\right\}. \tag{5.41}$$

Second, the perturbation of the residual F with respect to the distribution function f is formulated as follows:

$$\delta_f F \;=\; \lim_{\varepsilon\to 0}\frac{F[f+\varepsilon\eta]-F[f]}{\varepsilon}. \tag{5.42}$$

Here,

$$\begin{aligned}
F[f+\varepsilon\eta] =& G[f+\varepsilon\eta] + I[f+\varepsilon\eta] + B_{\mathrm{w}}[f+\varepsilon\eta] + B_{\mathrm{in}}[f+\varepsilon\eta] + B_{\mathrm{out}}[f+\varepsilon\eta] \\
=& \int_I\int_D\int_{\mathbb{R}^2} g\left(\frac{\partial(f+\varepsilon\eta)}{\partial t} + \boldsymbol{c}\cdot\nabla(f+\varepsilon\eta) + \frac{1}{\tau_B}\left[(f+\varepsilon\eta)\right.\right. \\
&\qquad\qquad \left. - \hat{f}^{eq}\left(\rho[f+\varepsilon\eta], \boldsymbol{u}\left(\rho[f+\varepsilon\eta], \boldsymbol{v}[f+\varepsilon\eta]\right)\right)\right. d\boldsymbol{c}dDdt \\
&+ \int_D\int_{\mathbb{R}^2} g(f+\varepsilon\eta-f_0)\; d\boldsymbol{c}dD \\
&+ \int_I\int_{\Gamma_{\mathrm{w}}}\int_{\mathbb{R}^2} g\left\{f(\boldsymbol{c})+\varepsilon\eta(\boldsymbol{c}) - f(-\boldsymbol{c}) - \varepsilon\eta(-\boldsymbol{c})\right\}\; d\boldsymbol{c}d\Gamma dt \\
&+ \int_I\int_{\Gamma_{\mathrm{in}}}\int_{\mathbb{R}^2} g\left\{f+\varepsilon\eta - \hat{f}^{eq}(\rho[f+\varepsilon\eta], \bar{u})\right\}\; d\boldsymbol{c}d\Gamma dt \\
&+ \int_I\int_{\Gamma_{\mathrm{out}}}\int_{\mathbb{R}^2} g\left\{f+\varepsilon\eta - \hat{f}^{eq}(\bar{\rho}, \boldsymbol{u}[f+\varepsilon\eta])\right\}\; d\boldsymbol{c}d\Gamma dt.
\end{aligned} \tag{5.43}$$

Therefore, the Eq. (5.42) can be expressed as follows:

$$\begin{aligned}
\delta_f F =& \lim_{\varepsilon\to 0}\frac{F[f+\varepsilon\eta]-F[f]}{\varepsilon} \\
=& -\int_I\int_D\int_{\mathbb{R}^2}\frac{\partial g}{\partial t}\eta\; d\boldsymbol{c}dDdt + \left[\int_D\int_{\mathbb{R}^2} g\eta\; d\boldsymbol{c}dD\right]_{t_0}^{t_1} \\
&+ \int_I\int_{\Gamma}\int_{\mathbb{R}^2} g\eta\boldsymbol{c}\cdot\boldsymbol{n}\; d\boldsymbol{c}d\Gamma dt - \int_I\int_D\int_{\mathbb{R}^2}(\boldsymbol{c}\cdot\nabla g)\eta\; d\boldsymbol{c}dDdt \\
&+ \int_I\int_D\int_{\mathbb{R}^2}\frac{g}{\tau_B}\eta\; d\boldsymbol{c}dDdt - \int_I\int_D\int_{\mathbb{R}^2}\frac{\hat{g}^{\mathrm{eq}}}{\tau_B}\eta\; d\boldsymbol{c}dDdt \\
&+ \int_D\int_{\mathbb{R}^2} g\eta\; d\boldsymbol{c}dD \\
&+ \int_I\int_{\Gamma_{\mathrm{w}}}\int_{\mathbb{R}^2} g\left\{\eta(\boldsymbol{c}) - \eta(-\boldsymbol{c})\right\}\; d\boldsymbol{c}d\Gamma dt \\
&+ \int_I\int_{\Gamma_{\mathrm{in}}}\int_{\mathbb{R}^2}\left\{g - \hat{g}^{\mathrm{eq}}_{\mathrm{in}}\right\}\eta\; d\boldsymbol{c}d\Gamma dt \\
&+ \int_I\int_{\Gamma_{\mathrm{out}}}\int_{\mathbb{R}^2}\left(g - \hat{g}^{\mathrm{eq}}_{\mathrm{out}}\right)\eta\; d\boldsymbol{c}d\Gamma dt,
\end{aligned} \tag{5.44}$$

where the expression of the perturbed quantities of $G = G_1 + G_2 + G_3 + G_4$, I, B_{w}, B_{in}, and B_{out} are sufficiently given in the Appendices section (A). Finally, from Eqs. (5.25), (5.38), (5.39), and Eq. (5.44), the adjoint equations (5.5)-(5.7) are constructed.

Next, the design sensitivity is calculated. From the previous calculation, the design sensitivity $\delta_\phi \bar{J}$ is as follows.

$$\delta_\phi \bar{J} = \delta_\phi F[f, g, \phi] + \lambda \delta_\phi V[\phi] \tag{5.45}$$

First, $\delta_\phi \bar{J}$ is a variation of the objective functional $\bar{J}$ with respect to ϕ, it is assumed that ϕ is perturbed by an amount $\varepsilon\psi$ (where ε is a constant that represents a variation size and ψ is an arbitrary function). It is noted that the perturbation of the objective functional by the change of ϕ is affected only by the equilibrium distribution function f^{eq}. Thus, only the fourth term of G (in Eq. (5.18) exists the equilibrium distribution function f^{eq}), B_{in}, and B_{out} are involved for the analysis. Here,

$$\begin{aligned} F[\phi + \varepsilon\psi] =& G[\phi + \varepsilon\psi] + B_{\mathrm{in}}[\phi + \varepsilon\psi] + B_{\mathrm{out}}[\phi + \varepsilon\psi] \\ =& \int_I \int_D \int_{\mathbb{R}^2} \frac{g}{\tau_B} \left\{ f - \hat{f}^{\mathrm{eq}}(\chi_\phi[\phi + \varepsilon\psi]) \right\} \, d\boldsymbol{c} dD dt \\ &+ \int_I \int_{\Gamma_{\mathrm{in}}} \int_{\mathbb{R}^2} g \left\{ f - \hat{f}^{\mathrm{eq}}[\chi_\phi(\phi + \varepsilon\psi)] \right\} \, d\boldsymbol{c} d\Gamma dt \\ &+ \int_I \int_{\Gamma_{\mathrm{out}}} \int_{\mathbb{R}^2} g \left\{ f - \hat{f}^{\mathrm{eq}}[\chi_\phi(\phi + \varepsilon\psi)] \right\} \, d\boldsymbol{c} d\Gamma dt \end{aligned} \tag{5.46}$$

where,

$$\begin{aligned} G[\phi + \varepsilon\psi] =& \int_I \int_D \int_{\mathbb{R}^2} \frac{g}{\tau_B} \left\{ f - \hat{f}^{\mathrm{eq}}(\chi_\phi[\phi + \varepsilon\psi]) \right\} \, d\boldsymbol{c} dD dt \\ =& \int_I \int_D \int_{\mathbb{R}^2} \frac{g}{\tau_B} \left\{ f - \hat{f}^{\mathrm{eq}}[\phi] \right\} \, d\boldsymbol{c} dD dt \\ &- \varepsilon \int_I \int_D \int_{\mathbb{R}^2} \frac{g}{\tau_B} \frac{\partial \hat{f}^{\mathrm{eq}}}{\partial \chi_\phi} \chi_\phi[\psi] \, d\boldsymbol{c} dD dt, \end{aligned} \tag{5.47}$$

$$\begin{aligned} B_{\mathrm{in}}[\chi_\phi(\phi + \varepsilon\psi)] =& \int_I \int_{\Gamma_{\mathrm{in}}} \int_{\mathbb{R}^2} g \left\{ f - \hat{f}^{\mathrm{eq}}[\chi_\phi(\phi + \varepsilon\psi)] \right\} \, d\boldsymbol{c} d\Gamma dt \\ =& \int_I \int_{\Gamma_{\mathrm{in}}} \int_{\mathbb{R}^2} g \left\{ f - \hat{f}^{\mathrm{eq}}[\chi_\phi(\phi)] \right\} \, d\boldsymbol{c} d\Gamma dt \\ &- \varepsilon \int_I \int_{\Gamma_{\mathrm{in}}} \int_{\mathbb{R}^2} g \frac{\partial \hat{f}^{\mathrm{eq}}}{\partial \chi_\phi} \chi_\phi[\psi] \, d\boldsymbol{c} d\Gamma dt, \end{aligned} \tag{5.48}$$

$$\begin{aligned} B_{\mathrm{out}}[\chi_\phi(\phi + \varepsilon\psi)] =& \int_I \int_{\Gamma_{\mathrm{out}}} \int_{\mathbb{R}^2} g \left\{ f - \hat{f}^{\mathrm{eq}}[\chi_\phi(\phi + \varepsilon\psi)] \right\} \, d\boldsymbol{c} d\Gamma dt \\ =& \int_I \int_{\Gamma_{\mathrm{out}}} \int_{\mathbb{R}^2} g \left\{ f - \hat{f}^{\mathrm{eq}}[\chi_\phi(\phi)] \right\} \, d\boldsymbol{c} d\Gamma dt \\ &- \varepsilon \int_I \int_{\Gamma_{\mathrm{out}}} \int_{\mathbb{R}^2} g \frac{\partial \hat{f}^{\mathrm{eq}}}{\partial \chi_\phi} \chi_\phi[\psi] \, d\boldsymbol{c} d\Gamma dt. \end{aligned} \tag{5.49}$$

Therefore, the second term in Eq. (5.45) can be expressed as follows:

$$
\begin{aligned}
\delta_\phi F &= \lim_{\varepsilon\to 0} \frac{F[\phi+\varepsilon\psi]-F[\phi]}{\varepsilon} \\
&= -\int_I\int_D\int_{\mathbb{R}^2} \frac{g}{\tau_B}\frac{\partial \hat{f}^{\mathrm{eq}}}{\partial \chi_\phi}\chi_\phi[\psi]\ d\boldsymbol{c}dDdt \\
&\quad -\int_I\int_{\Gamma_{\mathrm{in}}}\int_{\mathbb{R}^2} g\frac{\partial \hat{f}^{\mathrm{eq}}}{\partial \chi_\phi}\chi_\phi[\psi]\ d\boldsymbol{c}d\Gamma dt \\
&\quad -\int_I\int_{\Gamma_{\mathrm{out}}}\int_{\mathbb{R}^2} g\frac{\partial \hat{f}^{\mathrm{eq}}}{\partial \chi_\phi}\chi_\phi[\psi]\ d\boldsymbol{c}d\Gamma dt \\
&= -\int_I\int_D\int_{\mathbb{R}^2} \frac{g}{\tau_B}\frac{\hat{f}^{\mathrm{eq}}}{RT}\boldsymbol{u}\cdot(\boldsymbol{c}-\chi_\phi\boldsymbol{u})\chi_\phi[\psi]\ d\boldsymbol{c}dDdt \\
&\quad -\int_I\int_{\Gamma_{\mathrm{in}}}\int_{\mathbb{R}^2} g\frac{\hat{f}^{\mathrm{eq}}}{RT}\boldsymbol{u}\cdot(\boldsymbol{c}-\chi_\phi\boldsymbol{u})\chi_\phi[\psi]\ d\boldsymbol{c}d\Gamma dt \\
&\quad -\int_I\int_{\Gamma_{\mathrm{out}}}\int_{\mathbb{R}^2} g\frac{\hat{f}^{\mathrm{eq}}}{RT}\boldsymbol{u}\cdot(\boldsymbol{c}-\chi_\phi\boldsymbol{u})\chi_\phi[\psi]\ d\boldsymbol{c}d\Gamma dt.
\end{aligned}
\tag{5.50}
$$

Second, the perturbation of the volume constraint V with respect to the level-set function ϕ is formulated as follows:

$$
\begin{aligned}
V[\chi_\phi(\phi+\varepsilon\psi)] &= \int_D \chi_\phi[\phi+\varepsilon\psi]\ dD - V_{\max} \\
&= \int_D \chi_\phi[\phi]\ dD + \varepsilon\int_D \chi_\phi[\psi]\ dD - V_{\max}.
\end{aligned}
\tag{5.51}
$$

Thus,

$$
\begin{aligned}
\delta_\phi V &= \lim_{\varepsilon\to 0}\frac{V[\phi+\varepsilon\psi]-V[\phi]}{\varepsilon} \\
&= \int_D \chi_\phi[\psi]\ dD.
\end{aligned}
\tag{5.52}
$$

Finally, from Eq. (5.50) and Eq. (5.52), the design sensitivity constructed as follows:

$$
\begin{aligned}
\delta_\phi \bar{J} =& \delta_\phi F + \lambda\delta_\phi V \\
=& -\int_I\int_D\int_{\mathbb{R}^2} \frac{g}{\tau_B}\frac{\hat{f}^{\mathrm{eq}}}{RT}\boldsymbol{u}\cdot(\boldsymbol{c}-\chi_\phi\boldsymbol{u})\chi_\phi[\psi]\ d\boldsymbol{c}dDdt \\
&-\int_I\int_{\Gamma_{\mathrm{in}}}\int_{\mathbb{R}^2} g\frac{\hat{f}^{\mathrm{eq}}}{RT}\boldsymbol{u}\cdot(\boldsymbol{c}-\chi_\phi\boldsymbol{u})\chi_\phi[\psi]\ d\boldsymbol{c}d\Gamma dt \\
&-\int_I\int_{\Gamma_{\mathrm{out}}}\int_{\mathbb{R}^2} g\frac{\hat{f}^{\mathrm{eq}}}{RT}\boldsymbol{u}\cdot(\boldsymbol{c}-\chi_\phi\boldsymbol{u})\chi_\phi[\psi]\ d\boldsymbol{c}d\Gamma dt + \lambda\int_D \chi_\phi[\psi]\ dD \\
=& \int_{D\setminus(\Gamma_{\mathrm{in}}\cup\Gamma_{\mathrm{out}})}\left\{-\int_I\int_{\mathbb{R}^2}\frac{g}{\tau_B}\frac{\hat{f}^{\mathrm{eq}}}{RT}\boldsymbol{u}\cdot(\boldsymbol{c}-\chi_\phi\boldsymbol{u})\ d\boldsymbol{c}dt+\lambda\right\}\chi_\phi[\psi]\ dD \\
&\int_{\Gamma_{\mathrm{in}}\cup\Gamma_{\mathrm{out}}}\left\{-\int_I\int_{\mathbb{R}^2} g\frac{\hat{f}^{\mathrm{eq}}}{RT}\boldsymbol{u}\cdot(\boldsymbol{c}-\chi_\phi\boldsymbol{u})\ d\boldsymbol{c}dt+\lambda\right\}\chi_\phi[\psi]\ d\Gamma.
\end{aligned}
\tag{5.53}
$$

5.2 Numerical verification

In this section, several numerical demonstrations will be carried out to validate the proposed theoretical analysis. The wide-range applicabilities of the proposed method in engineering design are shown in various numerical applications in various objective functional examples, in both the minimization and maximization problems, in the steady and transient problems, and in the single direction flow and multiple direction flow problems, respectively.

In all numerical examples in this section, the initial conditions are initially filled by fluid at equilibrium state. The flow field is characterized by the Reynolds number, which is set as follows:

$$\mathrm{Re} = \frac{LU_o}{\nu}, \tag{5.54}$$

where L denotes the characteristics length of the inlet width. $U_o = 1 \times 10^{-1}$ denotes the mean velocity, $\tau_B = 0.8$ denotes the relaxation time, and $\nu = 1 \times 10^{-1}$ denotes the viscosity. The initial design domain is a square of $50\Delta x \times 50\Delta x$. The reference time t_1 for the LBM is preferred such that $N = 3600$ time steps in both the steady and unsteady problems. The regularization coefficient is set as $\tau = 5 \times 10^{-4}$ for all cases. It is, however, the constant boundary conditions are simply imposed in the steady problem while using the same framework of the transient problem in a direct comparison between the steady and unsteady problems in the study. The fluid volume constraint is set as 50% of its initial fluid volume. The terminated criterion is met the following conditions:

$$\left| \frac{J_k - J_{k-1}}{J_k} \right| < \epsilon_{\mathrm{opti}}, \tag{5.55}$$

where J_k denotes the objective functional at the k optimization time step, and $\epsilon_{\mathrm{opti}} = 1 \times 10^{-4}$ is set through all numerical examples.

The two objective functionals used in this section wherein it is defined in the fluid domain Ω or defined on the structural boundary Γ are as follows:

- The *dissipated kinetic energy* that relates to the above functional A is expressed as,

$$J_\Omega|_{t=t_1} = \frac{1}{\mathrm{Re}} \int_I \int_\Omega \frac{\partial u_i}{\partial x_j} \left(\frac{\partial u_i}{\partial x_j} + \frac{\partial u_j}{\partial x_i} \right) dt d\Omega \qquad (i, j = 1, 2). \tag{5.56}$$

- The *pressure drop* that relates to the above functional B is expressed as,

$$J_\Gamma|_{t=t_1} = \int_I \int_{\Gamma_{\mathrm{in}} \cup \Gamma_{\mathrm{out}}} u_j \left(\frac{1}{2} u_i^2 + p \right) n_j \; dt d\Gamma \qquad (i, j = 1, 2). \tag{5.57}$$

It is noted that the indexes i and j are followed Einstein's rule.

The two pairs of inlet-outlet boundary conditions for the case of steady and transient flows are respectively given as follows:

- For the *steady problem*, a constant inflow-outflow boundary conditions are used as,

$$\begin{cases} U_{in} = U_o \dfrac{(y-b)(a-y)}{1/4(a+b)^2 - ab} & \text{on } \Gamma_{\text{in}}, \\ \rho_{out} = 1 & \text{on } \Gamma_{\text{out}}. \end{cases} \tag{5.58}$$

- For the *transient problem*, a periodic inflow-outflow boundary conditions are used as,

$$\begin{cases} U_{in} = U_o \dfrac{(y-b)(a-y)}{1/4(a+b)^2 - ab}(1-\cos(\omega t)) & \text{on } \Gamma_{\text{in}}, \\ \rho_{out} = 1 & \text{on } \Gamma_{\text{out}}, \end{cases} \quad (t \in [0, 2\pi]). \tag{5.59}$$

Here, the effects of ω in the performance of transient cases will be investigated in the unsteady flow problem and will be sufficiently specified. Other than that, the $\omega = 1$ is used for all cases of the transient flow in the study. The parameters a and b used to defined the inlet width are different in one another case. Therefore, they are given in different numerical examples.

It is noted that to conduct a maximization problem from a minimization problem, the objective functional of the minimization problem is inversed by adding a minus sign. As a consequence, the differences are summarized as follows:

- For the *minimization problem*, the objective functionals are defined as,

$$\begin{cases} J_\Omega = \displaystyle\int_I \int_\Omega A\left(\rho, \nabla \boldsymbol{u}\right) \; d\Omega dt, \\ J_\Gamma = \displaystyle\int_I \int_\Gamma B\left(\rho, \boldsymbol{u}\right) \; d\Gamma dt. \end{cases} \tag{5.60}$$

The corresponding initial conditions of the adjoint Boltzmann equation (5.6) becomes,

$$\begin{cases} g|_{t=t_1} = -A' & \text{in } D \times \mathbb{R}^2, \\ g|_{t=t_1} = g_{\text{in}}^{\text{eq}} + B' & \text{on } \Gamma_{\text{in}} \times \mathbb{R}^2, \\ g|_{t=t_1} = g_{\text{out}}^{\text{eq}} + B' & \text{on } \Gamma_{\text{out}} \times \mathbb{R}^2. \end{cases} \tag{5.61}$$

- For the *maximization problem*, the objective functionals are defined as,

$$\begin{cases} J_\Omega = -\displaystyle\int_I \int_\Omega A\left(\rho, \nabla \boldsymbol{u}\right) \; d\Omega dt, \\ J_\Gamma = -\displaystyle\int_I \int_\Gamma B\left(\rho, \boldsymbol{u}\right) \; d\Gamma dt. \end{cases} \tag{5.62}$$

The corresponding initial conditions of the adjoint Boltzmann equation (5.6) becomes,

$$\begin{cases} g|_{t=t_1} = +A' & \text{in } D \times \mathbb{R}^2, \\ g|_{t=t_1} = g_{\text{in}}^{\text{eq}} - B' & \text{on } \Gamma_{\text{in}} \times \mathbb{R}^2, \\ g|_{t=t_1} = g_{\text{out}}^{\text{eq}} - B' & \text{on } \Gamma_{\text{out}} \times \mathbb{R}^2. \end{cases} \tag{5.63}$$

It is noted that the different values with the above settings will be described in case the other values are particularly used in specific numerical examples.

5.2.1 Verification of design sensitivity

Inspiring by the previous study by Yaji et al. [23], the design sensitivity in Eq. (5.12) is numerically compared with the finite differences of the given objective functional (denoted by FD_J). In this verification, the objective functional corresponds to the dissipation energy (5.56) is selected. The central difference method is used to compare finite differences. It is written as follows:

$$FD_J = \frac{J_\Omega(\chi_\phi + \gamma) - J_\Omega(\chi_\phi - \gamma)}{2\gamma}, \tag{5.64}$$

where $\gamma > 0$ denotes a small perturbation size of χ_ϕ, it is defined as $\gamma = 1 \times 10^{-3}$ in this study.

Table 5.1: The specified parameters used in the verification of design sensitivity problem

Mesh size $[\Delta x]$	Re	Inlet width L $[\Delta x]$	Mean velocity U_o	Viscosity ν	Relaxation time τ_B
50×50	32	16 ($a = 34, b = 18$)	1×10^{-1}	1×10^{-1}	0.8

Table 5.1 shows the summary of these specified parameters used in the verification of design sensitivity. Fig. 5.1 shows the design setting for this numerial example. The initial design is a square of $50\Delta x \times 50\Delta x$ latice and filled by fluid at equiribrium state. The inlet width and outlet width are the same ($16\Delta x$ lattice size) and placed in two opposite sides in the vertical left-end and the vertical right-end, respectively. In the center of the design domain, a solid circular with $20\Delta x$ lattice size is placed. The parameters $a = 34$ and $b = 18$ are respectively designated. The periodic inflow-outflow boundary conditions (5.59) are

selected. With these setting, the Reynolds number Re = 32 is accordingly computed by the Eq. (5.54). For the minimization of this verification problem, the objective functional (5.60) and the initial conditions of the adjoint system (5.61) are used while the objective functional (5.62) and the initial conditions of the adjoint system (5.63) are used in the maximization problem, respectively.

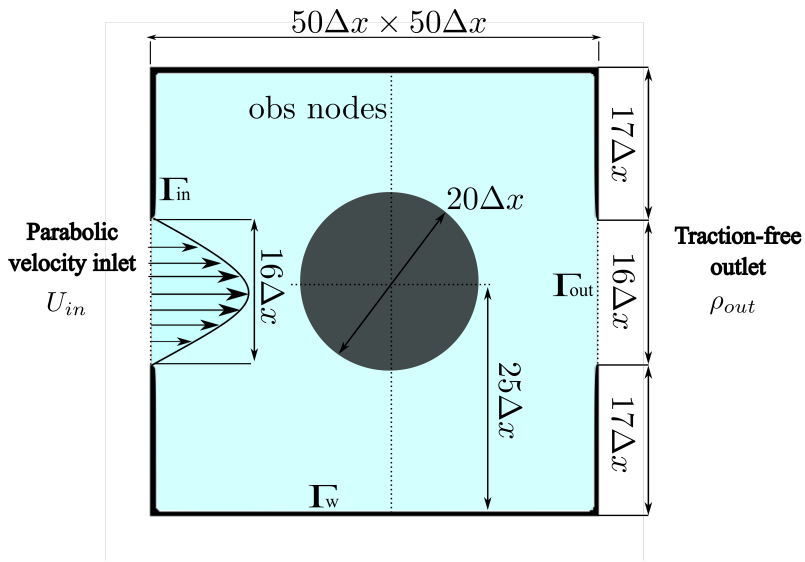

Figure 5.1: Design seting of design sensitivity validation problem.

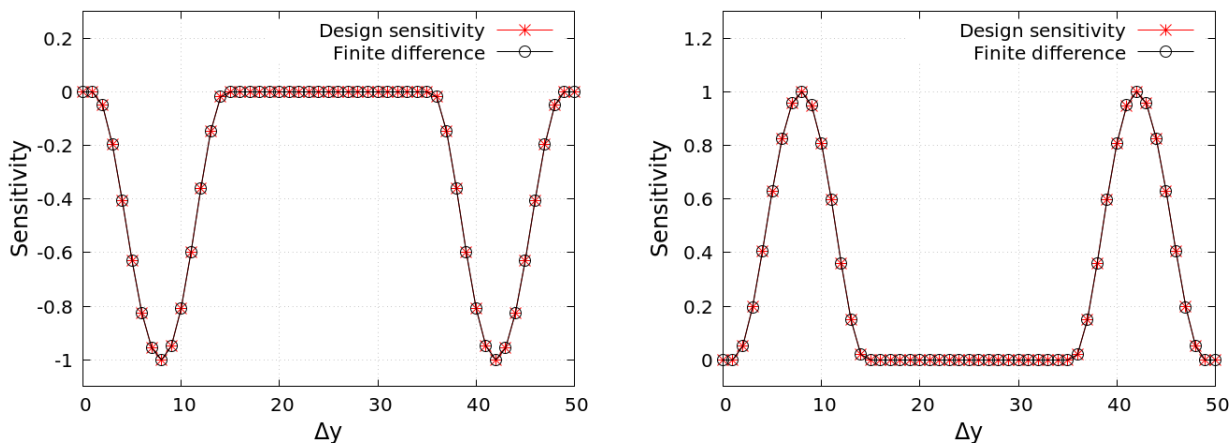

(a) Minimization problem

(b) Maximization problem

Figure 5.2: The result of design sensitivity and finite difference for both the minimization and maximization problems in comparison.

By the above settings, the recorded values for the design sensitivity and the comparative finite differences of the observation points (placed along the vertical centerline in the

design domain) are plotted. It is shown in Fig. 5.2, the good agreements between the finite difference and the design sensitivity in both the minimization and maximization are obtained. This confirms the verification for the design sensitivity in this study. It is noted that, in the maximization problem, the objective functional in the minimization problem is replaced with a minus sign results to an up-side-down configuration as compared to that of the minimization problem (see Figs. 5.2a and 5.2b).

Figure 5.3 shows the relationship of the primal field and the adjoint field wherein

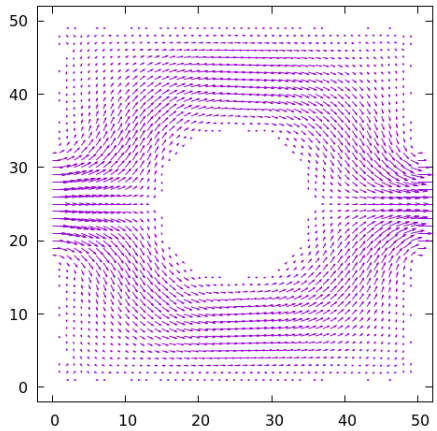

(a) Velocity vector field

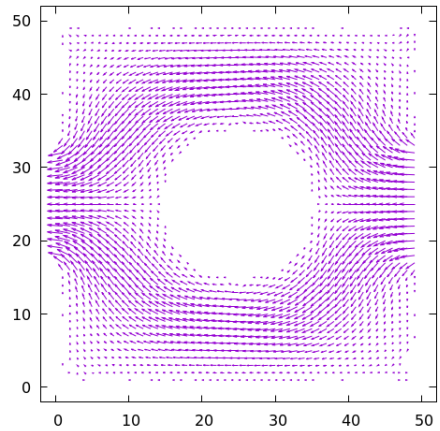

(b) Adjoint velocity vector field

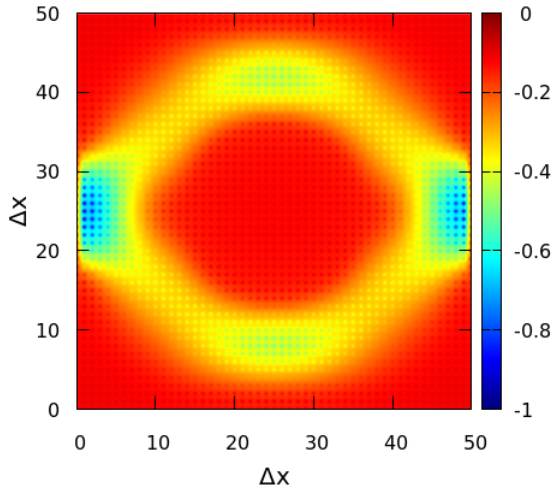

(c) Sensitivity distribution

Figure 5.3: Demonstrations of velocity vector field, adjoint velocity vector field, and the distribution of the design sensitivity for the minimization problem.

the opposite directions of the velocity vector field the adjoint vector field are observed (see Figs. 5.3a and 5.3b). It is well agreed with the theoretical formulation. To be more specific, the adjoint lattice Boltzmann equation (5.14) has the same structure but is discretized backward in time and space as compared to the lattice Boltzmann equation (5.13) [106, 98, 32]. The design sensitivity distribution shows that the objective functional tends to be reduced where the shortest connection between inlet and outlet (see Fig. 5.3c). It is the best to remove any obstacle placed at the inlet and outlet boundaries, as the lowest values of sensitivities are near the the inlet and outlet are obtained.

5.2.2 Various objective functional problems

In this section, the effects of using different objective functionals in the topology optimization of the same fluid flow will be investigated. The differences of the optimal configurations obtained from the uses of different objective functionals evaluated either in the interior-domain or on the boundary-domain will be examined. The important contributions of each kind of objective functionals used in the topology optimization for the flow field are, therefore, clarified throughout numerical demonstrations in the section.

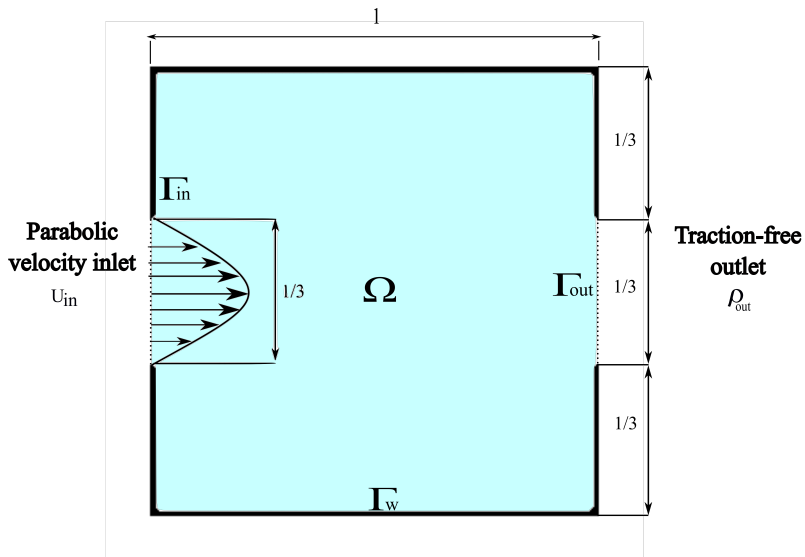

Figure 5.4: Design seting of the straight chanel.

Next, to determine the two objective functionals correspond to the dissipated kinetic energy and the pressure drop used in this study, the following derivations are given in summary to declare them. Here, the time-variant kinetic energy of the incompressible

Navier-Stokes flows reads [107]:

$$\frac{\partial E}{\partial t} = \rho \int \boldsymbol{u} \cdot \frac{\partial \boldsymbol{u}}{\partial t} \, dV. \tag{5.65}$$

The divergence-free ($\nabla \cdot \boldsymbol{u} = 0$ is implicitly used) non-dimensional form of the time-dependent incompressible Navier-Stokes equation (2.9) can be written as follows:

$$\frac{\partial \boldsymbol{u}}{\partial t} = -\left(\boldsymbol{u} \cdot \nabla\right) \boldsymbol{u} - \nabla p + \frac{1}{\mathrm{Re}} \nabla^2 \boldsymbol{u}. \tag{5.66}$$

Multiplying the time-variant form of the Navier-Stokes equation (5.66) by the fluid velocity $\boldsymbol{u}$, with the help of some mathematical expressions and the divergence theorem after integrating over the design domain D. The following expression can be obtained:

$$\int_D \boldsymbol{u} \cdot \frac{\partial \boldsymbol{u}}{\partial t} dD = \int_\Gamma \left(-\boldsymbol{u}\frac{1}{2}\boldsymbol{u}^2 - p\boldsymbol{u} + \frac{1}{\mathrm{Re}}\left(\nabla \boldsymbol{u} + \nabla \boldsymbol{u}^T\right) \cdot \boldsymbol{u}\right) \cdot \boldsymbol{n} \, d\Gamma - \int_\Omega \frac{1}{\mathrm{Re}} \nabla \boldsymbol{u} : \left(\nabla \boldsymbol{u} + \nabla \boldsymbol{u}^T\right) d\Omega. \tag{5.67}$$

Therefore, the corresponding dissipated kinetic energy and the pressure drop can be obtained by distinguishing the internal-domain integral Ω and the boundary-domain integral Γ, respectively. They can be defined as follows:

- The objective functional corresponds to the dissipated kinetic energy is as,

$$\dot{E} = -\frac{1}{\mathrm{Re}} \int_\Omega \nabla \boldsymbol{u} : \left(\nabla \boldsymbol{u} + \nabla \boldsymbol{u}^T\right) d\Omega. \tag{5.68}$$

- The objective functional corresponds to the pressure drop is as,

$$\dot{Q} = -\int_{\Gamma_{\mathrm{in}} \cup \Gamma_{\mathrm{out}}} \boldsymbol{u} \left(\frac{1}{2}\boldsymbol{u}^2 + p\right) \cdot \boldsymbol{n} d\Gamma. \tag{5.69}$$

Here, the no-slip boundary condition $\boldsymbol{u} = 0$ on Γ_w and the condition for a fully-developed flow $\int_{\Gamma_{\mathrm{in}} \cup \Gamma_{\mathrm{out}}} \frac{1}{\mathrm{Re}} \left(\nabla \boldsymbol{u} + \nabla \boldsymbol{u}^T\right) : (U\boldsymbol{n} \otimes \boldsymbol{n}) \; d\Gamma = 0$ are implicitly used, where $\Gamma = \Gamma_{\mathrm{in}} \cup \Gamma_{\mathrm{out}} \cup \Gamma_w$ denotes the structural boundary, $\boldsymbol{n}$ denotes the normal vector, U is the characteristic velocity between inlet and outlet of the fully-developed flow [29]. The same expression of the two objective functionals written in the index notation shown in the beginning of Section 5.2.

Table 5.2 shows the summary of these specified parameters used in the various objective functional problems. The initial settings of this problem shown in above and demonstrate by the Fig. 5.4. The periodic inflow-outflow boundary conditions (5.59) are used to this transient problem. The objective functional corresponds to the dissipation kinetic energy

Table 5.2: The specified parameters used in the various objective functional problems

Mesh size $[\Delta x]$	Re	Inlet width L $[\Delta x]$	Mean velocity U_o	Viscosity ν	Relaxation time τ_B
50×50	32	16 $(a = 34, b = 18)$	1×10^{-1}	1×10^{-1}	0.8

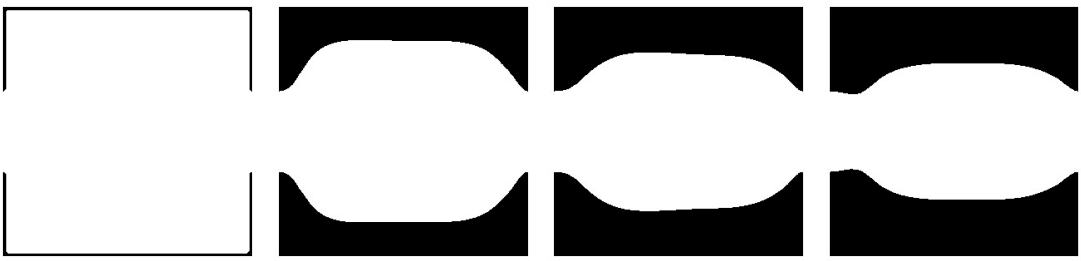

(a) Step = 1 (b) Step = 50 (c) Step = 100 (d) Final step

Case I: Dissipated kinetic energy problem

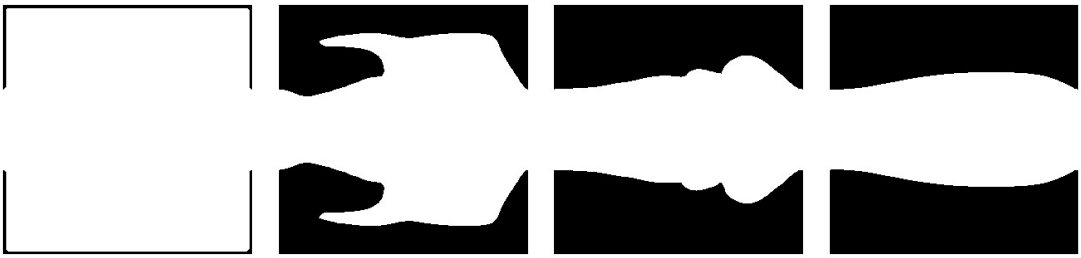

(e) Step = 1 (f) Step = 50 (g) Step = 100 (h) Final step

Case II: Pressure problem

Figure 5.5: The optimization histories obtained in the minimization problem.

and the objective functional corresponds to the pressure drop are employed from Eq. (5.56) and Eq. (5.57), respectively. In this numerical example, the same numerical groundwork for the transient flow (Eq. (5.59)) is used to visualize the differences of the optimized shapes obtained by using the objective functional corresponds to pressure drop vice versa the dissipation kinetic energy. Mathematically, the main different aspect of using the the two objective functionals is the evaluation of the function taken either in the internal

domain or the boundaries at inlet and outlet. There are significant differences are obtained from the uses of this two kinds of the function of interests in this numerical example for both the minimization and maximization problems. It is noted that in the minimization problem, the objective functional (5.60) and the initial conditions of the adjoint system (5.61) are used while the objective functional (5.62) and the initial conditions of the adjoint system (5.63) are used in the maximization problem, respectively.

Figure 5.5 shows the optimization histories obtained in the minimization problem for the two cases correspond to the uses of dissipation kinetic energy and the pressure drop for the function of interest in the numerical demonstration. In general, the optimal configurations obtained by the two cases are similar, even though some differences are observed from theirs local minimums. To be more specific, the fluid flows between the inlet and out let are encouraged to transport freely without any restriction during the optimization process. As a consequence, it avoids the loss of kinetic energy or the pressure drop of the fluid flows in the two examples.

In fluid dynamics, the objective functional corresponds to the minimization dissipated kinetic energy is often used as a standard function in the flow control and optimization [108]. However, in the topology optimization problem using the continuous adjoint lattice Boltzmann method, there is a need to use the finite difference scheme to compute the velocity gradient existing in the objective functional corresponds to the dissipation kinetic energy [109, 55]. Thus, leading to the extra cost in the topology optimization as compared to the topology optimization where the objective functional corresponds to the pressure drop. Therefore, in the minimization problem, the use of the cost function corresponds to the pressure drop results to a better computation cost, since there is no need of an extra finite difference scheme to compute the velocity gradient term in the adjoint system (exists in the in the integrand $A^{'}$ in Eq. (5.6)). The explicit expression of the velocity differential equations are sufficiently given in the Appendices section (B).

Figure 5.6 shows the optimization histories obtained in the maximization problem for the two cases correspond two the uses of dissipation kinetic energy and the pressure drop for the function of interest. In contrast to the minimization problem above, the significant differences are observed from the maximization problems using the the objective functionals correspond to the dissipation energy and the pressure drop. In the former, the obstacles tend to be generated in the internal domain and nearby the inlet and outlet. It

potentially stops the free transport of fluid flow from inlet and outlet results to the increase of kinetic energy losses during its movements. Unlikely, in the maximization problem using the objective functional corresponds to the pressure drop, the optimized shapes show a complete restriction of the fluid flows in the internal domain by blocking off the inlet at the first optimization step and closing off the outlet after next optimization steps. The optimization configuration ended up by a complete absence of the fluid flow inside the internal domain (no fluid flows between inlet and outlet) leading to a critical increase of the loss of kinetic energy. The observations can be explained by the uses of different objective functionals where it is considered at the internal nodes or at the boundary nodes. This important feature needs to be taken into account for the maximization problem where the uses of dissipation kinetic energy and the pressure drop as a function of interest results in different optimal configurations.

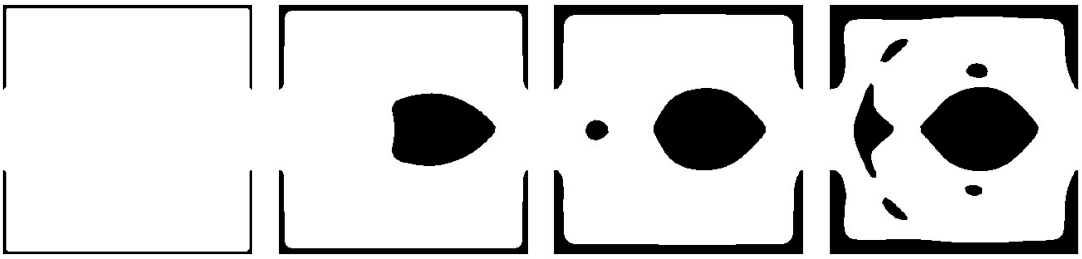

(a) Step = 1 (b) Step = 25 (c) Step = 100 (d) Final step

Case I: Dissipated kinetic energy problem

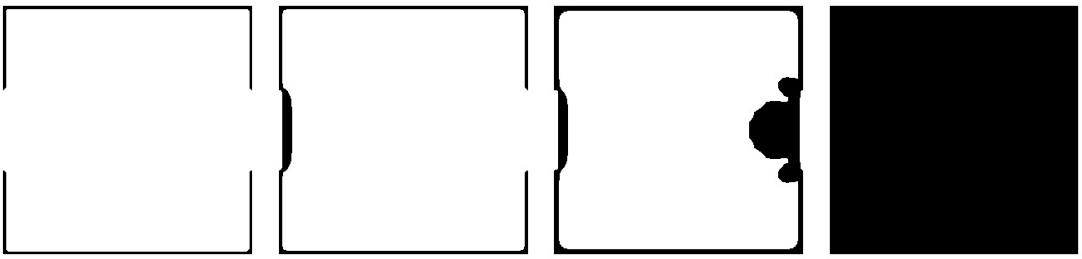

(e) Step = 1 (f) Step = 5 (g) Step = 20 (h) Final step

Case II: Pressure drop problem

Figure 5.6: The optimization histories obtained in the maximization problem.

5.2.3 Minimization and maximization problems

In this section, the same objective functional is used to evaluate the differences of the minimization and maximization problems using the proposed method. The emphasis of using objective functional corresponds to the dissipation kinetic energy (5.56) has shown in the previous numerical example. Therefore, this objective functional will be considered for the rest of following numerical demonstrations in this study.

The critical factor to converse a minimization problem to a maximization problem is adding a minus sign to the objective functional. To be more specific, the minimization problem will be conversed to the maximization problem if it is implemented by the objective functional with a minus sign. Thus, leading to the inverse signs of the intergrands A' and B' in the initial conditions of the adjoint Boltzmann equation (5.6). Those differences have been summarized in the beginning of Section 5.2 along with some common design settings for the numerical framework. To be more specific, while the minimization problem uses the objective functional (5.60) and the initial conditions of the adjoint system (5.61) in their framework, the maximization problem uses the objective functional (5.62) and the initial conditions of the adjoint system (5.63) in the computation. Other than that, the same periodic boundary conditions are used for both the minimization and maximization problems in the transient flows of this numerical example. It is written as follows:

$$\begin{cases} U_{in} = U_o \dfrac{(y-b)(a-y)}{1/4(a+b)^2 - ab} \sin(\omega t) & \text{on } \Gamma_{\text{in}}, \\ \rho_{out} = 1 & \text{on } \Gamma_{\text{out}}, \end{cases} \qquad (t \in [0, 2\pi]). \tag{5.70}$$

Table 5.3: The specified parameters used in the minimization and maximization problems

Mesh size $[\Delta x]$	Re	Inlet width L $[\Delta x]$	Mean velocity U_o	Viscosity ν	Relaxation time τ_B
50×50	50	50 $(a = 51, b = 1)$	1×10^{-1}	1×10^{-1}	0.8

Table 5.3 shows the summary of these specified parameters used in the minimization and maximization problems. Fig. 5.7 shows the initial setting of the diffuser used in this numerical example. It is initially filled with full of fluid at the state of rest.

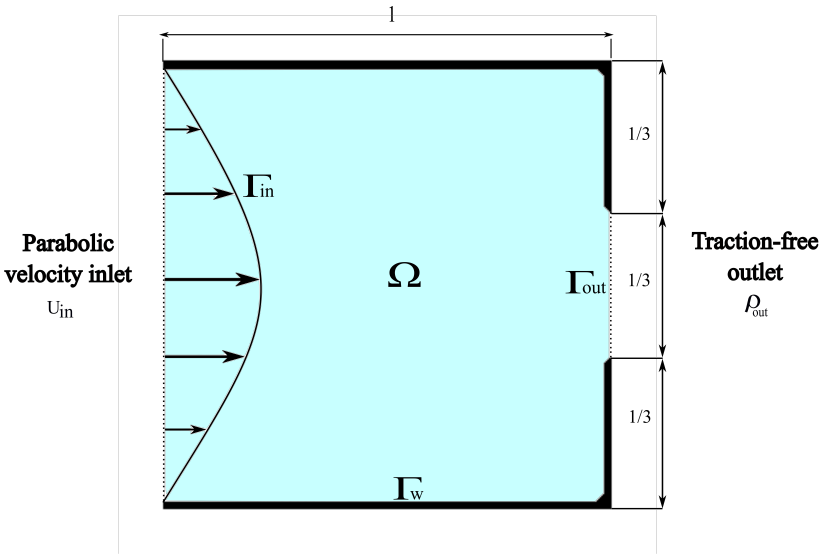

Figure 5.7: Design setting of the diffuser.

Figure 5.8 shows the optimization histories obtained by the unsteady minimization and maximization problems. In the case I of this numerical example, the minimization problem generated a noticeably simple optimized shapes that allowing the flow driven freely between inlet and outlet. There is no observation of solid obstacles occupied the transition of flow. The straight channel is generated to inspire the fluid flows freely from left to right and vice versa. It results to the decrease of the kinetic energy losses during the fluid flow immigrates between inlet and outlet.

Unlikely, in the case II of this numerical example, an opposite of physical property is observed as compared to the minimization problem. The presence of solid objects shows in the entire optimization steps. They are generated nearby the inlet and outlet, then, continuously developed until reaching the permissible volume constraint. The optimized shape finally merged the two obstacles generated near the inlet and outlet to one and occupied the center of the cavity. This leads the fluid flows in a longer and more curved than just a straight path resulting to a loss of kinetic energy while transportations. By using the sinusoidal velocity inlet, the fluid can be either pump in or pump out the internal domain from the inlet by each 1/2 time interval ($t = [0, \pi]$) and ($t = [\pi, 2\pi]$), respectively. Therefore, in a complete time interval ($t = [0, 2\pi]$), the fluid flows is always continuously restricted by a solid island leading to the noticeable loss of kinetic energy in total. This behavior is completely opposite to what was observed in the minimization problem above.

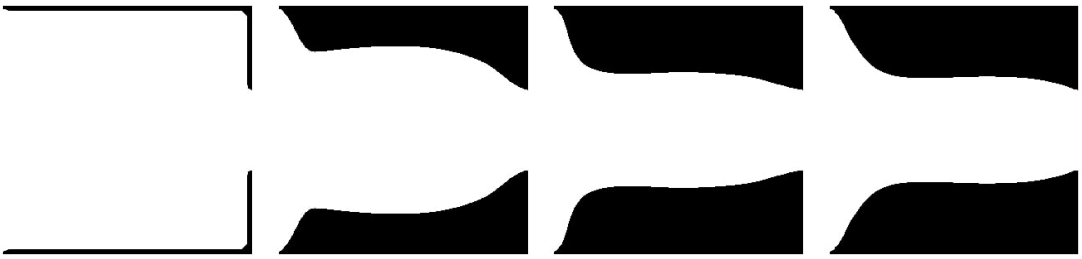

(a) Step = 1 (b) Step = 25 (c) Step = 50 (d) Final step

Case I: Minimization problem

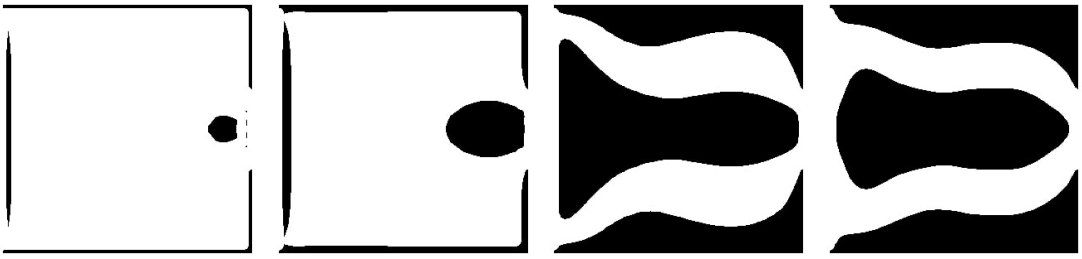

(e) Step = 1 (f) Step = 25 (g) Step = 50 (h) Final step

Case II: Maximization problem

Figure 5.8: The optimization histories obtained by the unsteady minimization and maximization problems.

The performance of this numerical demonstration has show in Fig. 5.9 and Fig. 5.10 for the convergence histories of the objective functional and volume constraint in the minimization problem and in the maximization problems, respectively. Their smooth convergences shown in both the minimization and maximization problems indicating that the obtained solutions are sufficiently validated. The up-side-down convergence configurations of the objective functional between the minimization problem and maximization problem well agreed with the mathematical point of view wherein the minimization problem is implemented by the objective functional with a minus sign added to that of the maximization problem.

In the applications of topology optimization, especially, to the design of fluidic devices, the results obtained by maximizing the objective functional corresponds to the dissipated energy are essentially needed in some particular problems [28, 29]. Therefore,

the achievement has shown in this numerical example certifies the applicability of the proposed method in the development of such devices wherein the optimal solutions of the topology optimization for transient flows orientated by the cost function corresponds to dissipated energy are demanded, particularly, not only for the minimization but also the maximization problems.

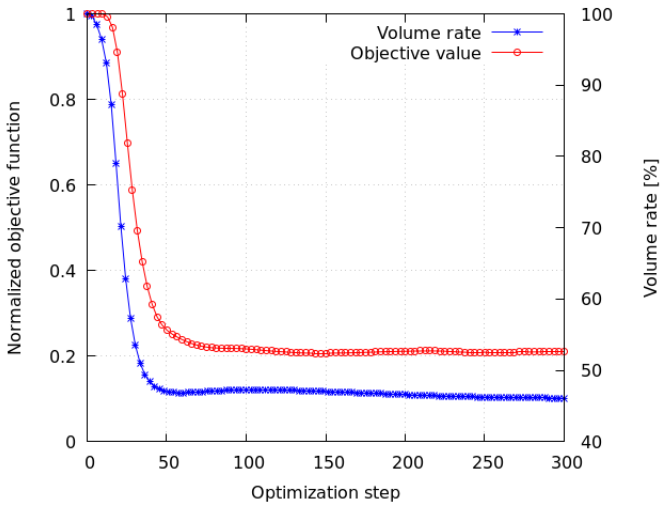

Figure 5.9: Convergence histories of the objective functional and volume constraint of the minimization problem.

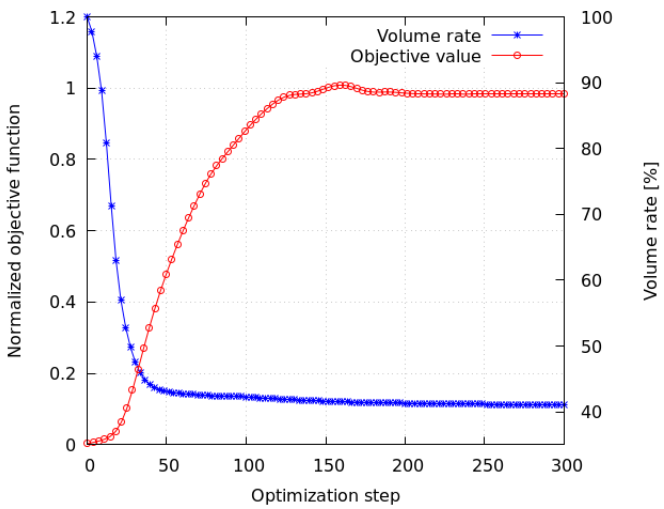

Figure 5.10: Convergence histories of the objective functional and volume constraint of the maximization problem.

5.2.4 One-directional flow and bi-directional flow problems

In this numerical example, the minimization and maximization problems for the single and bi-directional flows are examined in contrast. The periodic unsteady boundary conditions Eq. (5.59) are used. The objective functional corresponds to the dissipation kinetic energy (5.56) is employed in all cases. Aiming to design the symmetric channel for fluid devices where the oscillation boundary conditions are concerned, this numerical example is conducted to examine the potential symmetries of the optimal shapes. The optimizations are defined as the following,

- The topology optimization for *single direction flow* is formulated as follows:

$$\begin{aligned} \min_{\phi} J|_{t=t_1} &= \int_I \int_\Omega A\left(\rho, \frac{\partial u_i}{\partial x_j}\right) dt d\Omega + \int_I \int_\Gamma B\left(\rho, \boldsymbol{u}\right) dt d\Gamma, \\ \text{subject to} \quad & \text{Governing equations (single direction flow)}, \\ & V = \int_D \chi_\phi \, d\Omega - V_{\max} \leq 0. \end{aligned} \tag{5.71}$$

- The topology optimization for *bidirectional oscillation flow* is formulated as follows:

$$\begin{aligned} \inf_{\phi} J^*|_{t=t_1} &= \alpha_1 \cdot J_{\text{for}} + \alpha_2 \cdot J_{\text{rev}} \\ \text{subject to} \quad & \text{Governing equations (forward flow)}, \\ & \text{Governing equations (reverse flow)}, \\ & V = \int_D \chi_\phi \, d\Omega - V_{\max} \leq 0, \end{aligned} \tag{5.72}$$

where $J^*|_{t=t_1}$ denotes the total objective functional which is proportional to the objective functional of the forward flow J_{for} and the objective functional of the reverse flow J_{rev}. Here, the demonstration of the forward and reverse flows is shown in Fig. 5.11. The weighting constants α_1 and α_2 are simply designed by 0.5 in this study to ensure the neutral contribution of the objective functionals in the forward and reverse flows that effects to the optimization results.

For the optimization of single direction flow problem, the design settings are the same in the first numerical example for straight channel design (shown in Subsection 5.2.2). However, in the topology optimization of bi-directional flow problem, the inflow-outflow boundary conditions (5.59) used for the reverse flow will be adjusted such that the prescribed velocity inlet is set on the vertical right-end with a reverse direction and the

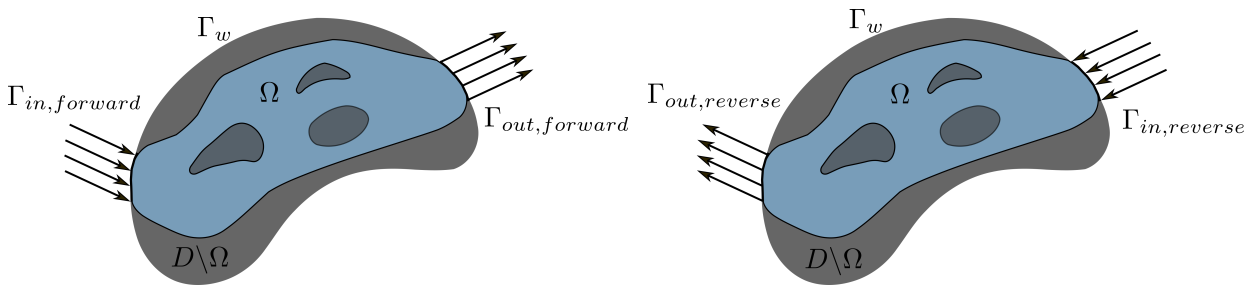

(a) The design domain of the forward flow (b) The design domain of the reverse flow

Figure 5.11: The demonstration for the forward and reverse flows in an optimization.

prescribed pressure boundary conditions is placed on the vertical left-end with a reverse direction as well (see Fig. 5.11). The evaluation of the total Lagrangian objective functional ($\bar{J}^*$) can be defined using the method proposed by Krause et al. [110] as follows:

$$\bar{J}^* = J_{\text{for}} + J_{\text{rev}} + \lambda_{\text{for}} R_{\text{for}} + \lambda_{\text{rev}} R_{\text{rev}}. \tag{5.73}$$

$$\bar{J}^{*\prime} = \bar{J}'_{\text{for}} + \bar{J}'_{\text{rev}} = \underbrace{\frac{\partial J_{\text{for}}}{\partial \phi} + \lambda_{\text{for}} \frac{\partial R_{\text{for}}}{\partial \phi}}_{\delta_\phi \bar{J}_{\text{for}}} + \underbrace{\frac{\partial J_{\text{rev}}}{\partial \phi} + \lambda_{\text{rev}} \frac{\partial R_{\text{rev}}}{\partial \phi}}_{\delta_\phi \bar{J}_{\text{rev}}} = 0 \tag{5.74}$$

where R_{for}, J_{for}, R_{rev}, and J_{rev} denotes the residual of the governing equations and objective functional for the forward flow, the residual of the governing equations and objective functional for the reverse flow, respectively. Therefore, the total objective functional and design sensitivity can be computed by the average mean value with the relation of the weighting coefficients of the forward and reverse flows (α_1 and α_2).

Finally, the total objective functional $\bar{J}^*$ is involved to the time-evolution equation (5.3) for updating the optimal shapes. It is expressed as follows:

$$\begin{aligned}
&\frac{\partial \phi}{\partial t} = -K\left(\bar{J}^{*\prime} - \tau \nabla^2 \phi\right) \quad \text{in } \Psi \times D, \\
&\phi|_{t=0} = \phi_0 \quad \text{in } D, \\
&\frac{\partial \phi}{\partial n} = 0 \qquad \text{on } \Psi \times (\Gamma_{\text{in}} \cup \Gamma_{\text{out}}), \\
&\phi = -1 \qquad \text{on } \Psi \times \Gamma_w,
\end{aligned} \tag{5.75}$$

where the total objective functional for the bi-directional flow denoted by $\bar{J}^*$.

Table 5.4 shows the summary of these specified parameters used in the one-directional flow and bi-directional flow problems. Figure 5.12 shows the design settings for the forward

Table 5.4: The specified parameters used in the one-directional flow and bi-directional flow problems

Mesh size $[\Delta x]$	Re	Inlet width L $[\Delta x]$	Mean velocity U_o	Viscosity ν	Relaxation time τ_B
50×50	32	16 $(a = 34, b = 18)$	1×10^{-1}	1×10^{-1}	0.8

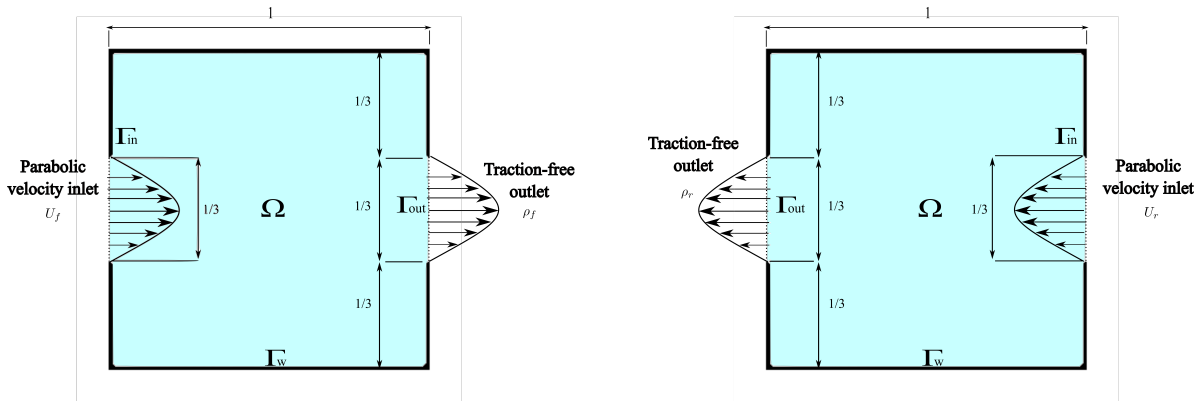

(a) The design setting of the forward flow

(b) The design setting of the reverse flow

Figure 5.12: The design settings for the forward and reverse flows in an optimization.

and reverse flows in a optimization. Both the designs for the forward and reverse flows are initially at state of rest with filled by fluid state.

Figure 5.13 shows the optimization histories obtained by single direction and bi-directional flows maximization problem. The common observation of this maximization problem for the two different flows is the characteristics of the maximization results where there is the creation of solid object in the internal domain. This phenomena is for preventing the direct transportation through the internal media from inlet to outlet. The flow is consequently separated into several paths which are longer and more curved as compared to a straightforward flow from inlet to outlet. It is, moreover, observed a unique characteristic for the results of the bi-directional flow wherein the symmetric configurations are obtained iteratively in all optimization time steps (case II), as compared to the single direction flow wherein the solid obstacles are created regionally (asymmetric configuration) and developed in a different manner (case I).

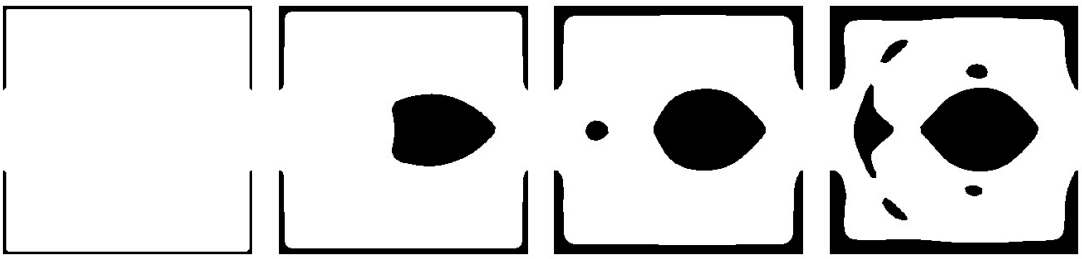

(a) Step = 1 (b) Step = 25 (c) Step = 100 (d) Final step

Case I: Single direction flow

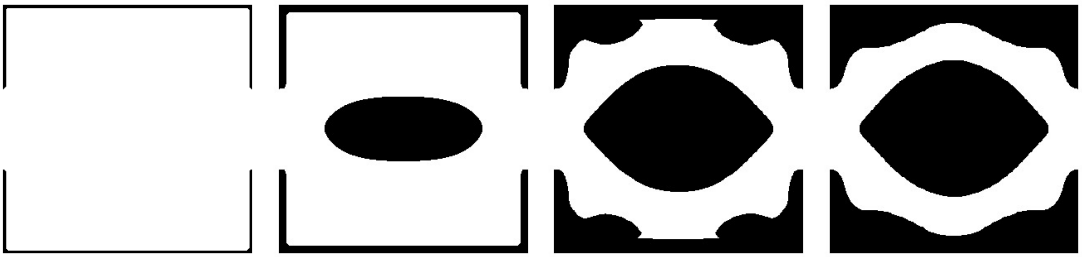

(e) Step = 1 (f) Step = 15 (g) Step = 30 (h) Final step

Case II: Bi-directional flow

Figure 5.13: The optimization histories obtained by single direction and bi-directional flows maximization problem.

Figure 5.14 shows the optimal configurations obtained by single direction and bi-directional flows minimization problem. The considerably simple configurations are obtained in the minimization of the two problems as compared to the maximization problem. The symmetric configurations are, still, observing in the in the bi-directional flow optimization. This complies with the purpose of creation the fluid devices to adapt the oscillation conditions of the fluid flows.

In general, the characteristics of the two problems are admittedly complies with one another. However, the symmetries obtained in the optimization for bi-directional flow maybe favorable in designing the fluid devices that requires the symmetric balance conditions. It is noted that for different design purposes, the change in the different weighting coefficients α_1 and α_2 can be adjusted to fulfill the needs. It is, however, the effects of the weighting coefficients in topology optimization for flow field will be considered in our

future extension, especially, in the design for time-dependent fluid devices.

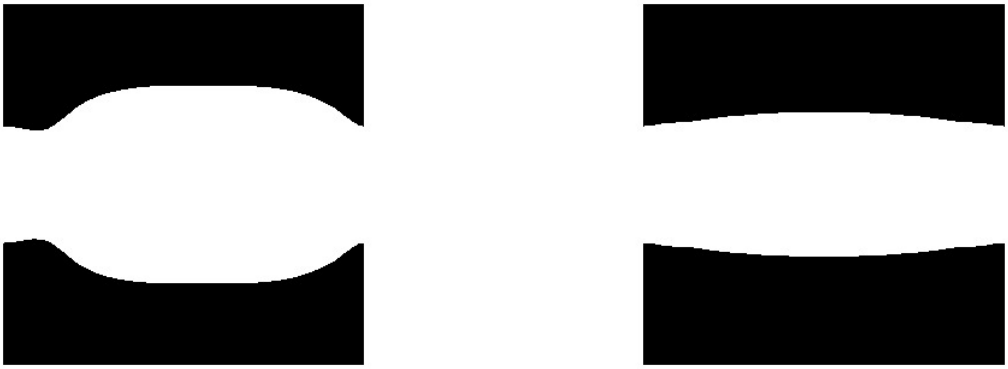

(a) The single direction flow (b) The bi-directional flow

Figure 5.14: The optimal configurations obtained by single direction and bi-directional flows minimization problem.

5.2.5 Steady flow and unsteady flow problems

This section aims to strengthen the object of this study is for the unsteady flow optimization wherein the objective functional used corresponds to the dissipation kinetic energy. Therefore, the necessary use of the transient optimization scheme in a topology optimization for the unsteady flow field problem is appropriately validated. It is, moreover, for further robust the validation, the comparison of the transient solutions to steady-state counterparts is sufficiently performed. The cross-comparisons between the steady-state optimal designs and transient optimal designs, and not only for minimization problem but also maximization problem are correspondingly presented.

In topology optimization for transient problem using LBM, the complete history of the solutions of the state variables need to be entirely stored for the calculation of the adjoint problem backward in time [98, 55]. It is, however, the computational efficiency between the unsteady and steady problems that using LBM is not considered in this study. While the same transient optimization conditions are used for both the transient and and steady problems, a steady boundary condition is simply used in the case of the steady problem and a transient boundary condition is used in the case of the unsteady problem. The different boundary conditions are highlighted in the pairs inflow-outflow

boundary conditions Eq. (5.58) and Eq. (5.70) for the steady case and the transient case, respectively. The differences between the minimization and maximization problems are highlighted in the equations of different objective functionals (Eq. (5.60) and Eq. (5.62)) and the equations for initial conditions of the adjoint problem (Eq. (5.61) and Eq. (5.63)) in beginning of Section 5.2. The initial design settings are the same in the settings of the diffuser problem shown in Fig. 5.7 and the summary of these specified parameters used in the steady flow and unsteady flow problems are shown in Tab. 5.5.

Table 5.5: The specified parameters used in the steady flow and unsteady flow problems

Mesh size $[\Delta x]$	Re	Inlet width L $[\Delta x]$	Mean velocity U_o	Viscosity ν	Relaxation time τ_B
50×50	50	50 $(a = 51, b = 1)$	1×10^{-1}	1×10^{-1}	0.8

As a result, Fig. 5.15 shows the optimization histories obtained by steady and unsteady flows minimization problem. The obtained results in all optimization steps in the steady case and unsteady case are quite similar. The tendency of encouraging the direct fluid flows between the inlet and outlet is observed in the two cases. It is, however, the more curved of the boundaries in a cavities are realized in the transient case. This creation is positively made from the oscillations of the unsteady flow while transporting inside the internal cavities and recognized also in the previous study [103].

Figure 5.16 shows the optimization histories obtained by steady and unsteady flows maximization problem. In the steady case, the solid obstacle is soon generated next to inlet and developed quickly to prevent the straightforward flow from inlet to outlet. It is stopped when when the volume constraint is satisfied. The solid object located nearby the inlet highly restrict the steady fluid flows freely in the straight path resulting to a significant increase of kinetic energy losses during transportations of the flow. In a similar manner, this characteristic is happened in both sided of the cavities during all the optimization time steps in the unsteady flow problem. As a similar explanation in Subsection 5.2.3, this reason may come from the physical phenomena of the oscillating flow conditions, where it is able to flow back and forth through the internal cavities in each 1/2 time interval $(t = [0, \pi])$ and $(t = [\pi, 2\pi])$, respectively. The islands generated nearby the inlet and outlet (shown in Figs. 5.16e and 5.16f) are developed until they

merged as one obstacle. It is continuously placed at the center of cavities resulting to the restriction of a free and straightforward flow between inlet and outlet. The dissipation kinetic energy is, then, significantly increased.

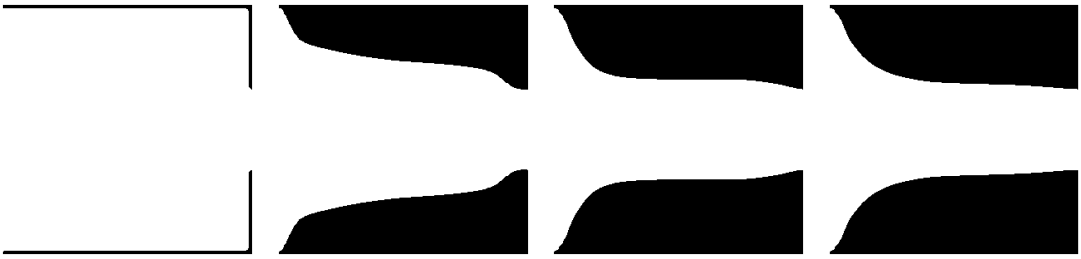

(a) Step = 1 (b) Step = 25 (c) Step = 50 (d) Final step

Case I: Steady flow

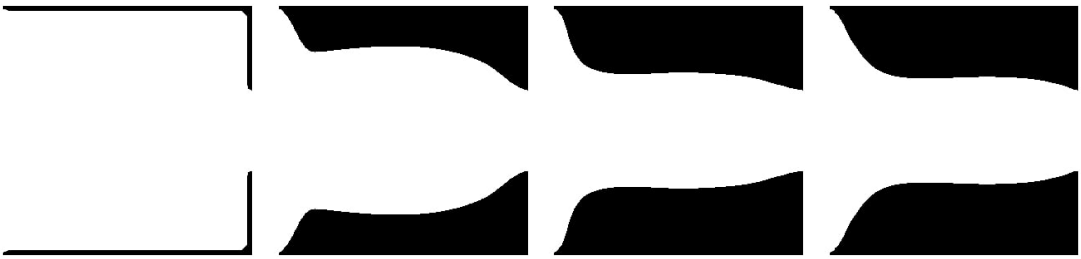

(e) Step = 1 (f) Step = 25 (g) Step = 50 (h) Final step

Case II: Unsteady flow

Figure 5.15: The optimization histories obtained by steady and unsteady flows minimization problem.

To examine the necessary utilization of the transient topology optimization for unsteady flow field, the cross-comparisons of the optimal shapes obtained by the steady-state topology optimization and the unsteady topology optimization are correspondingly conducted. By varying the characteristics of the inflow, e.g., changing the Reynolds numbers and the flow frequencies, the significant use of the transient optimization pattern in the topology optimization for unsteady flow field is probably shown. It is noted that for the steady flow, the steady boundary conditions are simply imposed at the inlet and outlet while the same transient framework has remained for simplification.

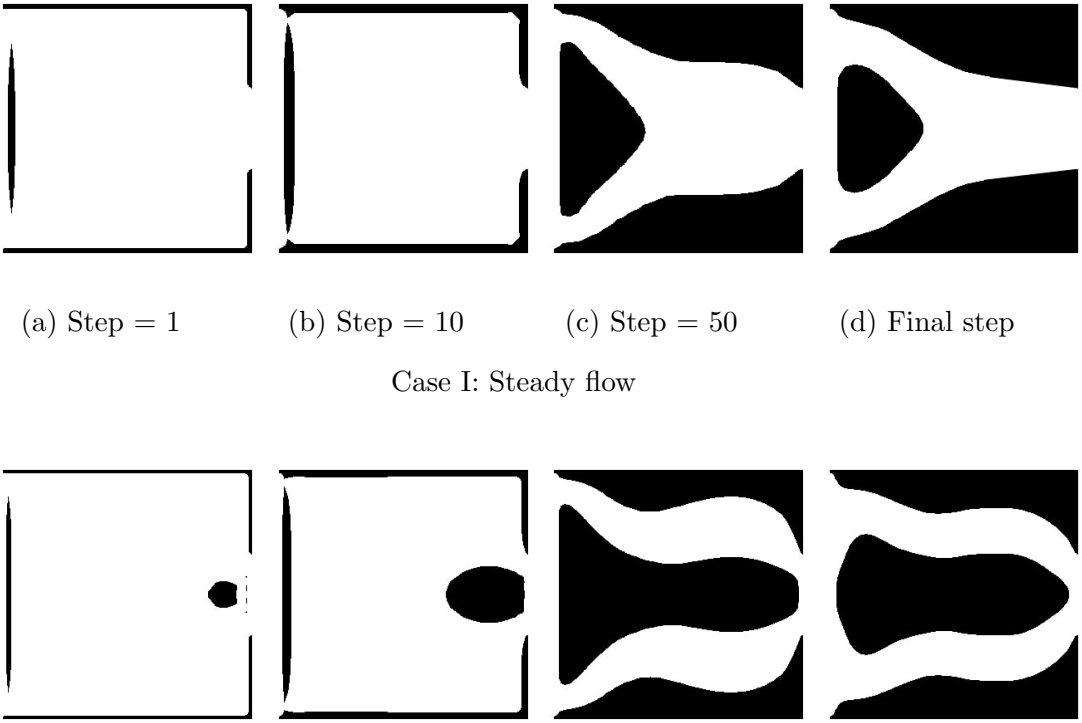

(a) Step = 1 (b) Step = 10 (c) Step = 50 (d) Final step

Case I: Steady flow

(e) Step = 1 (f) Step = 10 (g) Step = 50 (h) Final step

Case II: Unsteady flow

Figure 5.16: The optimization histories obtained by steady and unsteady flows maximization problem.

In the first comparison, the optimal configurations obtained in the minimization problem (Fig. 5.15) are used as the initial designs. The optimal shape obtained by the steady-state optimization problem (5.15d) is used as the initial design for the transient optimization problem (a periodic inflow-outflow boundary conditions (5.59) are used) while the optimal shape obtained by unsteady optimization (5.15h) is used as the initial design for the steady optimization problem (a constant inflow-outflow boundary conditions (5.58) are used). The same objective functional corresponds to the dissipation energy (5.56) is used in the two problems. Their values obtained by the steady-state scheme and the unsteady scheme are recorded and shown in Tab. 5.6. The comparative improvement shows that the steady-state optimal shape performs better in the steady-state optimization scheme while the unsteady optimal shape performs better in the transient optimization scheme.

Also, by increasing the inflow frequencies (at the same Re = 50), the transient optimization scheme behaves better performance to the steady-state scheme. The details of this comparison are shown in Fig. 5.7

Table 5.6: The comparison in optimal results between steady and unsteady cases in various Re numbers

Re	Boundary condition	Objective value of steady-state optimal shape [S]	Objective value of transient optimal shape [T]	The comparative improvement [(T-S)/S]
10	Steady-state	1.6159	1.6612	+2.8%
	Transient	0.5627	0.5226	-7.1%
25	Steady-state	4.3838	4.5512	+3.8%
	Transient	1.4195	1.3127	-7.5%
50	Steady-state	11.2506	11.7146	+4.1%
	Transient	2.9618	2.7254	-8.0%

Table 5.7: The comparison in optimal results of transient case in various flow frequencies (Re = 50)

Flow frequency	Boundary condition	Objective value of steady-state optimal shape [S]	Objective value of transient optimal shape [T]	The comparative improvement [(T-S)/S]
1/360	Transient	2.9618	2.7254	-8.0%
1/90	Transient	1.0255	0.9135	-10.9%
1/60	Transient	0.4097	0.3543	-13.5%

In the second comparison, the optimal shape obtained by the steady-state optimization problem (5.15d) and the optimal shape obtained by unsteady optimization (5.15h) are used as the initial designs to perform the transient optimization for evaluation of their performances. To examine the the straightforward flow resistance in a transient prob-

lem, the inflow velocity at a center point located on the vertical left-end boundary and the outflow velocity at a center point located on the vertical right-end boundary of the two cases are fully plotted. As a result, Fig. 5.17 shows that the performance of the optimal shape obtained by the unsteady optimization problem has better straightforward flow resistance ability as compared to the performance of the optimal shape obtained by the steady-state optimization problem. Therefore, the loss of kinetic energy during transportation in the optimal cavity obtained by the unsteady optimization problem will be higher. The two cross-comparisons in this study have shown the interest of using the optimal designs obtained by the unsteady optimization for the transient problems to increase their performances.

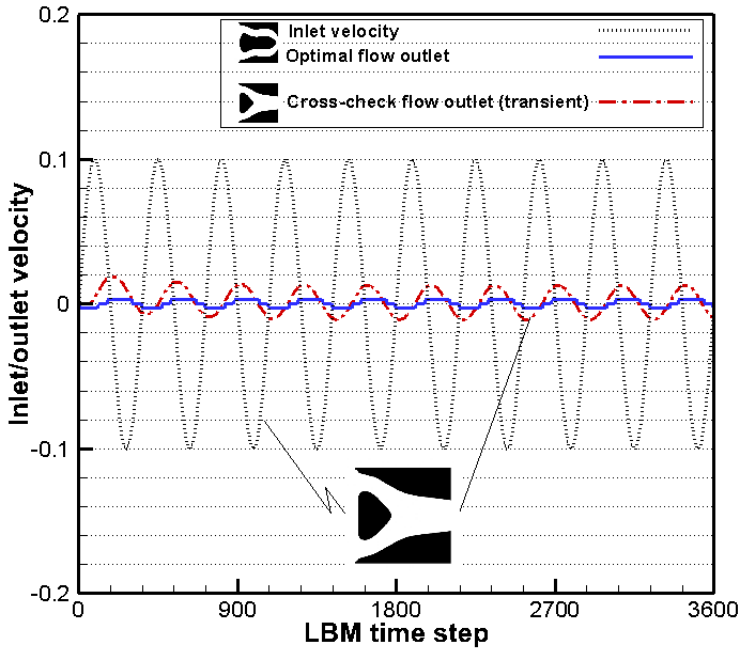

Figure 5.17: The cross-comparison of performance of the steady-state optimal shape and unsteady optimal shape for the transient optimization scheme.

Chapter 6

Topology Optimization for Thermal Conduction using LBM

In Chapter 5, the former research for the flow field optimization problem has been successfully presented with interesting results. It is, however, the design sensitivity (the gradient of the function of interest) is derived using the continuum derivative (Eq. (4.13)) that is based on the continuous adjoint lattice Boltzmann method (ALBM). As a result, the design sensitivity ends up with the continuous form containing the microscopic variables (Eq. (5.15)). Nevertheless, in topology optimization based on the level-set method, the gradient information of the function of interest used in the level-set method is more natural to compute with the macroscopic variables such as macroscopic density, macroscopic pressure, macroscopic velocity, or macroscopic temperature. Therefore, in this chapter, the more rigorous topology optimization based on the level-set method applied to the heat conduction is constructed wherein the gradient information of the function of interest is computed by the topological change. This computation is entitled as the topological derivative (Eq. (4.14)). The topological change in this work corresponds to the removing/inserting an infinitesimal solid circular from/to the original domain. As a consequence, the topological derivative only consists of the macroscopic variables such as macroscopic temperature and the adjoint temperature (Eq. (6.7)). The validation of this proposed methodology is done through several numerical demonstrations consisting of direct comparisons with one found in literature wherein the conventional method is used. The performance of this method is also compared to the previous research wherein the conventional method is used instead of the LBM in the current work. It is essentially noted that those computational time

values in the comparisons are just for references since the parallel computation method is used in the LBM while none of the fast algorithms are used in the conventional method (i.e., the BEM). The purpose of the comparisons is to certify the capability of high parallel computation efficiency of the LBM and also to verify the interest of using the LBM in the topology optimization for thermal conduction. The computational comparison over the FEM seems to be better than the FEM since the FEM is more popular in heat conduction problems. It is, however, the topology optimization for heat conduction using FEM has not been conducted during this time. Therefore, this research will be considered in a future study to clarify this concern.

6.1 Formulation for a topology optimization

6.1.1 Level-set based topology optimization for thermal field problem

In this structure topology optimization, the scalar level-set function $\phi(\boldsymbol{x})$ is introduced as a numerical method for representing the material distribution Ω, the non-material distribution $D\backslash\Omega$, and the structural boundaries $\partial\Omega$ of them in the fixed design domain D. It is expressed as follows:

$$\begin{cases} 0 < \phi(\mathbf{x}) \leq 1 & \mathbf{x} \in \Omega\backslash\partial\Omega, \\ \phi(\mathbf{x}) = 0 & \mathbf{x} \in \partial\Omega, \\ -1 \leq \phi(\mathbf{x}) < 0 & \mathbf{x} \in D\backslash\Omega, \end{cases} \tag{6.1}$$

where $\boldsymbol{x}$ denotes a specific position in the fixed design doamin D. Likely, the previous topology optimization for flow field, the characteristic function $\chi_\phi(\boldsymbol{x})$, Eq. (5.2), is used to represent the existence of the material in the entire design domain D.

Next, employing the method of updating the new design variables by solving the reaction-diffusion equation [68] with the help of the derivative of a given objective function J, the time-evolution level-set function is expressed as follows:

$$
\begin{aligned}
&\frac{\partial \phi}{\partial t} = K\left(\mathcal{T}_D + \tau \nabla^2 \phi\right) && \text{in } D, \\
&\phi|_{t=0} = \phi_0 && \text{in } D, \\
&\frac{\partial \phi}{\partial n} = 0 && \text{on } \partial D \backslash \Gamma_w, \\
&\phi = 1 && \text{on } \Gamma_w,
\end{aligned}
\tag{6.2}
$$

where $K > 0$ is the proportional parameter, t denotes the fictitious time, $\mathcal{T}_D$ denotes the topological derivative or the sensitivity of the objective function J. τ denotes the regularization parameter for designing the degree of complexity for optimal shapes. ϕ_0 denotes the initial value of ϕ at initial time $t = 0$. The non-design boundary denoted by Γ_w which is not changed during optimization process.

Let us now construct the topology optimization in order to minimize an objective function J wherein it is considered in the material region Ω and/or on the boundary Γ. The topology optimization can be formulated as follows:

$$
\min_{\phi} J\left(\chi_\phi\right) = \int_{\Omega} J_\Omega\left(T\right)\ d\Omega + \int_{\Gamma} J_\Gamma\left(T, Q\right)\ d\Gamma,
$$

subject to

$$
\begin{aligned}
&-k\nabla^2 T = 0 && \text{in } \Omega \backslash \partial\Omega, \\
&T = \bar{T} && \text{on } \Gamma_D, \\
&Q = -k\frac{\partial T}{\partial n} = \bar{Q} && \text{on } \Gamma_N, \\
&Q = h(T - T_\infty) && \text{on } \Gamma_h,
\end{aligned}
\tag{6.3}
$$

and

$$
G = \int_{D} \chi_\phi d\Omega - G_{\max} \leq 0, \tag{6.4}
$$

where the functions of interest specified in the material region Ω and on the boundary Γ denoted by J_Ω and J_Γ, respectively. T denotes the temperature and Q denotes the heat flux. The thermal conductivity denoted by k, the heat transfer coefficient denoted by h, and the ambient temperature denoted by T_∞. Here, the prescribed temperature $\bar{T}$ employed on Γ_D (Dirichlet boundary), the prescribed heat flux $\bar{Q}$ employed on Γ_N (Neumann boundary), and the Robin boundary (Γ_h) is implicitly imposed on the new boundaries generated during optimization process. G denotes the volume constraint and $G_{\max}$ denotes the permissible material volume of the optimal configuration obtained.

In this study, the use of the time-evolution equation (6.2) in finding the feasible distribution of material is considered. Besides, the Lagrange's multiplier is employed, and the adjoint variable $\mathcal{W}$ can be obtained by solving the following boundary value problem (BVP):

$$\begin{aligned}
-k\nabla^2\mathcal{W} &= \frac{\partial J_\Omega}{\partial T} && \text{in } \Omega, \\
\mathcal{W} &= -\frac{\partial J_\Gamma}{\partial Q} && \text{on } \Gamma_D, \\
\eta &= \frac{\partial J_\Gamma}{\partial T} && \text{on } \Gamma_N, \\
\eta &= h\left(\mathcal{W} + \frac{\partial J_\Gamma}{\partial Q} + \frac{1}{h}\frac{\partial J_\Gamma}{\partial T}\right) && \text{on } \Gamma_h,
\end{aligned} \tag{6.5}$$

where

$$\eta = -k\frac{\partial \mathcal{W}}{\partial n}. \tag{6.6}$$

It is noted that the topological derivative $\mathcal{T}_D$ in the reaction-diffusion (6.2) is obtained with the help of the adjoint method. It is, then, computed by using the solutions of the primal system (6.3) and the adjoint system (6.5). As a result, the expression of the topological derivative is as follows:

$$\mathcal{T}_D = \mathcal{W}^0 h\left(T^0 - T_\infty\right) + \left(T^0 - \hat{T}\right)^2, \tag{6.7}$$

where $\hat{T}$ is the target temperature. Here, the topological derivative wherein the Robin boundary condition defined on the infinitesimal circular Ω_ε with the boundary Γ_ε is shown. The asymtotic expansion of the temperature T and temperature adjoint $\mathcal{W}$ from the center of Ω_ε results to the notations T^0 and $\mathcal{W}^0$ as their values at their center points, respectively. The objective function specified on the boundary domain including the boundary of the new hole generated in the topological derivation process Γ_ε, $J_\Gamma = |T - \hat{T}|^2$, is implicitly employed. The detail analysis is, then, shown in the next section.

6.1.2 The adjoint problem and topological derivative

This part is inspired by the work done by Jing et al. [41] where the topological derivative of a design-dependent objective functional is comprehensively presented. The following derivation is, therefore, referenced by his study.

In order to relax the equality constraints and inequality constraints the the topology optimization described in Eqs. (6.3)-(6.4), the Lagrange's method is used. The uncon-

strained problem is, then, described as follows:

$$\min_{\phi} \bar{J} = J(\phi) + B + \lambda G, \tag{6.8}$$

where the Lagrangian objective function denoted by $\bar{J}$ and the Lagranges multiplier denoted by $\lambda \ni R$. The real function B is determined as follows:

$$B = \int_D \mathcal{W}\left(-k\nabla^2 T\right)\ d\Omega = 0. \tag{6.9}$$

By applying the Karush-Kuhn-Tucker conditions to the optimization above (6.8), it yields,

$$J' + B' + \lambda = 0, \quad \lambda G = 0, \quad \lambda \geq 0, \quad G \leq 0, \tag{6.10}$$

where J' and B' denote the variation of J and B with respect to the topological change, respectively. Specifically, the variation of J and B caused by the topological change can be denoted by the topological derivative when there is an infinitesimal circular hole is generated during the optimization process, $\mathcal{T}_D = J' + B'$.

Next, using the integration by parts to the Lagrangian objective function, $J := J + B$, the new expression of J is as follows:

$$\begin{aligned} J := J + B &= \int_\Gamma J_\Gamma(T, Q)\ d\Gamma + \int_\Omega J_\Omega(T)\ d\Omega + \int_\Omega \mathcal{W}\nabla \cdot (-k\nabla T)\ d\Omega \\ &= \int_\Gamma J_\Gamma\ d\Gamma + \int_\Omega J_\Omega\ d\Omega + \int_\Gamma \mathcal{W}Q\ d\Gamma - \int_\Omega \nabla\mathcal{W} \cdot (-k\nabla T)\ d\Omega. \end{aligned} \tag{6.11}$$

When there is a topological change as such removing an infinitesimal material circular Ω_ε from the material domain Ω, the Lagragian objective function J will be varied with an amount of δJ that corresponds to the variation δT and δQ in the temperature field. Thus, the variation can be expressed as follows:

$$\begin{aligned} J + \delta J = &\int_\Gamma \left(J_\Gamma + \frac{\partial J_\Gamma}{\partial T}\delta T + \frac{\partial J_\Gamma}{\partial Q}\delta Q\right)\ d\Gamma + \int_\Omega \left(J_\Omega + \frac{\partial J_\Omega}{\partial T}\delta T\right)\ d\Omega \\ &+ \int_\Gamma \mathcal{W}(Q + \delta Q)\ d\Gamma - \int_{\Omega\setminus\Omega_\varepsilon} \nabla\mathcal{W} \cdot (-k\nabla T)\ d\Omega \\ &- \int_{\Omega\setminus\Omega_\varepsilon} \nabla\mathcal{W} \cdot (-k\nabla\delta T)\ d\Omega + \int_{\Gamma_\varepsilon} \mathcal{W}(Q + \delta Q)\ d\Gamma \end{aligned} \tag{6.12}$$

By subtracting the equation (6.11) from (6.12), the variation δJ is given as follows:

$$
\begin{aligned}
\delta J = & \int_{\Gamma_D \cup \Gamma_N \cup \Gamma_h} \left(\frac{\partial J_\Gamma}{\partial T} \delta T + \frac{\partial J_\Gamma}{\partial Q} \delta Q \right) \, d\Gamma + \int_\Omega \frac{\partial J_\Omega}{\partial T} \delta T \, d\Omega + \int_{\Gamma_D \cup \Gamma_N \cup \Gamma_h} \mathcal{W} \delta Q \, d\Gamma \\
& - \int_{\Omega \setminus \Omega_\varepsilon} \nabla \mathcal{W} \cdot (-k \nabla \delta T) \, d\Omega + \int_{\Gamma_\varepsilon} \mathcal{W}(Q + \delta Q) \, d\Gamma + \int_{\Omega_\varepsilon} \nabla \mathcal{W} \cdot (-k \nabla T) \, d\Omega \\
= & \int_{\Gamma_N} \frac{\partial J_\Gamma}{\partial T} \delta T \, d\Gamma + \int_{\Gamma_D} \frac{\partial J_\Gamma}{\partial Q} \delta Q \, d\Gamma + \int_{\Gamma_h} \left(\frac{\partial J_\Gamma}{\partial T} \delta T + \frac{\partial J_\Gamma}{\partial Q} h \delta T \right) \, d\Gamma \\
& + \int_{\Gamma_D} \mathcal{W} \delta Q \, d\Gamma + \int_{\Gamma_h} \mathcal{W} h \delta T \, d\Gamma - \int_{\Gamma_N} \eta \delta T \, d\Gamma - \int_{\Gamma_h} \eta \delta T \, d\Gamma \\
& - \int_{\Omega \setminus \Omega_\varepsilon} \left[\nabla \cdot (-k \nabla \mathcal{W}) - \frac{\partial J_\Omega}{\partial T} \right] \delta T \, d\Omega \\
& - \int_{\Gamma_\varepsilon} \eta \delta T \, d\Gamma + \int_{\Gamma_\varepsilon} \mathcal{W}(Q + \delta Q) \, d\Gamma + \int_{\Omega_\varepsilon} \nabla \mathcal{W} \cdot (-k \nabla T) \, d\Omega
\end{aligned}
\tag{6.13}
$$

where

$$
\eta := -k \frac{\partial \mathcal{W}}{\partial n} \tag{6.14}
$$

From the above equation (6.13), the adjoint system is constructed in order to eliminated some computations of δT and δQ. The corresponding adjoint equation (6.5) is obtained and the variation δJ becomes as follows:

$$
\delta J = - \int_{\Gamma_\varepsilon} \eta \delta T \, d\Gamma + \int_{\Gamma_\varepsilon} \mathcal{W}(Q + \delta Q) d\Gamma + \int_{\Omega_\varepsilon} \nabla \mathcal{W} \cdot (-k \nabla T) \, d\Omega \tag{6.15}
$$

By considering the Robin boundary condition on Γ_ε and the objective function $J_\Gamma = |T - \hat{T}|^2$ is implicitly defined on Γ_ε, the following topological derivative is obtained after applying some mathematical transformation techniques, it gives,

$$
\mathcal{T}_D = \lim_{\varepsilon \to 0} \frac{\delta J}{2\pi\varepsilon} = \mathcal{W}^0 h \left(T^0 - T_\infty \right) + \left(T^0 - \hat{T} \right)^2 . \tag{6.16}
$$

It should be noted that the comprehensive derivation of the topological derivative is referred to the study by Jing et al. [41].

6.2 Numerical verification

In order to validate the proposed method in this study, various numerical demonstrations will be examined in contrast with the previous research in the field of heat conduction problem. After that, several numerical examples are produced to compared the computational efficiency of the use of LBM in heat conduction problem. It is noted that the

straightforward comparisons to the study by Jing et al. [41] are conducted to validate the current study. In the aforementioned study, the boundary element method (BEM) are used by the authors to to tackle the state file and the adjoint field. However, in the same optimization manner, this study uses the LBM to replace the BEM in the previous study.

For the design settings in the optimization for heat conduction problem using BEM, the review of the study by Jing et al. [41] will provide the readers with sufficient information. It is, however, the necessary conditions need for the comparisons with the proposed study will be stated in this thesis. The common setting conditions used for the LBM in this study are given such as the relaxation time $\tau_h = 1$, the proportional coefficient $K = 1$, and the permissible volume constraint $G_{\max} = 80\%$ of the initial domain though all the numerical examples. The thermal conductivity is calculated using the Eq. (3.27) and the regularization parameter $\tau = 5 \times 10^{-3}$ is used in the Eq. (6.2) for most numerical examples, excepted for the comparisons for its effects to the optimal configurations. For those comparisons, the particular regularization parameters will be provided accordingly. The objective function to be minimize in this study is the design dependent objective function. It is given as follows:

$$J = \int_{\Gamma_h \cup \Gamma_\epsilon} \left(T - \hat{T}\right)^2 d\Gamma, \tag{6.17}$$

where $\hat{T}$ is the target temperature, as $\hat{T} = 10$ is given in all examples. The termination condition is determined as follows:

$$\frac{|J_\varsigma - J_{\varsigma-1}|}{J_\varsigma} < \varepsilon_{\text{opt}}, \tag{6.18}$$

where the optimization step denoted by ς, $\varepsilon_{\text{opt}} = 10^{-6}$ is set in all numerical examples.

6.2.1 The applicability of the LBM and topological derivative

In this numerical example, the design settings are shown in Fig. 6.1. The initial design domain is a square of $50\Delta x \times 50\Delta x$ lattice. It is filled by the material at the initial state. The prescribed temperature boundary condition $\bar{T} = 100$ is specified on Γ_D–Dirichlet boundary condition. On the Robin boundary condition–Γ_h, the heat transfer constant $h = 1$ and the ambient temperature $T_\infty = 0$ are given.

As a result, a good agreement of the obtained configurations at selected optimization steps is observed. Fig. 6.2 shows the optimization obtained by the two studies, the LBM

and the BEM at different optimization steps. In general, during optimization process, these holes are allowed to be generated and developed leading to the significant reduce of the objective function (it is shown in Fig. 6.4). The generation of the four void domains is similarly observed by the two method leading to the similarities of optimized configurations obtained in the mentioned study and the proposed study. It is noted that in the previous study by Jing et al. [41], the setting of regularization parameter τ and the proportional coefficient K are different with the proposed method due to the different optimization schemes between the two. Other than that, the initial and boundary conditions are the same in both the studies.

Figure 6.3 shows the distribution of temperature field at different optimization steps. It is observed the lower temperature inside these holes as compared to the outside temperature. Therefore, these holes are considered ad the heat absorbers wherein the heat transfer boundary condition is implicitly used during optimization process. This totally complies with the study using BEM in literature [41]. Additionally, the smooth convergences of the objective function and the volume constraint confirms the validity of the numerical results obtained, shown in Fig. 6.4. The applicability of the LBM in topology optimization of the heat conduction is, as expected, proved.

In this study, the effects by the variations regularization coefficient τ to the optimal configurations obtained are also examined. The different parameters τ are used in this numerical example such as $\tau = 1 \times 10^{-3},\ 5 \times 10^{-3},$ and 1×10^{-2}. As a consequence, Fig. 6.5 shows the different optimized configurations at different values of τ. As what is observed, the smaller values of τ the more complicated shapes can be obtained. This phenomena is well agreed with what shown in literature [68, 41].

In the second numerical example the non-square domain of $75\Delta x \times 100\Delta x$ lattice is used to test the wide-range applicabilities of the proposed method to various initial designs. Basically, all the initial and boundary conditions are the same with the previous example. The initial domain is filled by the material. It thermal conductivity is computed by Eq. (3.27). The regularization coefficient $\tau = 1 \times 10^{-2}$ is given and the termination condition is followed the Eq. (6.18).

Figure 6.6 shows the initial design setting and the corresponding optimal results of the non-square design problem. The appearances of the four holes during optimization process observed as in the previous example leading to the decrease of the objective value and the

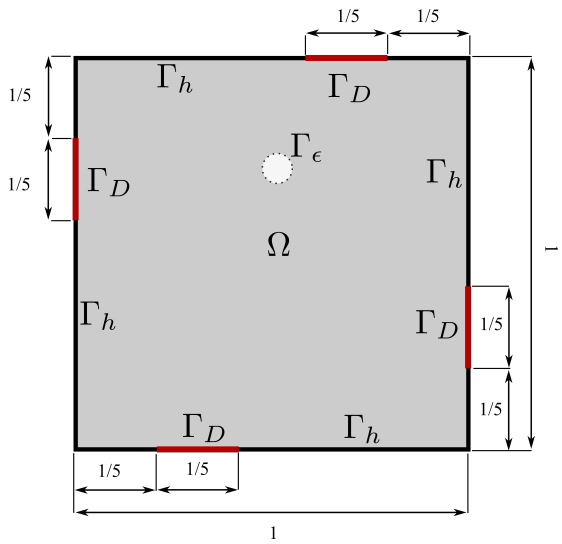

Figure 6.1: Design setting of the example 1.

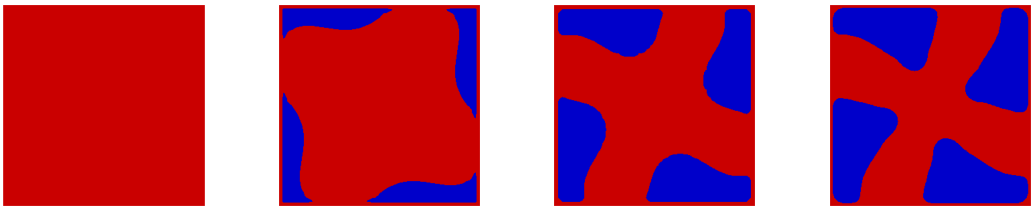

(a) Step = 1 (b) Step = 25 (c) Step = 100 (d) Final step

Case A: Lattice Boltzmann method

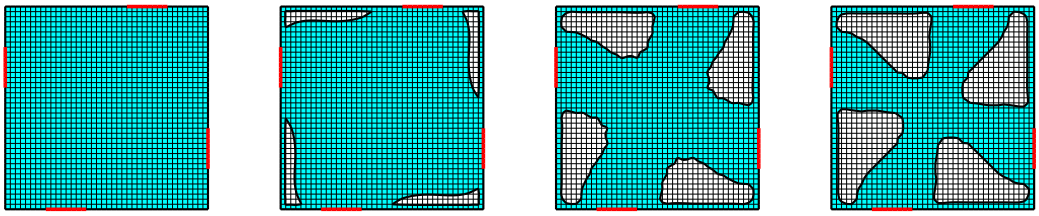

(e) Step = 1 (f) Step = 5 (g) Step = 20 (h) Final step

Case B: Boundary element method (taken from Jing et al., 2015)

Figure 6.2: The optimization histories obtained by different approaches.

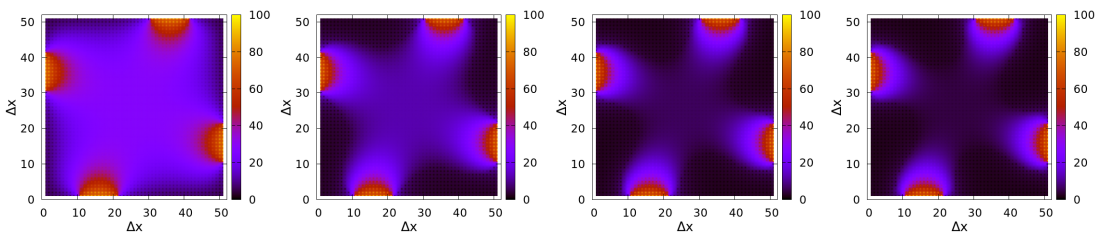

(a) Step = 1 (b) Step = 25 (c) Step = 100 (d) Final step

Figure 6.3: The temperature distribution at various steps.

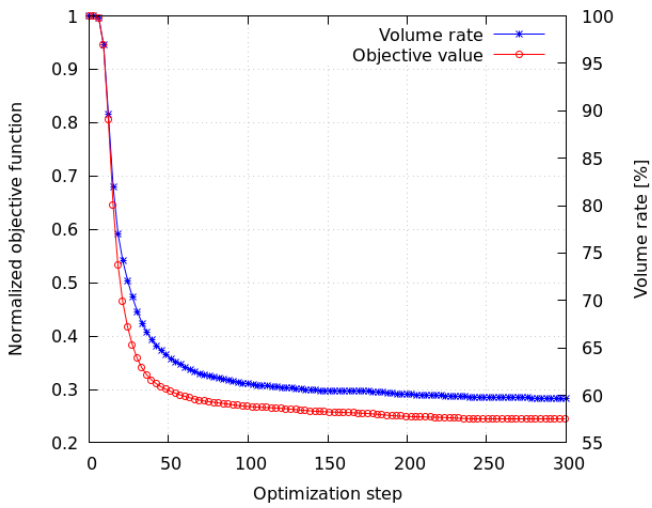

Figure 6.4: Convergence histories of normalized objective function and the volume constraint of the example 1.

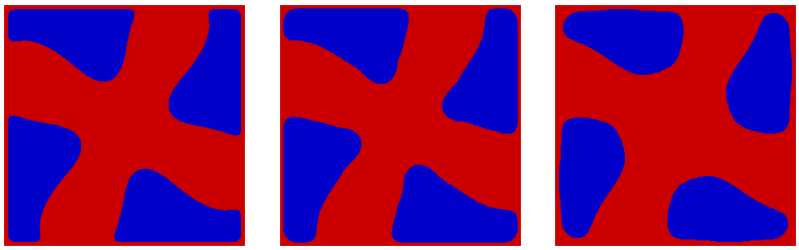

(a) $\tau = 1 \times 10^{-3}$ (b) $\tau = 5 \times 10^{-3}$ (c) $\tau = 1 \times 10^{-2}$

Figure 6.5: The different optimized shapes obtained by different τ.

volume constraint. The similar phenomena in generating the optimized shapes observed in this example and the above numerical example confirms the proposed method potentially works for different initial design domain in engineering design. It is, however, needed to test in the more complex boundary design problems, for that need, the more developed LBM to adapt such problems is considered and easily found in literature [111, 112, 113, 27].

The normalized topological derivative shown in Fig. 6.6b agrees with the optimized shape (Fig. 6.6c). the less smooth of those boundaries separating the feasible nodes (hot color) and the in-preferable node (cold color) are regularized by the diffusion term in the Eq. (6.2). As a result, the smoother boundaries are obtained in the optimized shapes. This penalty is often used in the previous studies [68, 41], by controlling such parameter τ the complexity of the optimal results can be generally manage. It is, however, the very small

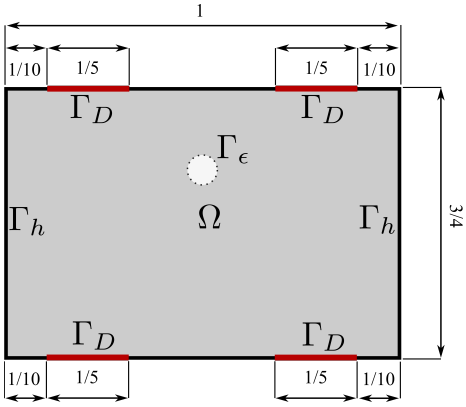

(a) Design setting of the example 2

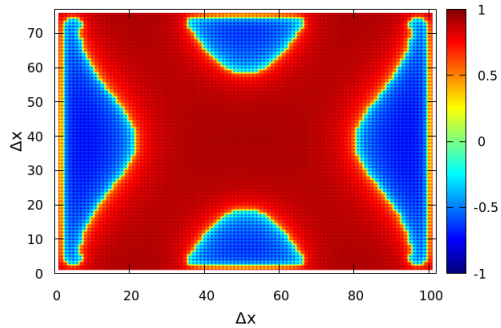

(b) Normalized topological derivative

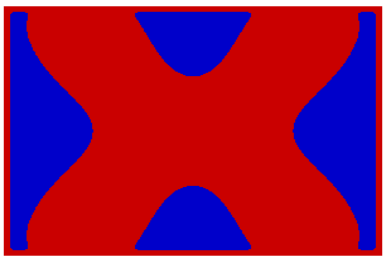

(c) Optimized shape

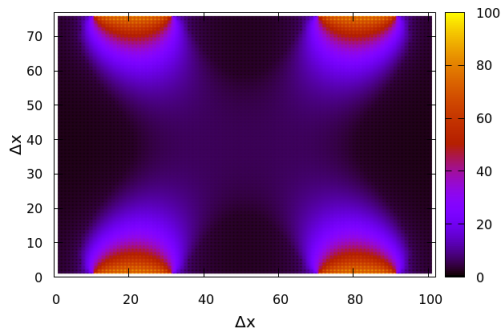

(d) Temperature distribution

Figure 6.6: The design setting and optimized results of the example 2.

of τ can create a very complex optimal shape, but it will be impossible to be manufactured if the shape is too complicated. Therefore, choosing inappropriate τ in order to generate a reliable shape is very important in developing such method in engineering design.

Figure 6.7 shows the convergence histories of the objective function and volume constraint in all optimization steps. All the objective value and the volume constraint are met the convergence conditions. Thus, the obtained results can be considered as the reliable solutions.

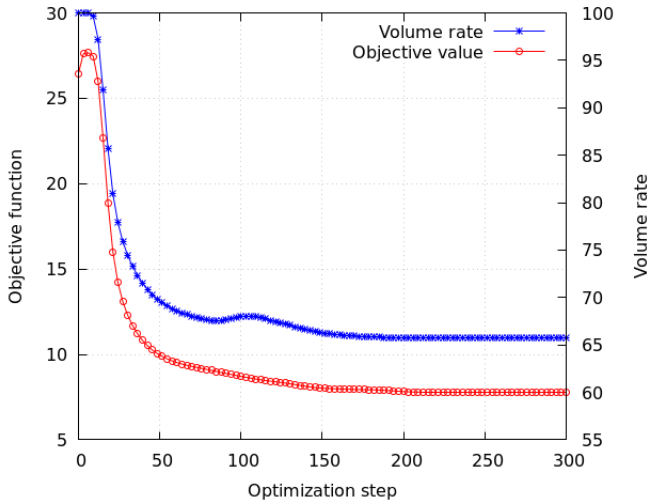

Figure 6.7: Convergence histories of objective function and the volume constraint of the example 2.

6.2.2 Computational efficiency compared to BEM

In this numerical example, a direct comparison of the computational efficiency of the topology optimization for the heat conduction problem using the new approach that corresponds to the LBM (produced by the proposed study) and the topology optimization for the heat conduction problem using the conventional method that corresponds to the BEM (produced by Jing et al., 2015) is considered. For this comparison, the numerical example 1 is selected to be tackled by the two approaches. All developed codes are written in Fortran. The specifications of the tested computer as such Intel Core I7-6700 3.40GHz CPU. As what is observed, a significant decreasing in the computation time in the topology optimization for heat conduction using LBM, as compared to the conventional method that solving the same problem by BEM. The detailed information of the computational time

for both the studties are sufficiently shown in Tab. 6.1. Comparatively, the computation time is efficiently saved in comparison to the BEM solver possibly comes from the free of use matrix solver in LBM program. Also, the parallel computation method used the LBM program can produce a good save. Therefore, it is confirmed that the effectiveness of using the LBM in topology optimization for the heat conduction problem.

Figure 6.8 shows the optimized shapes obtained by different approaches in different mesh sizes. The similar topologies of the optimal results obtained by the two different approaches confirms that the obtained results are certified as the optimal solutions. Therefore, the time recorded in the the Tab. 6.1 for computational time of the two methods are knowledgeable.

Table 6.1: The comparison of computional time in different mesh sizes by different methods

Mesh size [Δx]	Computational time of BEM [B]	Computational time of LBM [L]	The comparative improvement [(L-B)/B]
10×10	8.63199997	3.83159981	-55.6%
25×25	122.323997	21.8180008	-82.2%
50×50	909.200012	89.5059998	-90.2%
100×100	7581.43604	615.167188	-91.9%

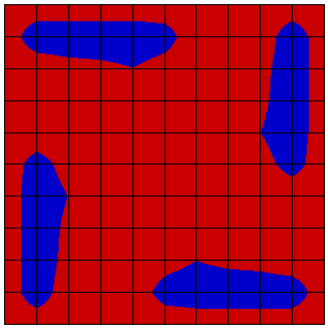

(a) $10\Delta x \times 10\Delta x$

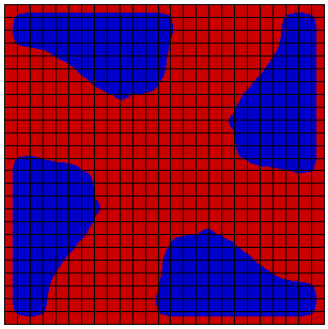

(b) $25\Delta x \times 25\Delta x$

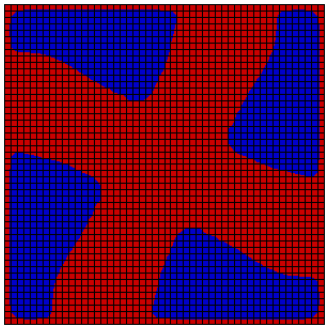

(c) $50\Delta x \times 50\Delta x$

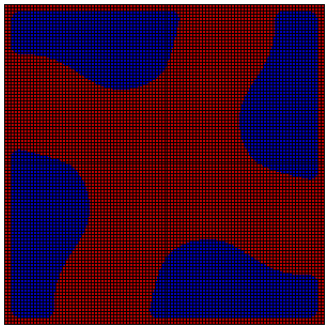

(d) $100\Delta x \times 100\Delta x$

Case A: Lattice Boltzmann method

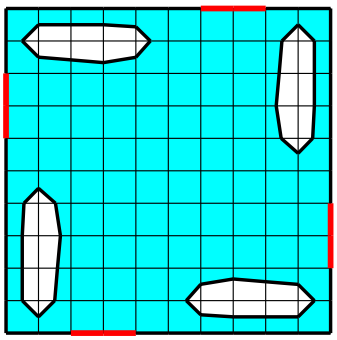

(e) $10\Delta x \times 10\Delta x$

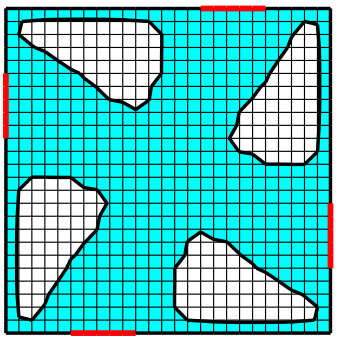

(f) $25\Delta x \times 25\Delta x$

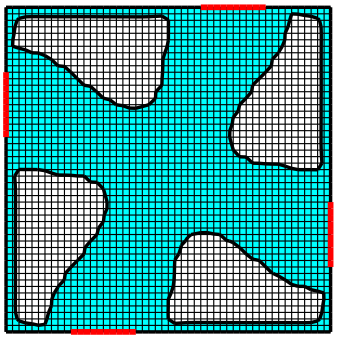

(g) $50\Delta x \times 50\Delta x$

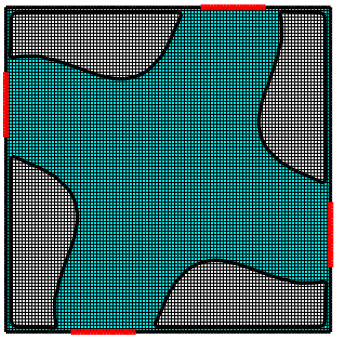

(h) $100\Delta x \times 100\Delta x$

Case B: Boundary element method (produced from Jing et al., 2015)

Figure 6.8: The optimized shapes obtained by different approaches in different mesh sizes.

Chapter 7

Conclusion

7.1 Summary

In the first study, the level-set based topology optimization for the flow field is successfully applied to various aspects of engineering demands, such as the problem for time-independent and time-dependent fluid flow, as well as concerning the minimization and maximization with various functions of interest (i.e., the pressure drop and the dissipated kinetic energy). This also presents the topology optimization for a single direction flow and multiple directional flows to fit with the needs in engineering design. The novelty of this part is the application of LBM in time-dependent flow with the function of interest that corresponds to the dissipation kinetic energy, which has an essential impact on designing the fluid devices for improving their performances.

In the second study, the level-set based topology optimization for the material distribution based on the performance of the heat energy conducts infected by the designated function of interest is performed. The original contribution in this work is the successful uses of the LBM in topology optimization for the heat conduction problem, which has a novel contribution to the literature development of the heat energy device. The high parallel efficiency is, then, certified by comparing with the one using the conventional method, i.e., the boundary element method. The significant improvement in computation time as compared to the conventional method based evaluating the interest of LBM in the topology optimization problem itself in which the high capability of parallel computation in LBM plays an important role and is generally validated in this work. Another important contribution of this work is the primary collaboration of the topological derivative concept

and the LBM in the level-set based topology optimization for heat conduction problem, leading to the more rigorous topology optimization based on the level-set method.

7.2 Future work

In the future development of the topology optimization for flow field using LBM, the potential expansion of this study to the time-dependent fluidic diode design is under consideration. Despite the majority of fluidic devices that have been developed (e.g., the Tesla valve application [27] and the fluidic design [28]), those applications are limited to the time-independent design. Thus, there is room for the development of time-dependent devices where the steady-state conditions are not satisfied. In the current study, the weight coefficients w_1 and w_2 and the inflow frequencies are simple leading to the simple optimal results obtained. Thus, to expand the current problem to the more complicated problem by using different ranges of the weight coefficients and the oscillating frequencies of the velocity inlet/outlet is interested. In these applications, the benefit of using the Pareto frontier method [29] can result in an interesting outcome. Moreover, the application of the turbulence flow conditions can also be a potential evolution for developing fluidic devices wherein the function of interest regarded the energy dissipation is considered.

Furthermore, in the future study, of the topology optimization for the thermal field using LBM, the potential expansion of this study to different initial design problems with more complex boundary design wherein the heat transfer boundary condition is explicitly employed on the design-dependent boundaries is demanded. Additionally, the successful collaboration of the topological derivative approach and the LBM in a level-set based topology optimization leads this methodology to a potential development for a more rigorous topology optimization level-set based on the N-S flow and the heat transfer problems that using the LBM. It is, however, for the complex boundary design problem, the use of a topological derivative approach that desire an appropriate discretization scheme with the high accuracy manner of the LBM. Therefore, the investigation in enhancing the better accuracy and efficiency of the LBM used for those topology optimizations needs further studies. The high-order discretization class of the LBM [114, 115, 116, 117] is an effective candidate to improve the proposed methodology.

Bibliography

[1] Joshua D Deaton and Ramana V Grandhi. A survey of structural and multidisciplinary continuum topology optimization: post 2000. *Structural and Multidisciplinary Optimization*, 49(1):1–38, 2014.

[2] Hemant Kumar Singh. *Development of optimization methods to deal with current challenges in engineering design optimization*. University of New South Wales, Australian Defence Force Academy, School of , 2011.

[3] Shiyi Chen and Gary D Doolen. Lattice Boltzmann method for fluid flows. *Annual review of fluid mechanics*, 30(1):329–364, 1998.

[4] Zhaoli Guo, Baochang Shi, and Nengchao Wang. Lattice BGK model for incompressible Navier–Stokes equation. *Journal of Computational Physics*, 165(1):288–306, 2000.

[5] Sauro Succi. *The lattice Boltzmann equation: for fluid dynamics and beyond*. Oxford university press, 2001.

[6] M Yoshino, Y Matsuda, and C Shao. Comparison of accuracy and efficiency between the lattice Boltzmann method and the finite difference method in viscous/thermal fluid flows. *International Journal of Computational Fluid Dynamics*, 18(4):333–345, 2004.

[7] XF Pan, Aiguo Xu, Guangcai Zhang, and Song Jiang. Lattice Boltzmann approach to high-speed compressible flows. *International Journal of Modern Physics C*, 18(11):1747–1764, 2007.

[8] FL Hinton, MN Rosenbluth, SK Wong, YR Lin-Liu, and RL Miller. Modified lattice Boltzmann method for compressible fluid simulations. *Physical Review E*, 63(6):061212, 2001.

[9] Takeshi Kataoka and Michihisa Tsutahara. Lattice Boltzmann method for the compressible euler equations. *Physical review E*, 69(5):056702, 2004.

[10] Moran Wang and Qinjun Kang. Modeling electrokinetic flows in microchannels using coupled lattice Boltzmann methods. *Journal of Computational Physics*, 229(3):728–744, 2010.

[11] Jianying Zhang, Guangwu Yan, and Yinfeng Dong. A new lattice Boltzmann model for the Laplace equation. *Applied Mathematics and Computation*, 215(2):539–547, 2009.

[12] A Hiorth, UH a Lad, S Evje, and SM Skjaeveland. A lattice Boltzmann-BGK algorithm for a diffusion equation with robin boundary conditionapplication to nmr relaxation. *International journal for numerical methods in fluids*, 59(4):405–421, 2009.

[13] Miki Hirabayashi, Yu Chen, and Hirotada Ohashi. The lattice BGK model for the Poisson equation. *JSME International Journal Series B Fluids and Thermal Engineering*, 44(1):45–52, 2001.

[14] Zhenhua Chai and Baochang Shi. A novel lattice Boltzmann model for the Poisson equation. *Applied mathematical modelling*, 32(10):2050–2058, 2008.

[15] Jinku Wang, Moran Wang, and Zhixin Li. Lattice Poisson–Boltzmann simulations of electro-osmotic flows in microchannels. *Journal of colloid and interface science*, 296(2):729–736, 2006.

[16] Zhenhua Chai and Baochang Shi. Simulation of electro-osmotic flow in microchannel with lattice Boltzmann method. *Physics Letters A*, 364(3-4):183–188, 2007.

[17] S Ponce Dawson, S Chen, and Gary D Doolen. Lattice Boltzmann computations for reaction-diffusion equations. *The Journal of chemical physics*, 98(2):1514–1523, 1993.

[18] Jianying Zhang and Guangwu Yan. A lattice Boltzmann model for the reaction-diffusion equations with higher-order accuracy. *Journal of Scientific Computing*, 52(1):1–16, 2012.

[19] Xiaoyi He and Li-Shi Luo. Theory of the lattice Boltzmann method: From the Boltzmann equation to the lattice Boltzmann equation. *Physical Review E*, 56(6):6811, 1997.

[20] G Brenner, Th Zeiser, K Beronov, P Lammers, and J Bernsdorf. Lattice Boltzmann methods: High performance computing and engineering applications. In *Parallel Computational Fluid Dynamics 2002*, pages 3–12. Elsevier, 2003.

[21] Christian Obrecht. *High performance lattice Boltzmann solvers on massively parallel architectures with applications to building aeraulics*. PhD thesis, 2012.

[22] K. Yaji, T. Yamada, M. Yoshino, and T. Matsumoto. Topology optimization using the lattice Boltzmann method incorporating level set boundary expressions. *Computational Physics*, 274:158–181, 2014.

[23] Kentaro Yaji. Topology optimization using the lattice Boltzmann method and applications in flow channel designs considering thermal and two-phase fluid flows. 2016.

[24] K. Yaji, T. Yamada, M. Yoshino, T. Matsumoto, K. Izui, and S. Nisiwaki. . , 13(18-131129), 2013.

[25] Allan Gersborg-Hansen, Ole Sigmund, and Robert B Haber. Topology optimization of channel flow problems. *Structural and multidisciplinary optimization*, 30(3):181–192, 2005.

[26] Sebastian Kreissl, Georg Pingen, Anton Evgrafov, and Kurt Maute. Topology optimization of flexible micro-fluidic devices. *Structural and Multidisciplinary Optimization*, 42(4):495–516, 2010.

[27] Georg Pingen, Anton Evgrafov, and Kurt Maute. A parallel schur complement solver for the solution of the adjoint steady-state lattice Boltzmann equations: application to design optimisation. *International Journal of Computational Fluid Dynamics*, 22(7):457–464, 2008.

[28] Sen Lin, Longyu Zhao, James K Guest, Timothy P Weihs, and Zhenyu Liu. Topology optimization of fixed-geometry fluid diodes. *Journal of Mechanical Design*, 137(8), 2015.

[29] Yuki Sato, Kentaro Yaji, Kazuhiro Izui, Takayuki Yamada, and Shinji Nishiwaki. Topology optimization of a no-moving-part valve incorporating Pareto frontier exploration. *Structural and Multidisciplinary Optimization*, 56(4):839–851, 2017.

[30] Casper Schousboe Andreasen, Allan Roulund Gersborg, and Ole Sigmund. Topology optimization of microfluidic mixers. *International Journal for Numerical Methods in Fluids*, 61(5):498–513, 2009.

[31] David Makhija, Georg Pingen, Ronggui Yang, and Kurt Maute. Topology optimization of multi-component flows using a multi-relaxation time lattice Boltzmann method. *Computers & fluids*, 67:104–114, 2012.

[32] Truong Nguyen, Hiroshi Isakari, Toru Takahashi, Kentaro Yaji, Masato Yoshino, and Toshiro Matsumoto. Level-set based topology optimization of transient flow using lattice Boltzmann method considering an oscillating flow condition. *Computers & Mathematics with Applications*, 80(1):82–108, 2020.

[33] Adriano A Koga, Edson Comini C Lopes, Helcio F Villa Nova, Cícero R De Lima, and Emílio Carlos Nelli Silva. Development of heat sink device by using topology optimization. *International Journal of Heat and Mass Transfer*, 64:759–772, 2013.

[34] T Zhang, ZW Yan, L Xiao, HD Fu, G Pei, and J Ji. Experimental, study and design sensitivity analysis of a heat pipe photovoltaic/thermal system. *Applied Thermal Engineering*, 162:114318, 2019.

[35] Joe Alexandersen and Casper Schousboe Andreasen. A review of topology optimisation for fluid-based problems. *Fluids*, 5(1):29, 2020.

[36] T Dbouk. A review about the engineering design of optimal heat transfer systems using topology optimization. *Applied Thermal Engineering*, 112:841–854, 2017.

[37] Seung-Hyun Ha and Seonho Cho. Topological shape optimization of heat conduction problems using level set approach. *Numerical Heat Transfer, Part B: Fundamentals*, 48(1):67–88, 2005.

[38] ChunGang Zhuang, ZhenHua Xiong, and Han Ding. A level set method for topology optimization of heat conduction problem under multiple load cases. *Computer Methods in Applied Mechanics and Engineering*, 196(4-6):1074–1084, 2007.

[39] Takayuki Yamada, Kazuhiro Izui, and Shinji Nishiwaki. A level set-based topology optimization method for maximizing thermal diffusivity in problems including design-dependent effects. *Journal of Mechanical Design*, 133(3):031011–9, 2011.

[40] Guoxian Jing, Toshiro Matsumoto, Toru Takahashi, Hiroshi Isakari, and Takayuki Yamada. Topology optimization for 2D heat conduction problems using boundary element method and level set method. *Transactions of JASCOME*, 13(19):5–10, 2013.

[41] Guoxian Jing, Hiroshi Isakari, Toshiro Matsumoto, Takayuki Yamada, and Toru Takahashi. Level set-based topology optimization for 2d heat conduction problems using bem with objective function defined on design-dependent boundary with heat transfer boundary condition. *Engineering Analysis with Boundary Elements*, 61:61–70, 2015.

[42] Benliang Zhu, Xianmin Zhang, Nianfeng Wang, and Sergej Fatikow. Optimize heat conduction problem using level set method with a weighting based velocity constructing scheme. *International Journal of Heat and Mass Transfer*, 99:441–451, 2016.

[43] Alberto Donoso and Pablo Pedregal. Optimal design of 2D conducting graded materials by minimizing quadratic functionals in the field. *Structural and Multidisciplinary Optimization*, 30(5):360–367, 2005.

[44] Allan Gersborg-Hansen, Martin P Bendsøe, and Ole Sigmund. Topology optimization of heat conduction problems using the finite volume method. *Structural and Multidisciplinary Optimization*, 31(4):251–259, 2006.

[45] Ercan Mehmet Dede. Multiphysics topology optimization of heat transfer and fluid flow systems. In *Proceedings of The COMSOL Users Conference*, 2009.

[46] Gilles Marck, Maroun Nemer, Jean-Luc Harion, Serge Russeil, and Daniel Bougeard. Topology optimization using the SIMP method for multiobjective conductive problems. *Numerical Heat Transfer, Part B: Fundamentals*, 61(6):439–470, 2012.

[47] Jaco Dirker and Josua Petrus Meyer. Topology optimization for an internal heat-conduction cooling scheme in a square domain for high heat flux applications. *Journal of Heat Transfer*, 135(11):111010–10, 2013.

[48] Francois H Burger, Jaco Dirker, and Josua Petrus Meyer. Three-dimensional conductive heat transfer topology optimisation in a cubic domain for the volume-to-surface problem. *International Journal of Heat and Mass Transfer*, 67:214–224, 2013.

[49] Suna Yan, Fengwen Wang, and Ole Sigmund. On the non-optimality of tree structures for heat conduction. *International Journal of Heat and Mass Transfer*, 122:660–680, 2018.

[50] Shuhao Wu, Yongcun Zhang, and Shutian Liu. Topology optimization for minimizing the maximum temperature of transient heat conduction structure. *Structural and Multidisciplinary Optimization*, 60(1):69–82, 2019.

[51] Lei Tang, Tong Gao, Longlong Song, Liang Meng, Chengqi Zhang, and Weihong Zhang. Topology optimization of nonlinear heat conduction problems involving large temperature gradient. *Computer Methods in Applied Mechanics and Engineering*, 357:112600, 2019.

[52] Gil Ho Yoon, Ercan Mehmet Dede, Tsuyoshi Nomura, and Paul Schmalenberg. Topology optimization of time-transient heat conduction for thermo-optic silicon modulators. *International Journal of Heat and Mass Transfer*, 157:119862, 2020.

[53] Qing Li, Grant P Steven, Yi Min Xie, and Osvaldo M Querin. Evolutionary topology optimization for temperature reduction of heat conducting fields. *International Journal of Heat and Mass Transfer*, 47(23):5071–5083, 2004.

[54] Tong Gao, Weihong Zhang, Jihong Zhu, Yingjie Xu, and David H Bassir. Topology optimization of heat conduction problem involving design-dependent heat load effect. *Finite Elements in Analysis and Design*, 44(14):805–813, 2008.

[55] Truong Nguyen, Hiroshi Isakari, Toru Takahashi, Masato Yoshino, and Toshiro Matsumoto. Level-set based topology optimization for heat conduction problem using lattice Boltzmann method. *Transactions of JASCOME*, 20:53–64, 2020.

[56] Richard H Pletcher, John C Tannehill, and Dale Anderson. *Computational fluid mechanics and heat transfer*. CRC press, 2012.

[57] R Byron Bird. We stewart, and en lightfoot. *Transport phenomena*, 11:5, 1960.

[58] Benny Lautrup. *Physics of continuous matter: exotic and everyday phenomena in the macroscopic world*. CRC press, 2011.

[59] M Necati Özışık. *Boundary value problems of heat conduction*. courier Corporation, 1989.

[60] Gilberto M Kremer. *An introduction to the Boltzmann equation and transport processes in gases*. Springer Science & Business Media, 2010.

[61] T. Inamuro, M. Yoshino, and F. Ogino. Accuracy of the lattice Boltzmann method for small knudsen number with finite reynolds number. *Physics of Fluids*, 9.

[62] Takaji Inamuro, Masato Yoshino, Hiroshi Inoue, Riki Mizuno, and Fumimaru Ogino. A lattice Boltzmann method for a binary miscible fluid mixture and its application to a heat-transfer problem. *Journal of Computational Physics*, 179(1):201–215, 2002.

[63] Y Sone. Asymptotic theory of a steady flow of a rarefied gas past bodies for small knudsen numbers. In *Advances in Kinetic Theory and Continuum Mechanics*, pages 19–31. Springer, 1991.

[64] Qisu Zou and Xiaoyi He. On pressure and velocity boundary conditions for the lattice Boltzmann BGK model. *Physics of fluids*, 9(6):1591–1598, 1997.

[65] M Alaoui and A Santos. Poiseuille flow driven by an external force. *Physics of Fluids A: Fluid Dynamics*, 4(6):1273–1282, 1992.

[66] M Yoshino and T Inamuro. Lattice Boltzmann simulations for flow and heat/mass transfer problems in a three-dimensional porous structure. *International Journal for Numerical Methods in Fluids*, 43(2):183–198, 2003.

[67] Frédéric Hecht. New development in freefem++. *Journal of numerical mathematics*, 20(3-4):251–266, 2012.

[68] Takayuki Yamada, Kazuhiro Izui, Shinji Nishiwaki, and Akihiro Takezawa. A topology optimization method based on the level set method incorporating a fictitious interface energy. *Computer Methods in Applied Mechanics and Engineering*, 199(45-48):2876–2891, 2010.

[69] F Van Keulen, RT Haftka, and NH Kim. Review of options for structural design sensitivity analysis. part 1: Linear systems. *Computer methods in applied mechanics and engineering*, 194(30-33):3213–3243, 2005.

[70] Grégoire Allaire. A review of adjoint methods for sensitivity analysis, uncertainty quantification and optimization in numerical codes. 2015.

[71] Hong-Kai Zhao, Tony Chan, Barry Merriman, and Stanley Osher. A variational level set approach to multiphase motion. *Journal of computational physics*, 127(1):179–195, 1996.

[72] Grégoire Allaire, François Jouve, and Anca-Maria Toader. A level-set method for shape optimization. *Comptes Rendus Mathematique*, 334(12):1125–1130, 2002.

[73] Samuel Amstutz and Heiko Andrä. A new algorithm for topology optimization using a level-set method. *Journal of computational physics*, 216(2):573–588, 2006.

[74] Vivien J Challis and James K Guest. Level set topology optimization of fluids in Stokes flow. *International journal for numerical methods in engineering*, 79(10):1284–1308, 2009.

[75] Zheng-Dong Ma, Noboru Kikuchi, and Hsien-Chie Cheng. Topological design for vibrating structures. *Computer methods in applied mechanics and engineering*, 121(1-4):259–280, 1995.

[76] Shinji Nishiwaki, Mary I Frecker, Seungjae Min, and Noboru Kikuchi. Topology optimization of compliant mechanisms using the homogenization method. *International journal for numerical methods in engineering*, 42(3):535–559, 1998.

[77] Grégoire Allaire, François Jouve, and Anca-Maria Toader. Structural optimization using sensitivity analysis and a level-set method. *Journal of computational physics*, 194(1):363–393, 2004.

[78] Martin P Bendsøe. Optimal shape design as a material distribution problem. *Structural optimization*, 1(4):193–202, 1989.

[79] Jaroslav Haslinger and Raino AE Mäkinen. *Introduction to shape optimization: theory, approximation, and computation*. SIAM, 2003.

[80] Yunliang Ding. Shape optimization of structures: a literature survey. *Computers & Structures*, 24(6):985–1004, 1986.

[81] Bijan Mohammadi and Olivier Pironneau. Shape optimization in fluid mechanics. *Annu. Rev. Fluid Mech.*, 36:255–279, 2004.

[82] Nikolas Provatas and Ken Elder. *Phase-field methods in materials science and engineering*. John Wiley & Sons, 2011.

[83] Gunduz Caginalp and Paul Fife. Phase-field methods for interfacial boundaries. *Physical Review B*, 33(11):7792, 1986.

[84] George J Fix. Phase field methods for free boundary problems. 1982.

[85] Shiguang Deng and Krishnan Suresh. Topology optimization under thermo-elastic buckling. *Structural and Multidisciplinary Optimization*, 55(5):1759–1772, 2017.

[86] GIN Rozvany. Aims, scope, methods, history and unified terminology of computer-aided topology optimization in structural mechanics. *Structural and Multidisciplinary optimization*, 21(2):90–108, 2001.

[87] Thomas Buhl, Claus BW Pedersen, and Ole Sigmund. Stiffness design of geometrically nonlinear structures using topology optimization. *Structural and Multidisciplinary Optimization*, 19(2):93–104, 2000.

[88] EA Kontoleontos, EM Papoutsis-Kiachagias, AS Zymaris, DI Papadimitriou, and KC Giannakoglou. Adjoint-based constrained topology optimization for viscous flows, including heat transfer. *Engineering Optimization*, 45(8):941–961, 2013.

[89] Ole Sigmund and MP Bondsgc. Topology optimization. *State-of-the-Art and Future Perspectives, Copenhagen: Technical University of Denmark (DTU)*, 2003.

[90] Michael B Giles and Niles A Pierce. An introduction to the adjoint approach to design. *Flow, turbulence and combustion*, 65(3-4):393–415, 2000.

[91] George Corliss, Christele Faure, Andreas Griewank, Laurent Hascoet, and Uwe Naumann. *Automatic differentiation of algorithms: from simulation to optimization*. Springer Science & Business Media, 2013.

[92] Vadim Komkov, Kyung K Choi, and Edward J Haug. *Design sensitivity analysis of structural systems*, volume 177. Academic press, 1986.

[93] Lisa G Stanley and Dawn L Stewart. *Design sensitivity analysis: computational issues of sensitivity equation methods*. SIAM, 2002.

[94] Kyung K Choi and Jose LT Santos. Design sensitivity analysis of non-linear structural systems part i: Theory. *International Journal for Numerical Methods in Engineering*, 24(11):2039–2055, 1987.

[95] Antonio A Novotny, Raúl A Feijóo, Edgardo Taroco, and Claudio Padra. Topological sensitivity analysis. *Computer methods in applied mechanics and engineering*, 192(7-8):803–829, 2003.

[96] H. Isakari, K. Kuriyama, H. Harada, T. Yamada, T. Takahashi, and T. Matsumoto. A topology optimization for three-dimensional acoustics with the level set method and the fast multiple boundary element method. *Mechanical Engineering Journal*, 1(4):CM0039, 2014.

[97] AA Novotny, RA Feijóo, C Padra, and E Taroco. Topological derivative for linear elastic plate bending problems. *Control and Cybernetics*, 34:339–361, 2005.

[98] Cong Chen, Kentaro Yaji, Takayuki Yamada, Kazuhiro Izui, and Shinji Nishiwaki. Local-in-time adjoint-based topology optimization of unsteady fluid flows using the lattice Boltzmann method. *Mechanical Engineering Journal*, 4(3):17–00120, 2017.

[99] Sebastian Nørgaard, Ole Sigmund, and Boyan Lazarov. Topology optimization of unsteady flow problems using the lattice Boltzmann method. *Journal of Computational Physics*, 307:291–307, 2016.

[100] Ronald M Errico. What is an adjoint model? *Bulletin of the American Meteorological Society*, 78(11):2577–2592, 1997.

[101] M Inokuti, H Sekine, and T Mura. General use of the lagrange multiplier in nonlinear mathematical physics. *Variational method in the mechanics of solids*, 33(5):156–162, 1978.

[102] Kazufumi Ito and Karl Kunisch. *Lagrange multiplier approach to variational problems and applications*. SIAM, 2008.

[103] Andrew Kirk, Sebastian Kreissl, Georg Pingen, and Kurt Maute. Lattice Boltzmann topology optimization for transient flow. In *MAESC 2011 Conference May*, volume 3, 2011.

[104] Ch H Kruger and WG Vincenti. Introduction to physical gas dynamics. *John Wlley & Sons*, 1965.

[105] Geoff Gordon and Ryan Tibshirani. Karush-kuhn-tucker conditions. *Optimization*, 10(725/36):725, 2012.

[106] Kentaro Yaji, Takayuki Yamada, Masato Yoshino, Toshiro Matsumoto, Kazuhiro Izui, and Shinji Nishiwaki. Topology optimization using the lattice Boltzmann method incorporating level set boundary expressions. *Journal of Computational Physics*, 274:158–181, 2014.

[107] Lev Davidovich Landau and Evgenii Mikhailovich Lifshits. *Fluid mechanics, by LD Landau and EM Lifshitz*, volume 11. Pergamon Press Oxford, UK, 1959.

[108] Carsten Othmer. A continuous adjoint formulation for the computation of topological and surface sensitivities of ducted flows. *International journal for numerical methods in fluids*, 58(8):861–877, 2008.

[109] Geng Liu, Martin Geier, Zhenyu Liu, Manfred Krafczyk, and Tao Chen. Discrete adjoint sensitivity analysis for fluid flow topology optimization based on the gen-

eralized lattice Boltzmann method. *Computers & Mathematics with Applications*, 68(10):1374–1392, 2014.

[110] Mathias J Krause, Gudrun ThäTer, and Vincent Heuveline. Adjoint-based fluid flow control and optimisation with lattice Boltzmann methods. *Computers & Mathematics with Applications*, 65(6):945–960, 2013.

[111] Cheng Chang, Chih-Hao Liu, and Chao-An Lin. Boundary conditions for lattice Boltzmann simulations with complex geometry flows. *Computers & Mathematics with Applications*, 58(5):940–949, 2009.

[112] Cyrus K Aidun and Jonathan R Clausen. Lattice-Boltzmann method for complex flows. *Annual review of fluid mechanics*, 42:439–472, 2010.

[113] Xuewen Yin and Junfeng Zhang. An improved bounce-back scheme for complex boundary conditions in lattice Boltzmann method. *Journal of Computational Physics*, 231(11):4295–4303, 2012.

[114] Kazem Hejranfar and Eslam Ezzatneshan. A high-order compact finite-difference lattice Boltzmann method for simulation of steady and unsteady incompressible flows. *International Journal for Numerical Methods in Fluids*, 75(10):713–746, 2014.

[115] PC Philippi, DN Siebert, LA Hegele Jr, and KK Mattila. High-order lattice-Boltzmann. *Journal of the Brazilian Society of Mechanical Sciences and Engineering*, 38(5):1401–1419, 2016.

[116] Alexander Düster, Leszek Demkowicz, and Ernst Rank. High-order finite elements applied to the discrete Boltzmann equation. *International journal for numerical methods in engineering*, 67(8):1094–1121, 2006.

[117] Kazem Hejranfar and Eslam Ezzatneshan. Implementation of a high-order compact finite-difference lattice Boltzmann method in generalized curvilinear coordinates. *Journal of Computational Physics*, 267:28–49, 2014.

Appendix

A. The explicit expressions of G_1, G_2, G_3, G_4, I, B_{w}, B_{in}, and B_{out}

The expression of the perturbed quantities of G_1, G_2, G_3, G_4, I, B_{w}, B_{in}, and B_{out} used in the Eq. (5.43) of Chapter 5 are respectively given as follows:

$$\begin{aligned} G_1[f+\varepsilon\eta] &= \int_I\int_D\int_{\mathbb{R}^2} g\frac{(f+\varepsilon\eta)}{\partial t}\ d\boldsymbol{c}dDdt \\ &= \int_I\int_D\int_{\mathbb{R}^2} g\frac{\partial f}{\partial t}\ d\boldsymbol{c}dDdt + \varepsilon\int_I\int_D\int_{\mathbb{R}^2} g\frac{\partial \eta}{\partial t}\ d\boldsymbol{c}dDdt \\ &= \int_I\int_D\int_{\mathbb{R}^2} g\frac{\partial f}{\partial t}\ d\boldsymbol{c}dDdt + \varepsilon\int_I\int_D\int_{\mathbb{R}^2} \left(\frac{\partial(g\eta)}{\partial t} - \frac{\partial g}{\partial t}\eta\right)\ d\boldsymbol{c}dDdt. \end{aligned} \tag{A1}$$

$$\begin{aligned} G_2[f+\varepsilon\eta] &= \int_I\int_D\int_{\mathbb{R}^2} g\boldsymbol{c}\cdot\nabla(f+\varepsilon\eta)\ d\boldsymbol{c}dDdt \\ &= \int_I\int_D\int_{\mathbb{R}^2} g\boldsymbol{c}\cdot\nabla f\ d\boldsymbol{c}dDdt + \varepsilon\int_I\int_D\int_{\mathbb{R}^2} g\boldsymbol{c}\cdot\nabla\eta\ d\boldsymbol{c}dDdt \\ &= \int_I\int_D\int_{\mathbb{R}^2} g\boldsymbol{c}\cdot\nabla f\ d\boldsymbol{c}dDdt + \varepsilon\int_I\int_D\int_{\mathbb{R}^2} \{\boldsymbol{c}\cdot\nabla(g\eta) - (\boldsymbol{c}\cdot\nabla g)\eta\}\ d\boldsymbol{c}dDdt \\ &= \int_I\int_D\int_{\mathbb{R}^2} g\boldsymbol{c}\cdot\nabla f\ d\boldsymbol{c}d\Omega dt + \varepsilon\int_I\int_\Gamma\int_{\mathbb{R}^2} g\eta\boldsymbol{c}\cdot\boldsymbol{n}\ d\boldsymbol{c}d\Gamma dt \\ &\quad - \varepsilon\int_I\int_D\int_{\mathbb{R}^2} (\boldsymbol{c}\cdot\nabla g)\eta\ d\boldsymbol{c}d\Omega dt. \end{aligned} \tag{A2}$$

$$\begin{aligned} G_3[f+\varepsilon\eta] &= \int_I\int_D\int_{\mathbb{R}^2} \frac{g}{\tau_B}(f+\varepsilon\eta)\ d\boldsymbol{c}dDdt \\ &= \int_I\int_D\int_{\mathbb{R}^2} \frac{g}{\tau_B}f\ d\boldsymbol{c}dDdt + \varepsilon\int_I\int_D\int_{\mathbb{R}^2} \frac{g}{\tau_B}\eta\ d\boldsymbol{c}dDdt. \end{aligned} \tag{A3}$$

$$
\begin{aligned}
G_4[f+\varepsilon\eta] &= -\int_I\int_D\int_{\mathbb{R}^2} \frac{g}{\tau_B}\hat{f}^{\mathrm{eq}}\left\{\rho[f+\varepsilon\eta], \boldsymbol{u}\left(\rho[f+\varepsilon\eta], \boldsymbol{v}[f+\varepsilon\eta]\right)\right\}\ d\boldsymbol{c}dDdt \\
&= -\int_I\int_D\int_{\mathbb{R}^2} \frac{g}{\tau_B}\hat{f}^{\mathrm{eq}}\left\{\rho[f], \boldsymbol{u}\left(\rho[f], \boldsymbol{v}[f]\right)\right\}\ d\boldsymbol{c}dDdt \\
&\quad - \varepsilon\int_I\int_D\int_{\mathbb{R}^2} \frac{g}{\tau_B}\left\{\frac{\partial \hat{f}^{\mathrm{eq}}}{\partial\rho}\rho[\eta] + \frac{\partial \hat{f}^{\mathrm{eq}}}{\partial\boldsymbol{u}}\cdot\left(\frac{\partial\boldsymbol{u}}{\partial\rho}\rho[\eta] + \frac{\partial\boldsymbol{u}}{\partial\boldsymbol{v}}\boldsymbol{v}[\eta]\right)\right\}\ d\boldsymbol{c}dDdt \\
&= -\int_I\int_D\int_{\mathbb{R}^2} \frac{g}{\tau_B}\hat{f}^{\mathrm{eq}}\left\{\rho[f], \boldsymbol{u}\left(\rho[f], \boldsymbol{v}[f]\right)\right\}\ d\boldsymbol{c}dDdt \\
&\quad - \varepsilon\int_I\int_D\int_{\mathbb{R}^2} \frac{g}{\tau_B\rho[f]}\left\{\frac{\partial \hat{f}^{\mathrm{eq}}}{\partial\rho}\rho[f] + \frac{\partial \hat{f}^{\mathrm{eq}}}{\partial\boldsymbol{u}}\cdot\left(\hat{\boldsymbol{c}} - \boldsymbol{u}[f]\right)\right\}\rho[\eta]\ d\boldsymbol{c}dDdt \\
&= -\int_I\int_D\int_{\mathbb{R}^2} \frac{g}{\tau_B}\hat{f}^{\mathrm{eq}}\left\{\rho[f], \boldsymbol{u}\left(\rho[f], \boldsymbol{v}[f]\right)\right\}\ d\boldsymbol{c}dDdt \\
&\quad - \varepsilon\int_I\int_D\int_{\mathbb{R}^2}\int_{\mathbb{R}^2} \frac{g}{\tau_B\rho[f]}\left\{\hat{f}^{\mathrm{eq}} + \frac{\hat{f}^{\mathrm{eq}}}{RT}\chi_\phi\left(\boldsymbol{c} - \chi_\phi\boldsymbol{u}\right)\cdot\left(\hat{\boldsymbol{c}} - \boldsymbol{u}\right)\right\}\eta\ d\hat{\boldsymbol{c}}d\boldsymbol{c}dDdt \\
&= -\int_I\int_D\int_{\mathbb{R}^2} \frac{g}{\tau_B}\hat{f}^{\mathrm{eq}}\left\{\rho[f], \boldsymbol{u}\left(\rho[f], \boldsymbol{v}[f]\right)\right\}\ d\boldsymbol{c}dDdt \\
&\quad - \varepsilon\int_I\int_D\int_{\mathbb{R}^2}\int_{\mathbb{R}^2} \frac{g}{\tau_B}\frac{\hat{f}^{\mathrm{eq}}}{\rho RT}\left\{RT + \chi_\phi\left(\boldsymbol{c} - \chi_\phi\boldsymbol{u}\right)\cdot\left(\hat{\boldsymbol{c}} - \boldsymbol{u}\right)\right\}\eta\ d\hat{\boldsymbol{c}}d\boldsymbol{c}dDdt \\
&= -\int_I\int_D\int_{\mathbb{R}^2} \frac{g}{\tau_B}\hat{f}^{\mathrm{eq}}\left\{\rho[f], \boldsymbol{u}\left(\rho[f], \boldsymbol{v}[f]\right)\right\}\ d\boldsymbol{c}dDdt \\
&\quad - \varepsilon\int_I\int_D\int_{\mathbb{R}^2}\int_{\mathbb{R}^2} \frac{g}{\tau_B}\frac{\hat{f}^{\mathrm{eq}}}{\rho RT}\left\{RT + \chi_\phi\left(\boldsymbol{c} - \chi_\phi\boldsymbol{u}\right)\cdot\left(\hat{\boldsymbol{c}} - \boldsymbol{u}\right)\right\}\eta\ d\hat{\boldsymbol{c}}d\boldsymbol{c}dDdt \\
&= -\int_I\int_D\int_{\mathbb{R}^2} \frac{g}{\tau_B}\hat{f}^{\mathrm{eq}}\left\{\rho[f], \boldsymbol{u}\left(\rho[f], \boldsymbol{v}[f]\right)\right\}\ d\boldsymbol{c}dDdt \\
&\quad - \varepsilon\int_I\int_D\int_{\mathbb{R}^2} \frac{\hat{g}^{\mathrm{eq}}}{\tau_B}\eta\ d\boldsymbol{c}dDdt.
\end{aligned}
\tag{A4}
$$

$$
\begin{aligned}
I[f+\varepsilon\eta] &= \int_D\int_{\mathbb{R}^2} g(f+\varepsilon\eta - f_0)\ d\boldsymbol{c}dD \\
&= \int_D\int_{\mathbb{R}^2} g(f - f_0)\ d\boldsymbol{c}dD + \varepsilon\int_D\int_{\mathbb{R}^2} g\eta\ d\boldsymbol{c}dD.
\end{aligned}
\tag{A5}
$$

$$
\begin{aligned}
B_{\mathrm{w}}[f+\varepsilon\eta] &= \int_I\int_{\Gamma_{\mathrm{w}}}\int_{\mathbb{R}^2} g\left\{f(\boldsymbol{c}) + \varepsilon\eta(\boldsymbol{c}) - f(-\boldsymbol{c}) - \varepsilon\eta(-\boldsymbol{c})\right\}\ d\boldsymbol{c}d\Gamma dt \\
&= \int_I\int_{\Gamma_{\mathrm{w}}}\int_{\mathbb{R}^2} g\left\{f(\boldsymbol{c}) - f(-\boldsymbol{c})\right\}\ d\boldsymbol{c}d\Gamma dt \\
&\quad + \varepsilon\int_I\int_{\Gamma_{\mathrm{w}}}\int_{\mathbb{R}^2} g\left\{\eta(\boldsymbol{c}) - \eta(-\boldsymbol{c})\right\}\ d\boldsymbol{c}d\Gamma dt.
\end{aligned}
\tag{A6}
$$

Here,

$$
\begin{aligned}
&\int_I \int_{\Gamma_\mathrm{w}} \int_{\mathbb{R}^2} \{g\boldsymbol{c}\cdot\boldsymbol{n} + g\eta(\boldsymbol{c}) - g\eta(-\boldsymbol{c})\}\ d\boldsymbol{c}d\Gamma dt \\
=\ &\int_I \int_{\Gamma_\mathrm{w}} \int_{\mathbb{R}^2} \{g\boldsymbol{c}\cdot\boldsymbol{n}\}\ d\boldsymbol{c}d\Gamma dt \\
=\ &\int_I \int_{\Gamma_\mathrm{w}} \int_{\boldsymbol{c}_+} g(\boldsymbol{c})\boldsymbol{c}\cdot\boldsymbol{n}\eta(\boldsymbol{c})\ d\boldsymbol{c} + \int_{\boldsymbol{c}_-} g(\boldsymbol{c})\boldsymbol{c}\cdot\boldsymbol{n}\eta(\boldsymbol{c})\ d\boldsymbol{c}d\Gamma dt \\
=\ &\int_I \int_{\Gamma_\mathrm{w}} \int_{\boldsymbol{c}_+} g(\boldsymbol{c})\boldsymbol{c}\cdot\boldsymbol{n}\eta(\boldsymbol{c})\ d\boldsymbol{c} + \int_{\boldsymbol{c}_+} g(-\boldsymbol{c})(-\boldsymbol{c}\cdot\boldsymbol{n})\eta(-\boldsymbol{c})\ d\boldsymbol{c}d\Gamma dt \\
=\ &\int_I \int_{\Gamma_\mathrm{w}} \int_{\boldsymbol{c}_+} \boldsymbol{c}\cdot\boldsymbol{n}\,\{g(\boldsymbol{c})\eta(\boldsymbol{c}) - g(-\boldsymbol{c})\eta(-\boldsymbol{c})\}\ d\boldsymbol{c}d\Gamma dt \\
=\ &\int_I \int_{\Gamma_\mathrm{w}} \int_{\boldsymbol{c}_+} \{g(\boldsymbol{c}) - g(-\boldsymbol{c})\}\,\boldsymbol{c}\cdot\boldsymbol{n}\eta(\boldsymbol{c})\ d\boldsymbol{c}d\Gamma dt.
\end{aligned}
\tag{A7}
$$

$$
\begin{aligned}
B_\mathrm{in}[f+\varepsilon\eta] &= \int_I \int_{\Gamma_\mathrm{in}} \int_{\mathbb{R}^2} g\left\{f + \varepsilon\eta - \hat{f}^\mathrm{eq}(\rho[f+\varepsilon\eta], \bar{\boldsymbol{u}})\right\}\ d\boldsymbol{c}d\Gamma dt \\
&= \int_I \int_{\Gamma_\mathrm{in}} \int_{\mathbb{R}^2} g\left\{f + \varepsilon\eta - \hat{f}^\mathrm{eq}(\rho[f], \bar{\boldsymbol{u}}) - \varepsilon\frac{\partial \hat{f}^\mathrm{eq}}{\partial\rho}\rho[\eta]\right\}\ d\boldsymbol{c}d\Gamma dt \\
&= \int_I \int_{\Gamma_\mathrm{in}} \int_{\mathbb{R}^2} g\left\{f - \hat{f}^\mathrm{eq}(\rho[f], \bar{\boldsymbol{u}})\right\}\ d\boldsymbol{c}d\Gamma dt \\
&\quad + \varepsilon\int_I \int_{\Gamma_\mathrm{in}} \int_{\mathbb{R}^2} g\eta\ d\boldsymbol{c}d\Gamma dt - \varepsilon\int_I \int_{\Gamma_\mathrm{in}} \int_{\mathbb{R}^2} \int_{\mathbb{R}^2} \frac{g\hat{f}^\mathrm{eq}}{\rho}\eta\ d\hat{\boldsymbol{c}}d\boldsymbol{c}d\Gamma dt \\
&= \int_I \int_{\Gamma_\mathrm{in}} \int_{\mathbb{R}^2} g\left\{f - \hat{f}^\mathrm{eq}(\rho[f], \bar{\boldsymbol{u}})\right\}\ d\boldsymbol{c}d\Gamma dt \\
&\quad + \varepsilon\int_I \int_{\Gamma_\mathrm{in}} \int_{\mathbb{R}^2} g\eta\ d\boldsymbol{c}d\Gamma dt - \varepsilon\int_I \int_{\Gamma_\mathrm{in}} \int_{\mathbb{R}^2} \hat{g}^\mathrm{eq}_\mathrm{in}\eta\ d\boldsymbol{c}d\Gamma dt.
\end{aligned}
\tag{A8}
$$

$$
\begin{aligned}
B_\mathrm{out}[f+\varepsilon\eta] &= \int_I \int_{\Gamma_\mathrm{out}} \int_{\mathbb{R}^2} g\left\{f + \varepsilon\eta - \hat{f}^\mathrm{eq}(\bar{\rho}, \boldsymbol{u}[f+\varepsilon\eta])\right\}\ d\boldsymbol{c}d\Gamma dt \\
&= \int_I \int_{\Gamma_\mathrm{out}} \int_{\mathbb{R}^2} g\left\{f + \varepsilon\eta - \hat{f}^\mathrm{eq}(\bar{\rho}, \boldsymbol{u}[f]) - \varepsilon\frac{\partial \hat{f}^\mathrm{eq}}{\partial\boldsymbol{u}}\cdot\left(\frac{\partial\boldsymbol{u}}{\partial\rho}\rho[\eta] + \frac{\partial\boldsymbol{u}}{\partial\boldsymbol{v}}\boldsymbol{v}[\eta]\right)\right\}\ d\boldsymbol{c}d\Gamma dt \\
&= \int_I \int_{\Gamma_\mathrm{out}} \int_{\mathbb{R}^2} g\left\{f - \hat{f}^\mathrm{eq}(\bar{\rho}, \boldsymbol{u}[f])\right\}\ d\boldsymbol{c}d\Gamma dt \\
&\quad + \varepsilon\int_I \int_{\Gamma_\mathrm{out}} \int_{\mathbb{R}^2} g\eta(\hat{\boldsymbol{c}})\ d\boldsymbol{c}d\Gamma dt \\
&\quad - \varepsilon\int_I \int_{\Gamma_\mathrm{out}} \int_{\mathbb{R}^2} \int_{\mathbb{R}^2} \frac{g\hat{f}^\mathrm{eq}}{\rho RT}\chi_\phi\left(\boldsymbol{c} - \chi_\phi\boldsymbol{u}\right)\cdot(\hat{\boldsymbol{c}} - \boldsymbol{u})\,\eta\ d\hat{\boldsymbol{c}}d\boldsymbol{c}d\Gamma dt \\
&= \int_I \int_{\Gamma_\mathrm{out}} \int_{\mathbb{R}^2} g\left\{f - \hat{f}^\mathrm{eq}(\bar{\rho}, \boldsymbol{u}[f])\right\}\ d\boldsymbol{c}d\Gamma dt \\
&\quad + \varepsilon\int_I \int_{\Gamma_\mathrm{out}} \int_{\mathbb{R}^2} g\eta(\hat{\boldsymbol{c}})\ d\boldsymbol{c}d\Gamma dt - \varepsilon\int_I \int_{\Gamma_\mathrm{out}} \int_{\mathbb{R}^2} \hat{g}^\mathrm{eq}_\mathrm{out}\eta\ d\boldsymbol{c}d\Gamma dt.
\end{aligned}
\tag{A9}
$$

B. The expressions of velocity differential equations

Let us assume the velocity $\boldsymbol{u} = (u_x, u_y)$ in Cartesian coordinates and the coordinates of a chosen lattice point reads $\boldsymbol{u} = (x_i, y_i)$. The following Taylor expansions are used to approximate the velocity gradient items with respect to x and y directions in Cartesian coordinates. They are shown as follows:

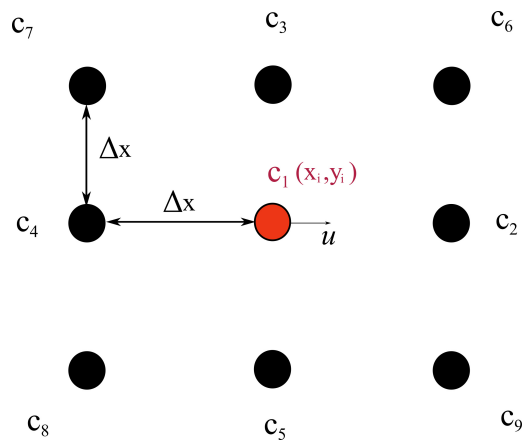

Figure B.1: The lattice point pattern 1.

1. For fluid nodes surrounding a chosen lattice point

$$u_x(x_2) = u_x(x_i + \Delta x, y_i) = u_x(x_i, y_i) + \Delta x \frac{\partial u_x}{\partial x} + \frac{(\Delta x)^2}{2!}\frac{\partial^2 u_x}{\partial x^2} + O[\Delta x]^3,$$

$$u_x(x_3) = u_x(x_i, y_i + \Delta x) = u_x(x_i, y_i) + \Delta x \frac{\partial u_x}{\partial y} + \frac{(\Delta x)^2}{2!}\frac{\partial^2 u_x}{\partial y^2} + O[\Delta x]^3,$$

...

$$u_x(x_6) = u_x(x_i + \Delta x, y_i + \Delta x) = u_x(x_i, y_i)$$
$$+ \Delta x \left(\frac{\partial u_x}{\partial x} + \frac{\partial u_x}{\partial y}\right) + \frac{(\Delta x)^2}{2!}\left(\frac{\partial^2 u_x}{\partial x^2} + \frac{\partial^2 u_x}{\partial x \partial y} + \frac{\partial^2 u_x}{\partial y^2}\right) + O[\Delta x]^3,$$

$$u_x(x_7) = u_x(x_i - \Delta x, y_i + \Delta x) = u_x(x_i, y_i)$$
$$+ \Delta x \left(\frac{\partial u_x}{\partial x} - \frac{\partial u_x}{\partial y}\right) + \frac{(\Delta x)^2}{2!}\left(\frac{\partial^2 u_x}{\partial x^2} - \frac{\partial^2 u_x}{\partial x \partial y} + \frac{\partial^2 u_x}{\partial y^2}\right) + O[\Delta x]^3,$$

...

Thus,

$$\frac{\partial u_x}{\partial x} = \frac{1}{6\Delta x}\left[u_x(x_2) - u_x(x_4) + u_x(x_6) - u_x(x_7) - u_x(x_8) + u_x(x_9)\right], \tag{B1}$$

$$\frac{\partial u_x}{\partial y} = \frac{1}{6\Delta x}\left[u_x(x_3) - u_x(x_5) + u_x(x_6) + u_x(x_7) - u_x(x_8) - u_x(x_9)\right]. \tag{B2}$$

Similarly,

$$\frac{\partial u_y}{\partial x} = \frac{1}{6\Delta x}\left[u_y(x_2) - u_y(x_4) + u_y(x_6) - u_y(x_7) - u_y(x_8) + u_y(x_9)\right], \tag{B3}$$

$$\frac{\partial u_y}{\partial y} = \frac{1}{6\Delta x}\left[u_y(x_3) - u_y(x_5) + u_y(x_6) + u_y(x_7) - u_y(x_8) - u_y(x_9)\right]. \tag{B4}$$

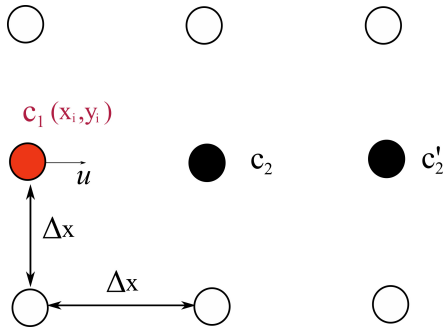

Figure B.2: The lattice point pattern 2.

2. For fluid nodes are placed on the right side of the left-end lattice points

$$u_x(x_1) = u_x(x_i, y_i),$$

$$u_x(x_2) = u_x(x_i, y_i) + \Delta x\frac{\partial u_x}{\partial x} + \frac{(\Delta x)^2}{2!}\frac{\partial^2 u_x}{\partial x^2} + O[\Delta x]^3,$$

$$u_x(x_2^{'}) = u_x(x_i, y_i) + 2\Delta x\frac{\partial u_x}{\partial x} + 2(\Delta x)^2\frac{\partial^2 u_x}{\partial x^2} + O[\Delta x]^3.$$

Thus,

$$\frac{\partial u_x}{\partial x} = \frac{1}{2\Delta x}\left[-3u_x(x_1) + 4u_x(x_2) - u_x(x_2^{'})\right], \tag{B5}$$

$$\frac{\partial u_x}{\partial y} = \frac{1}{2\Delta x}\left[-3u_x(x_1) + 4u_x(x_3) - u_x(x_3^{'})\right]. \tag{B6}$$

Similarly,

$$\frac{\partial u_y}{\partial x} = \frac{1}{2\Delta x}\left[-3u_y(x_1) + 4u_y(x_2) - u_y(x_2^{'})\right], \tag{B7}$$

$$\frac{\partial u_y}{\partial y} = \frac{1}{2\Delta x}\left[-3u_y(x_1) + 4u_y(x_3) - u_y(x_3^{'})\right]. \tag{B8}$$

3. For fluid nodes are placed on the right side of the right-end lattice points

$$u_x(x_1) = u_x(x_i, y_i),$$

$$u_x(x_4) = u_x(x_i, y_i) - \Delta x\frac{\partial u_x}{\partial x} + \frac{(\Delta x)^2}{2!}\frac{\partial^2 u_x}{\partial x^2} + O[\Delta x]^3,$$

$$u_x(x_4^{'}) = u_x(x_i, y_i) - 2\Delta x\frac{\partial u_x}{\partial x} + 2(\Delta x)^2\frac{\partial^2 u_x}{\partial x^2} + O[\Delta x]^3.$$

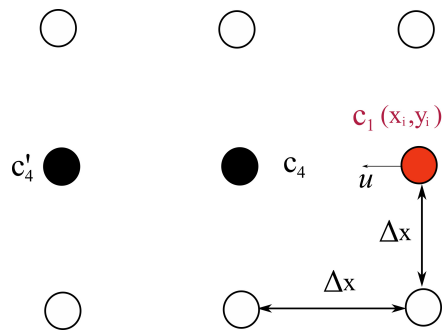

Figure B.3: The lattice point pattern 3.

Thus,

$$\frac{\partial u_x}{\partial x} = -\frac{1}{2\Delta x}\left[-3u_x(x_1) + 4u_x(x_4) - u_x(x_4^{'})\right], \tag{B9}$$

$$\frac{\partial u_x}{\partial y} = -\frac{1}{2\Delta x}\left[-3u_x(x_1) + 4u_x(x_5) - u_x(x_5^{'})\right]. \tag{B10}$$

Similarly,

$$\frac{\partial u_y}{\partial x} = -\frac{1}{2\Delta x}\left[-3u_y(x_1) + 4u_y(x_4) - u_y(x_4^{'})\right], \tag{B11}$$

$$\frac{\partial u_y}{\partial y} = -\frac{1}{2\Delta x}\left[-3u_y(x_1) + 4u_y(x_5) - u_y(x_5^{'})\right]. \tag{B12}$$

List of Publications

The publications associated with this thesis are given as follows:

[P1]: Nguyen T., Isakari H., Takahashi T., Yaji K., Yoshino M., and Matsumoto T. Level-set based topology optimization of transient flow using lattice Boltzmann method considering an oscillating flow condition. *Computers & Mathematics with Applications*, Vol. 80, Issue 1, pp. 82-108, 2020.

[P2]: Nguyen T., Isakari H., Takahashi T., Yoshino M., and Matsumoto T. Level-set based topology optimization for heat conduction problem using lattice Boltzmann method. *Transactions of JASCOME*, Vol. 20, pp. 53-64, 2020.